University of Alberta

Charged Entities Interacting with Electronically Responsive Structures with Implications for the Modeling of Interactions between Carbon Nanotubes and DNA

by

Oxana Malysheva

A thesis submitted to the Faculty of Graduate Studies and Research
in partial fulfillment of the requirements for the degree of

Doctor of Philosophy

Department of Mechanical Engineering

Fall 2011
Edmonton, Alberta

To My Family, You are everything to me.

Abstract

Understanding interactions between charged entities with electronically responsive structures embedded in an electrolytic environment is important because of the diverse range of practical applications. This study was motivated by the technique where single stranded DNA was used to separate carbon nanotubes (CNTs) with different electronic properties (metallic or semiconducting).

The objective of this study was to create theoretical models which improve the understanding of the DNA-assisted separation technique for CNTs. In the course of this study four models with different levels of complexity at the continuum level were developed, with the electrostatic interaction being the main focus. In each of these models, with certain simplifications on geometry the boundary value problems for the electric potential were formulated using equations of electrostatics and in particular the Debye-Hückel theory for electrolyte. Using mathematical techniques, semi-analytical solutions for the electric potential were obtained and its implication for the DNA-CNT interaction and the property of the DNA-CNT hybrid were discussed. It was found that the electric potential due to a metallic CNT-DNA hybrid is weaker than that for a semiconducting CNT-DNA. In addition to that based on the proposed models, it was observed that the obtained results are applicable to a larger class of problems involving charged entities interacting with responsive structures. For example, it was studied how the phenomenon of counterion condensation on a polyelectrolyte (PE) is affected by the presence of a responsive cylinder. It was shown that counterions gradually release from the surface of the PE as it approaches a metallic cylinder, whereas more counterions are condensed on the PE as it approaches a dielectric cylinder where the dielectric constant of that cylinder ia smaller than that of the electrolyte solution.

Results from this dissertation clearly demonstrate that in order to model the interaction between a charged entity and an electronically responsive structure, it is crucial to account for the response of the structure. Therefore, the models developed here have implications for modeling interactions between other charged entities near responsive structures. For example, cells adhering to an implant's surface and biosensors detecting a specific DNA sequence.

Contents

List of Figures

Acknowledgements

From the bottom of my heart I would like to thank my great supervisors: Dr. Peter Schiavone and Dr. Tian Tang. Without them, this dissertation would not be possible for many reasons. It was my pleasure to know Dr. Schiavone for one and a half years before I joined the University of Alberta (in September 2007). It was a long journey for me before I was admitted to the University of Alberta. Dr. Schiavone was waiting for me and let me believe that the day would come and the TOEFL test would be behind me. Without his patience and encouragement, I would never have found enough strength to learn the language and write the TOEFL exams. From that moment, Dr. Schiavone became a great mentor in my life. My outstanding second supervisor is Dr. Tian Tang, she is a superb example of a successful professor in the beginning of her career. I am very thankful that Dr. Tang has provided me with interesting topics for my research and for the interesting discussions about my research topic. Throughout my studies, both my supervisors, Drs. Tang and Schiavone, were providing me with useful advice and shared their scientific knowledge. Without them, I would not be, where I am today.

Also, I would like to thank my group members and colleagues. In particular, Chun Il Kim and Laleh Golshahi for being my friends and being with me the whole time I have been at the University of Alberta; Chongbo Sun for making the illustrations seen in my introduction (Figures 1–4); Tamran Lengyel for proofreading my introduction and providing me with valuable feedback; Morteza Chehel Amirani for our enjoyable discussions of our research. It is my pleasure to know all of them. Moreover, I found two very good friends, Elizaveta Luybimova and Olga Luybimova, at the university of Alberta. Both of them have influenced my life and made it fuller and happier.

I would also like to thank for financial support my supervisors, the Department of Mechanical Engineering, and FGSR for the Queen Elizabeth Scholarship. In addition to this I would like to thank all the professors with whom I had the opportunity to work with while doing my TA. In particularly, Dr. Schiavone, Dr. Ru and Dr. Lange.

And last but not least, I would like to thank to my parents and my husband (as well as the rest of my family) for providing me with love and support. It means a lot to me.

List of Abbreviations

Symbol	Description
CNT	Carbon Nanotube
DNA	Deoxyribonucleic Acid
swCNT	single-walled Carbon Nanotube
mwCNT	multi-walled Carbon Nanotube
ssDNA	single-stranded DNA
dsDNA	double-stranded DNA
PE	Polyelectrolyte
IEC	Ion Exchange Chromatography
Poly(T)	ssDNA consisting of repeating Thymine bases
Poly(GT)	ssDNA consisting of alternation Thymine and Guanine bases
vdW	Van der Waals
MD	Molecular Dynamics
EDL	Electric Double Layer
PB	Poisson-Boltzmann
DH	Debye-Hückel
CC	Counterion Condensation
DFT	Density Functional Theory
MM	Molecular Mechanics
AFM	Atomic Force Microscopy
CHARMM	Chemistry at HARvard Molecular Mechanics
DLVO	Derjaguin-Landau-Verwey-Overbeek
GE	Governing Equation
BC	Boundary Condition
BVP	Boundary Value Problem
LJ	Lennard-Jones Potential
DOS	Density of States
1D	One Dimensional
TB	Tight Binding
HiPco	High Pressure Carbon Monoxide

List of Symbols

Here, dimensional parameters that appear in the analysis are listed. Whenever bar is added to a parameter, it represents the dimensionless value associated with that parameter, unless otherwise specified. The specific normalization is also defined in each chapter.

Chapter 1: List of Symbols

Symbol	Description
$1/k$	Debye Length
c	Salt Concentration of Electrolyte Solution
ϕ	Electric Potential
q	Unsigned Charge of Electron
k_B	Boltzmann Constant
T	Temperature
ξ	Dimensionless Charge Density
θ	Amount of Condensed Counterions per unit Charge
b	Average Spacing along Contour of Charged Molecule
l_B	Bjerrum Length
ξ_{crit}	Threshold Value for Dimensionless Surface Charge Density
z	Unsigned Valence of Counterions
σ_{crit}	Critical Surface Charge Density
σ	Surface Charge Density before Counterion Condensation

Chapter 2: List of Symbols

Symbol	Description
$\mathbf{D}$	Electric Displacement
ρ	Total Electric Charge Density
$\mathbf{E}$	Electric Field
ε_0	Permittivity of Free Space

Continued on Next Page...

Chapter2: List of Symbols (Continued)

Symbol	Description
ϕ	Electric Potential
ρ^f	Free-Charge Density
ρ^p	Polarization Charge Density
$\mathbf{P}$	Polarization Field
χ	electric susceptibility
ε_1	Dielectric Constant of Medium
ϵ	Permittivity of Medium
k_B	Boltzmann Constant
T	Temperature
μ	Chemical Potential
q	Unsigned Charge of Electron
z_k	Valence of the k^{th} type of Ions
n_k	Number Densities of k^{th} type of Ion in Solution
n_k^0	Bulk Number Densities of k^{th} type of Ion
N	Number of Ionic Species
N_D	Number Density of Ionized Donors
N_A	Number Density of Ionized Acceptors
n	Number Density of Electrons
p	Number Density of Holes
E_F	Fermi Level of Electrons
n_i	Intrinsic Carrier Density
E_V	Top of Valence Band
E_C	Bottom of Conduction Band
N_C	Effective Density of States in Conduction Band
N_V	Effective Density of State in Valence Band
$1/k_2$	Debye Length in Semiconductor
ρ	Charge density
σ	Surface Charge Density

Chapter 3: List of Symbols

Symbol	Description
ϕ	Electric Potential
q	Unsigned Charge of Electron
z_i	Valence of the i^{th} Species of Ions
n_i^0	Bulk Number Density of the i^{th} Species of Ions
ε_0	Permittivity of Free Space
ε_1	Dielectric Constant of Electrolyte Solution

Continued on Next Page...

Chapter 3: List of Symbols (Continued)

Symbol	Description
k_B	Boltzmann Constant
T	Temperature
$1/k$	Debye Length
l_b	Bjerrum Length
σ	Uniform Charge Density on Substrate
n	Integer Describing Total Charge of Particle
Q	Charge of Particle ($Q = nq$)
$1/k_1$	Debye Length of Electrolyte Solution
$1/k_2$	Debye Length of Semiconducting Substrate
ε_2	Dielectric Constant of Dielectric or Semiconducting Substrate
d	Distance between Particle with charge Q and Substrate with Surface Charge σ
(r, z)	Cylindrical Coordinates
L	Thickness of Dielectric Substrate
ϕ_σ	Electric Potential due to σ
ϕ_Q	Electric Potential due to Q
$J_0(x)$	0th order Bessel Function of the First Kind
E_F	Difference between Current Fermi Level and Intrinsic Fermi Level of Electrons
n_i	Intrinsic Carrier Density
E_g	Band Gap of Semiconductor
G_{vdw}	Van der Waals Free Energy
G_{el}	Electrostatic Free Energy due to Presence of Substrate
$\varepsilon_{2/1}$	Ratio of ε_2 to ε_1
$k_{2/1}$	Ratio of k_2 to k_1
g_{el}	Normalized value of G_{el}
g_{vdW}	Normalized value of G_{vdW}
g	Normalized Total Free Energy
u	Lennard-Jones Potential
r_o	Distance where $u = 0$
c	Depth of Lennard-Jones Potential Well
N	Number of Atoms in Particle with Charge Q
ρ_1	Atom Number Density in Substrate

Chapter 4: List of Symbols

Symbol	Description
ξ	Dimensionless Polymer Charge Density

Continued on Next Page...

Chapter 4: List of Symbols (Continued)

Symbol	Description
ξ_{crit}	Critical Value of ξ
$1/k$	Debye Length
σ_{crit}	Critical Value of Surface Charge Density
r_0	Radius of Electronically Responsive Cylinder
a	Radius of Thin Cylinder representing Polyelectrolyte
d	Distance between Centers of Polyelectrolyte (PE) and Responsive Cylinder
ε_1	Dielectric Constant of Electrolyte Solution
ε_2	Dielectric Constant of Dielectric Cylinder
(r, ψ)	Polar Coordinates with Origin in Center of Responsive Cylinder
(r', ψ')	Polar Coordinates with Origin in Center of PE
θ	Number of Condensed Counterions
σ	Surface Charge Density on PE
q	Elementary Charge
$\phi_{in(l)}^{met}$	Electric Potential Inside of Metallic Cylinder
$\phi_{in(l)}^{diel}$	Electric Potential Inside of Dielectric Cylinder
ϕ_{out}^{met}	Electric Potential in Electrolyte solution due to PE-metallic Cylinder System
ϕ_{out}^{diel}	Electric Potential in Electrolyte solution due to PE-dielectric Cylinder System
$\phi_{in(s)}^{met}$	Electric Potential in PE due to PE-metallic Cylinder System
$\phi_{in(s)}^{diel}$	Electric Potential in PE due to PE-dielectric Cylinder System
ε_0	Permittivity of Vacuum
$K_n(x)$	the n^{th} order Modified Bessel Function of the Second Kind (n is integer)
l_B	Bjerrum Length
k_B	Boltzmann Constant
T	Temperature
b	Length of Cylinder per unit Surface Charge
θ	Number of Counterions per unit Charge on PE
z	Unsigned Valence of Counterions
γ	Activity Coefficient for Bulk Solution
ν	Number of Counterions in Chemical Formula of Salt
c	Bulk Salt Concentration
Q	Internal Partition Function of Condensed Layer
g_{el}	Normalized Electrostatic Free Energy per unit Length of PE
g_{en}	Normalized Entropic Energy per unit Length
g	Normalized Total Free Energy per unit Length of PE
e	Base of Natural Logarithm
N_A	Avogadros Number

Continued on Next Page...

Chapter 4: List of Symbols (Continued)

Symbol	Description
ν_i	Number of the i^{th} type of Ion in Chemical Formula of Salt
η_1	Percentage Error for Electric Potential
η_2	Percentage Error for Electric Displacement

Chapter 5: List of Symbols

Symbol	Description
r_0	Radius of Electronically Responsive Cylinder
a	Radius of PE
d	Distance between Centers of PE and Responsive Cylinder
d_1	Distance between Center of Responsive Cylinder and Charged Wall
d_2	Distance between Charged Wall from Center of PE
σ_{PE}	Uniform Charge Density on PE
σ_s	Uniform Charge Density on Wall
$1/k$	Debye Length
l_B	Bjerrum Length
ε_1	Dielectric Constant of Electrolyte Solution
ε_2	Dielectric Constant of Dielectric Cylinder
(r, ψ)	Polar Coordinates with Origin in Center of Responsive Cylinder
(x, y)	Cartesian Coordinates with Origin in Center of Responsive Cylinder
(r', ψ')	Polar Coordinates with Origin in Center of PE
ϕ_0^{met}	Electric Potential in Electrolyte Solution due to PE-metallic Cylinder Complex
ϕ_1^{met}	Electric Potential in Responsive Cylinder due to PE-metallic Cylinder Complex
ϕ_2^{met}	Electric Potential in PE due to due to PE-metallic Cylinder Complex
ϕ_0^{diel}	Electric Potential in Electrolyte Solution due to PE-dielectric Cylinder Complex
ϕ_1^{diel}	Electric Potential in Responsive Cylinder due to PE-dielectric Cylinder Complex
ϕ_2^{diel}	Electric Potential in PE due to due to PE-dielectric Cylinder Complex
c	Salt Concentration of Electrolyte Solution
ϕ_c	Electric Potential inside of Metallic Cylinder
ε_0	Permittivity of Vacuum
$\mathbf{F}$	Force on Charged Wall due to PE-cylinder Complex
$\mathbf{E}$	Electric Field in Electrolyte Solution
F_x^{met}	Binding Force per unit Length in Horizontal Direction due to PE-metallic Cylinder Complex

Continued on Next Page...

Chapter 5: List of Symbols (Continued)

Symbol	Description
F_x^{diel}	Binding Force per unit Length in Horizontal Direction due to PE-dielectric Cylinder Complex
l_B	Bjerrum Length
k_B	Boltzmann Constant
T	Temperature
$K_n(x)$	the n^{th} order Modified Bessel Functions of the Second Kind (n is integer)
ε_{21}	Ratio of ε_2 to ε_1
θ	Amount of Counterion Condensation

Chapter 6: List of Symbols

Symbol	Description
r_{CNT}	Radius of Cylindrical Surface representing Carbon Nanotube (CNT)
r_{DNA}	Radius of Cylindrical Surface representing DNA molecule
σ_{DNA}	Surface Charge Density on Cylindrical Surface Representing DNA
σ_{CNT}	Charge Induced on CNT Surface
$1/k$	Debye Length
ε_0	Dielectric Constant of Electrolyte Solution
ε_1	Dielectric Constant between Surfaces representing DNA and CNT
r	Polar Radius
ϕ_0^m	Electric Potential in Electrolyte Solution due to Metallic CNT-DNA Hybrid
ϕ_1^m	Electric Potential between surfaces representing DNA and CNT due to Metallic CNT-DNA Hybrid
ϕ_2^m	Electric Potential inside of CNT due to Metallic CNT-DNA Hybrid
ϕ_0^s	Electric Potential in Electrolyte Solution due to Semiconducting CNT-DNA Hybrid
ϕ_1^s	Electric Potential between surfaces representing DNA and CNT due to Semiconducting CNT-DNA Hybrid
ϕ_2^s	Electric Potential inside of CNT due to Semiconducting CNT-DNA Hybrid
$epsilon$	Permittivity of Free Space
E	Energy
$V_{pp\pi}$	Nearest-neighbor Interaction
a	Lattice Constant of Graphene Sheet
a_{C-C}	Distance between Carbon Atoms
$\nu(E)$	Universal DOS per Carbon Atom

Continued on Next Page...

Chapter 6: List of Symbols (Continued)

Symbol	Description
(n_1, n_2)	Pair of Integer Indices Defining CNTs Chirality
$\delta\rho$	Amount of Induced Charge per Carbon Atom
E_F	Fermi level
$F(E)$	Fermi distribution function
e	Unsigned Charge of Electron
ϕ_{CNT}	Electric Potential on CNT
k_B	Boltzmann Constant
T	Temperature
z	Valence of Cation in Electrolyte Solution
l_B	Bjerrum Length
$I_0(x)$	the 0th order Modified Bessel Functions of the First Kind
$K_0(x)$	the 0th order Modified Bessel Functions of the Second Kind
θ	Wrapping Angle of DNA around CNT
c	Salt Concentration of Electrolyte Solution

Appendix A: List of Symbols

Symbol	Description
a_{C-C}	Distance between two Carbon Atoms
a	Lattice Constant of Graphene Sheet
$\vec{a}_1, \vec{a}_2$	Unit Vectors of Hexagonal Lattice in Real Space
$\vec{b}_1, \vec{b}_2$	Unit Vectors from Reciprocal Hexagonal Lattice
$\vec{k}$	Wave Vector
E	energy
H	Hamiltonian matrix
S	Overlap Matrix
Φ_j	Bloch Function for Orbitals
$\vec{R}$	Lattice Vector
r_{CNT}	Radius of Carbon Nanotube
$V_{pp\pi}$	Nearest-neighbor Interaction
$\rho(E)$	Density of States per Carbon Atom
(n_1, n_2)	Pair of Integer Indices Defining CNTs Chirality

Preface

The seven chapters in this dissertation represent the author's work on the interaction of charged entities with electronically responsive structures, and its implication for the modeling of interactions between carbon nanotubes and DNA. This thesis follows the mixed format as described by Faculty of Graduate Studies and Research (FGSR) of the University of Alberta. Chapter 1 is an introduction to the whole thesis, and it shows how other chapters are related. In Chapter 2 the description of the fundamentals of electrostatics are provided. Chapters 3, 4, 5, and 6 were originally written as separate papers. Therefore, the same symbol in one of these chapters may have a different physical meaning from that of the same symbol in a different chapter. The definition of each symbol is consistent within each chapter. Chapter 7 summarizes the results of the whole thesis. Finally, each chapter has its own bibliography. Therefore, the reference numbers in a specific chapter only correspond to the list at the end of that chapter.

Chapter 1
Introduction

The motivation for this thesis arose from a remarkable phenomenon which is concerned with the separation of "bundles"of carbon nanotubes (CNTs) into individual tubes. This separation is essential if the CNTs are to be used in practical applications. The aforementioned phenomenon (of separation) involves the interaction of singles strands of Deoxyribonucleic acid (DNA) with the CNTs bundles. The fascination of the author comes from the fact that two seemingly unrelated yet well-recognized structures could combine together to produce such a remarkable result of the separation of bundled CNTs. The initial idea behind this thesis was to try and understand this mechanism of interaction between DNA and CNT bundles using some form of mathematical model. As all good modelers know, the latter involves a delicate balancing act between trying to separate the most significant aspects of the mechanism without producing an intractable model of the process. We quickly identified that the initial steps in model development were part of the more general subject matter dealing with charged entities interacting with electronically responsive structures, which is where the majority of this thesis is concentrated.

1.1 Carbon nanomaterials

Since the discovery of carbon nanomaterials in the mid 1980s, their use has been increasing. The reason for this is that they became widely accepted because of promising potential applications in different areas [1–3]. For example, biomedical, electronic, environmental and energy industries. In the last two decades the discovery of different carbon nanomaterials (fullerene) was reported [4, 5], such as buckminsterfullerene C_{60}, carbon nanotubes (CNT), and graphene.

Figure 1.1(a) depicts fullerene, discovered in 1985, which can be imagined as a hollow carbon sphere. Figure 1.1(b) depicts a carbon nanotube, discovered in

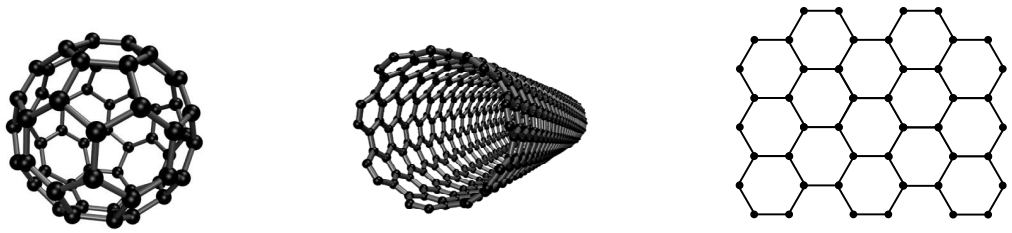

(a) (b) (c)

Figure 1.1: a) Buckminsterfullerene/buckyball, b) carbon nanotube; and c) piece of the graphene sheet. In this figure, the black circles represent carbon atoms, and the lines connecting carbon atoms are covalent bonds.

1991, which resembles a hollow carbon cylinder. Figure 1.1(c) depicts graphene, discovered in 2004, which is a sheet of graphite of one atom thick. Graphene can be imagined as atomic-scale "chicken wire", made of carbon atoms and covalent bonds (special chemical bonds) between them. To appreciate the dimensions of these structures note that the atom is incredibly small: it is only one tenth of a nanometer (1 Å = angstrom is equal to 0.1 nm).

The most interesting structures arising from carbon nanomaterials are carbon nanotubes (CNTs) due to their unique electronic, mechanical, and thermal properties [5]. CNTs were discovered by Iijima in 1991 [4, 5] and for the last twenty years, an extensive amount of studies have been performed to utilize their unique properties in electronic [6, 7], biomedical [8–10], and many others applications [11–13]. CNTs can have two different forms: single-walled CNTs (swCNTs) depicted in Figure 1.2(a) and multi-walled CNTs (mwCNTs) depicted in Figure 1.2(b). A single-walled CNT can be visualized as a seamless cylinder wrapped from a graphene sheet and, depending on the direction of wrapping of the graphene sheet in the tube, CNTs can possess different electronic properties (metallic or semiconducting). Multi-walled CNTs on the other hand can be visualized as several tubes with different radii placed one inside the other.

The diameter of the experimentally observed single-walled CNTs ranges from 0.7 nm to 2 nm, and the average length is on the order of microns [5], although CNTs of the order of centimeters in length are produced. CNTs are incredibly

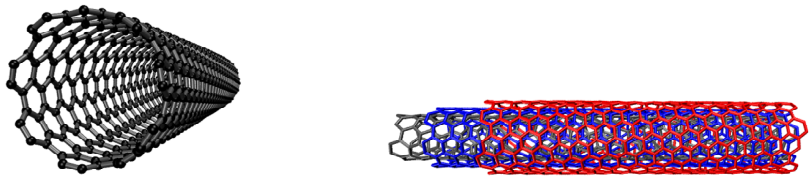

(a) (b)

Figure 1.2: a) A single-walled carbon nanotube; b) multi-walled carbon nanotube.

light and strong. The stiffness of the material is measured in terms of Young's modulus. Different theoretical methods and experimental measurements predict different values for the Young's modulus for single-walled CNTs, starting from around 1 TPa (1TPa $= 10^3$ GPa $= 10^9$ Pa) to near 5 TPa [12, 14, 15]. This means that CNTs are between five to twenty five times stiffer than similar structures made from stainless steel.

1.2 Separating carbon nanotubes via the mechanism of DNA interactions

CNTs can be manufactured using different techniques: carbon-arc discharge, laser ablation, or chemical vapor deposition [4, 5]. The outcome of the manufacturing process is bundled CNTs, with metallic and semiconducting tubes present within the bundle. To be able to use them in practical applications, the CNTs have to be dispersed into individual tubes and then separated according to their electronic properties. This is not trivial, because there is a strong adhesion between CNTs and the hydrophobicity of CNTs makes it difficult to disperse them in aqueous solutions. However, this is a necessary step because, as mentioned above, practical applications require dispersed CNTs with certain electronic properties. Different techniques for dispersion and separation of CNTs are available to utilize electronic properties of the CNTs.

One of the successful and remarkable techniques to disperse and separate CNTs in an aqueous solution is to use single-stranded DNA (ssDNA) molecules as depicted in Figure 1.3. DNA molecules are polyelectrolytes (PEs) [16]. PEs are poly-

mers bearing repeating ionizable groups [17]. These groups are able to dissociate in an aqueous solution, making DNA molecules charged. When DNA molecules are immersed in an aqueous solution, their electric neutrality is lost. In an aqueous solution, DNA molecules become negatively charged because one proton dissociates from each phosphate group [18]. The separation between two neighboring phosphorous atoms on DNA backbone is 7 Å.

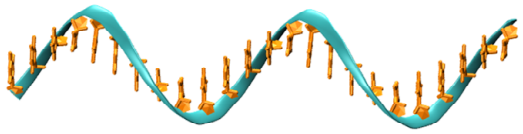

Figure 1.3: Representation of a single-stranded DNA molecule (ssDNA). It consists of backbone and bases (Adenine, Guanine, Cytosine, Thymine). The blue ribbon represents the backbone, which consists of alternating phosphate groups and sugar. The bases are shown in orange.

In 2003 a group of scientists (Zheng *et al.*) successfully applied the ssDNA-assisted CNT dispersion technique to disperse CNTs in aqueous solution and to separate them according to their electronic properties by the ion exchange chromatography (IEC) method [19]. Even though single-stranded DNAs are not the only polymers that are able to disperse CNTs, they are the most efficient at doing so [19]. In the process of dispersion, bundled CNTs are sonicated with ssDNA molecules in an aqueous solution with low salt concentration (0.1 M = moles/litre for table salt - sodium chloride NaCl). An aqueous solution with a small amount of salt forms an electrolyte solution, which is a medium with ions capable of conducting electricity. As a result of sonication, negatively charged ssDNA-CNT hybrids are formed (See Figure 1.4). Molecular modeling suggests that ssDNA molecules wrap around CNTs in a helical fashion [19]. The phosphate groups on the ssDNA-CNT hybrid are negatively charged. Due to the difference in the electronic properties of metallic and semiconducting CNTs, it is speculated that the surface charge distribution would be modified differently [19]. This allows the separation of CNTs into several fractions by IEC, particularly anion exchange chromatography. In the IEC method an electrolyte solution with dispersed negatively charged ssDNA-CNT

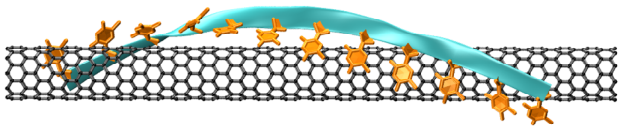

Figure 1.4: Helical wrapping of ssDNA molecule around CNT, so called CNT-DNA hybrid.

hybrids is passed through the column packed with the anion exchange resins. The resin surface gets positively charged upon being introduced in the electrolyte solution so that the negatively charged phosphate groups of DNA bind to it. At this stage, the separation of the ssDNA-CNT hybrids according to the electronic properties of the CNT's core could be done by passing the solution with the increased salt concentration through the column. As the salt concentration in the solution increases (from 0.1 M to 0.8 M), the salt ions are able to exchange with the ssDNA-hybrids. Experiments show that the metallic CNTs elute from the column earlier than the semiconducting ones. Zheng *et al.* speculated that this would happen due to their reduced surface charge [19].

Following the experiments, Zheng *et al.* conducted molecular statics (MS) calculations of a Poly(T) with semiconducting (10, 0) CNT in vacuum [19]. Poly(T) is a ssDNA consisting of repeating thymine (T) bases only. By minimizing the energy of Poly(T) and CNT, favorable configurations of the Poly(T) and CNT are determined. In the preferred range of the torsion angles of ssDNA molecule, there are many favorable configurations. Helical wrapping is one of the favorable configurations, and it is supported by images from atomic force microscopy (AFM) of CNT-DNA hybrids based on Poly(GT) [20]. Further, Zheng *et al.* found that wrapping of CNTs by ssDNA molecules is sequence-dependent [20]. It was identified that the best separation of CNTs according to their electronic properties and diameters was obtained by using Poly(GT), i.e. ssDNA molecules consisting of alternating guanine (G) and thymine (T) bases. Later on, Tu *et al.* [21] refined the experiments, and identified the specific DNA sequences which are able to separate CNTs with specific chiralities. The efficiency of the dispersion and separation depends on the DNA sequence, salt concentration and the type of salt [19, 20].

Although experiments show promising results, it is necessary to understand the interactions in the hybrid to be able to obtain full control of this method. However, due to the size of the hybrid, it is impossible to measure the total interactions between the DNA and CNT experimentally. CNT-DNA hybrids are very complex, and include many interactions: van der Waals adhesion of the DNA bases to the surface of the CNT, elasticity of DNA and deformation of the CNT, electrostatic interaction between DNA charges and the metallic/semiconducting CNT, hydrophobic interactions between DNA bases and the CNT.

Using scaling analyses, Manohar et al. [22] determined that in a dilute electrolyte solution the most important interactions for the formation of CNT-DNA hybrids are:

- the electrostatic interaction between DNA charges (charged phosphate groups) and the metallic/semiconducting CNT;
- the van der Waals adhesion of the DNA bases to CNT.

Electrostatic interaction is one of the long-ranged interactions which occurs between the charges. For a system consisting of a CNT-DNA hybrid embedded in an electrolyte solution the electrostatic interaction has several components. The first component is the interaction of DNA charges with metallic/semiconducting CNT. The second component is the interaction of ions in the electrolyte solution with a CNT-DNA hybrid. At the nano scale, the interactions which are negligible in the macroscopic world become important [23]. One of these interactions is van der Waals forces (vdW). All atoms have a nucleus and electrons, and the former consists of protons and neutrons. Even though the whole atom is neutral, the location of electrons and protons do not coincide in the atom. This gives rise to the temporary dipole. Interaction between any two dipoles of different particles is the origin of the vdW forces. Compared with covalent interactions, van der Waals forces are long-range and can be effective from larger distances (greater than 10 nm) down to interatomic spacings (about 0.2 nm). Depending on the separation distance, vdW forces may be repulsive or attractive, and play a significant role at short distances. Essentially vdW interaction is electric in nature.

The main focus throughout this thesis, therefore, is given to the electrostatic interaction between CNT and DNA in the hybrid. It is proposed that the electric field induced by DNA charges will be affected differently by the metallic or semiconducting CNTs, and it will explain the difference observed in the IEC experiments.

1.2.1 Charged entities interacting with electronically responsive structures: phenomena driven by electrostatic interactions

By studying the interaction between charged DNA molecules and CNTs, it became clear that the CNT-DNA hybrid is a subset of a larger set of problems: that are described by the interaction of charged entities with electronically responsive structures. This broad topic has significance in other areas such as 1) in medicine, cells adhere to the implants with various electronic properties [24]; 2) in bio-medicine modeling, DNA based biosensors are used to detect the desired types of DNA [25, 26].

In this thesis, the focus will remain on the CNTs, so that in this context, the CNT is the electronically responsive structure, and the DNA molecule is the charged entity. To summarize, in this work the interaction of the charged entities with electronically responsive structures is examined with the CNT-DNA hybrid being the motivating factor.

For charged entities interacting with electronically responsive structures embedded in an aqueous solution, there are several important phenomena partially driven by the electrostatic interaction. These include the electric double layer near the surface of the charged entity (DNA molecule) and the phenomenon of counterion condensation on the charged entity embedded in the electrolyte solution.

Electrolyte solution

An electrolyte environment can be described as a liquid substance containing ions (atoms or molecules with a net positive or negative electric charge). By means of these ions, the electrolyte solution conducts electricity. One of the simplest examples of an electrolyte solution is water with table salt (sodium chloride $NaCl$). In

water, the salt breaks down into sodium ions (Na^+) and chloride ions (Cl^-). In the human body, to maintain a healthy lifestyle, the electrolyte balance of calcium, potassium and sodium must be preserved, because the body uses ions to conduct electric impulses between tissues of the body [27].

In mathematical modeling, approaches at different levels of complexity can be used to represent an electrolyte solution: the explicit [28] and the implicit [29–31] approaches. Both approaches can be used in molecular dynamics (MD) simulations, depending on the systems under consideration and available computational resources. In the first approach, each molecule in the electrolyte solution is modeled explicitly. In the latter approach, the electrolyte solution is modeled implicitly. In continuum modeling, the implicit approach is often used. For example, in a primitive model of an electrolyte solution [32] at the continuum level the ions are represented by hard spheres with the charge of the ion located at the center of the sphere. The solvent is represented by a continuum medium with a certain dielectric permittivity; ions and solvent have the same dielectric permittivity. Usually, the size of the ions is neglected, and ions are considered as point charges. The dielectric permittivity or dielectric constant measures the ability of a material to be polarized by an external field; it is a factor by which the external electric field is reduced when penetrating the material. In this approach, the fundamentals of classical electrostatics are combined with statistical mechanics and used to study the interaction between the charged objects in an electrolyte solution. The implicit approach is less computationally demanding compared to the explicit approach. At a continuum level, it allows one (in some situations) to obtain a closed-form analytical or semi-analytical solution, which can be tested quicker at the real time scale.

Electric double layer

When an object, such as a solid particle, is embedded in an aqueous solution then the surface of this object may become charged. This happens due to dissociation or ionization of the surface groups from the surface of the particle to the aqueous solution or binding ions from a solution to a previously uncharged surface. Depending on the sign of the ions ($^+$ or $^-$) leaving the surface or binding to it, the surface

of the particle gets positively or negatively charged. However, the overall system (including the particle and aqueous solution) is neutral. Overall electroneutrality is achieved by the presence of counterions. Counterions are ions with a charge that is opposite to the charge on the surface of the particle, whereas co-ions are ions with the same sign of the charge as that of the particle. There could be two types of counterions close to the particle: 1) ions which are bound to the surface of the particle within the so-called Stern layer (it is only one atom thick); and 2) diffuse layer of counterions participating in thermal motion. This structure, consisting of the charge on the surface of the particle, bounded counterions, and diffused ions, is called an electrical double layer (EDL) [23, 30]. EDL is depicted on Figure 1.5. After the diffuse layer, bulk solution begins. It refers to the part of the solution, where ions of the solution are influenced only by other ions of the solution, and not by any other interfaces. To measure the thickness of EDL at the nanometer scale, the Debye length, $1/k$, is used. The Debye length is used to measure how rapidly the electric potential (caused by the charge on the surface of the particle) falls off from its value at the surface. For example, at one Debye length away from the surface, electric potential falls off to about one-third of its value at the surface. At several Debye lengths away from the surface of the particle, the electric field is effectively screened by the build-up of a diffuse layer of counterions. Also, the Debye length is related to the salt concentration c of the electrolyte solution, as $1/k \sim 1/\sqrt{c}$. A more dilute solution corresponds to a larger Debye length compared to a solution with an increased salt concentration. The Debye length of 1 nm corresponds to an electrolyte solution with a roughly physiological condition [33]. The Debye length from 10 to 100 nm corresponds to the dilute electrolyte solution.

The common ways of treating the layer of diffused ions around a charged molecule is through the Poisson-Boltzmann (PB) equation (implicit approach) [23, 30]. The PB equation is a non-linear second order differential equation for the electric potential. The closed-form (analytical) solution is available only for simple geometries [30], in other cases numerical calculations are required. Another approach available for treating the layer of diffused ions is the linearized Poisson-Boltzmann equation, which is called the Debye-Hückel (DH) equation. The DH

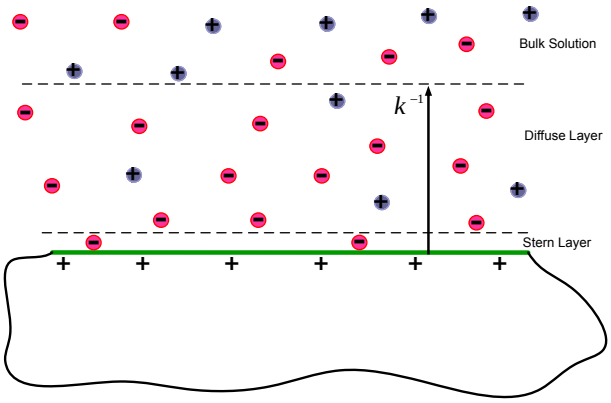

Figure 1.5: Electric double layer on the interface between solid and liquid.

equation can be solved for many geometries. It is valid under the condition that the electric potential is small, that is, $q\phi/k_BT << 1$ [30]. Here, q is the unsigned charge of an electron, ϕ is the electric potential, k_B is the Boltzmann constant, and T is the temperature. The DH equation can be used to obtain an analytical solution. However, for highly charged molecules the validity condition breaks down, and the PB equation should be used instead [30]. For highly charged molecules, G.S. Manning resolved this difficulty by proposing the theory of counterion condensation [34]. This theory allows one to apply the DH equation in the remote regions from the highly charged molecule when the original charge density of the molecule is replaced by an effectively reduced charge density.

Counterion Condensation

The phenomenon of counterion condensation (CC) occurs near a highly charged molecule, such as DNA, embedded in an electrolyte solution. This phenomenon is observed experimentally [35, 36] and also it is supported through MD simulations [37]. It is analogous to the above mentioned Stern layer [38]. The theory of counterion condensation was developed by G.S. Manning in 1969. This theory allows one to obtain an analytical expression for the amount of condensed counterions, θ, per unit charge [34, 39–42]. The condition for the existence of CC is given in terms of the dimensionless charge density ξ. A dimensionless charge density is

equal to $\xi = l_B/b$ [35], where l_B is the Bjerrum length [30], and b is the average spacing along the contour of a charged molecule. There is a threshold value for the dimensionless surface charge density $\xi_{\text{crit}} = 1/z$. When $\xi > \xi_{\text{crit}}$, then counterion condensation occurs on the surface of the charged molecule and it partially neutralizes the charge, where z is the unsigned valence of the counterions. When $\xi \leq 1/z$, then there is no counterion condensation. Also, equivalent conditions for the existence of CC are derived by Manning [41] in terms of the critical surface charge density σ_{crit} for the charged molecules of different geometries (sphere-like, cylinder-like, wall-like). In this formulation, CC occurs on the charged molecule, when $\sigma > \sigma_{crit}$, where σ is the surface charge density before CC.

According to Manning, the amount of CC can be obtained by considering the equilibrium between two contributions to the Helmholtz free energy of the charged molecule: electrostatic and entropic contributions. Hereafter it is referred to as free energy. The electrostatic contribution is the electrostatic interaction between the charged molecule and the counterions, which tends to attract the counterions from the bulk solution to the vicinity of the charged molecule. The entropic contribution is the entropic effect, which tends to keep the counterions in a more random state, namely, in the bulk. The competition between these two contributions defines the amount of CC on the charged molecule. In the theory of CC proposed by Manning, it says that if the charge on the surface of the molecule is partially reduced by CC, then the diffused ions are governed by the DH equation. The DH equation can be solved analytically with a few governing parameters.

1.2.2 Available techniques for modeling systems in electrolyte solution

To study the interactions between systems in an aqueous solution, the models of different scales have been developed, including: *ab initio* ("from the first principles") and semi-empirical calculations, molecular dynamics, coarse-grained molecular dynamics models, and continuum modeling.

The *ab initio* method uses quantum mechanical calculations to study the behavior of the desired materials at the electronic level (an atom being comprised

of electrons and nucleus). Hartree-Fock method [43], Density Functional Theory (DFT) [44] are *ab initio* methods, which are used to obtain electronic behavior of materials from the first principles using quantum mechanical calculations. *Ab initio* methods are extremely accurate. However, the main disadvantage is that these methods are computationally expensive and allow one to study only systems of a few hundreds atoms over a short time scale (1 ps, where 1 ps = 10^{-12}s).

The tight binding method [5, 45] is a semi-empirical quantum mechanics method, which is important for treating molecules such as DNA, where the full *ab initio* calculations are computationally expensive. It is based on the Hartree-Fock method, but it includes many approximations, and some parameters come from empirical data.

Molecular dynamics (MD) simulations are performed at an atomic level by solving Newton's equations of motion for each atom in the considered system until the time evolution for the desired time period is reached [28, 46]. This allows one to study the configuration and energetics of the charged molecules in solvents. In MD simulations, force fields are used to describe the potential energy of a system of atoms [28, 46]. Force fields are developed using data from the experiments and from *ab initio* methods. This implies that MD is empirical in origin. MD simulations give a unique insight into the intermolecular interactions and they can be very accurate, although computationally expensive. Comparing MD with *ab initio* methods [47], it can be seen that the former is more computationally affordable. However, the simulated time and the size of the model are still small. MD methods allow one to study systems at short time scales (on the order of a few microseconds), and the number of atoms in the system is of the order of 10^6 [47, 48].

The coarse-grained MD method improves the computational affordability by reducing the number of independently modeled atoms. Instead of explicitly modeling each atom of the system, a collection of atoms is modeled as a single coarse grained particle, and the whole system is modeled using MD simulations. This modeling greatly reduces the number of degrees of freedom compared with MD calculations and are performed for all the atoms of the system, allowing one to simulate larger systems in microsecond time scale; however, it comes with the risk of losing some

atomistic details.

At the continuum level, the solvent has been represented implicitly by an effective dielectric medium [29], and the screening effect of the ions in the solution can be characterized using the Poisson–Boltzmann (PB) or Debye-Hückel (DH) equation for the electric potential [30].

1.2.3 Literature review of past modeling works on CNT-DNA hybrids

Theoretical approaches at different levels have been developed to shed light on the interactions between CNT-DNA hybrids. Meng *et al.* [49] take a combined approach to calculate the interaction energy between a DNA base and semiconducting (10, 0) CNT. Using molecular mechanics (MM) with CHARMM force field [50], the energetically favorable configurations of the base on the CNT are found. Then to further optimize the structure *ab initio* calculations are used. Afterwards, the interaction energy is calculated for the optimized configurations. Two groups of authors [51, 52] have utilized *ab initio* calculations to study interactions of DNA base with CNTs. In [51], the authors found that five DNA/RNA bases exhibit different interaction strengths with (5, 0) CNT. In [52], the authors studied the adsorption of adenine on the surface of metallic (6,6) swCNT and thymine on the surface of semiconducting (8,0) swCNT. It should be noted that in [51, 52], the charges on the DNA backbone are not taken into consideration, and therefore, the electronic response of the CNT is not reflected. Rotkin *et al.* using tight binding calculations performed semi-empirical quantum modeling for the electronic structure of the CNT-DNA hybrid in vacuum [45]. The CNT-DNA hybrid is modeled by considering Poly(T) helically wrapped around semiconducting (7,0) CNT. The polarization component of cohesion energy of the CNT-DNA hybrid is calculated. The results confirm that the CNT-DNA hybrids are highly stable. However, all these quantum mechanics calculations lack one main feature. Their analysis was performed in the absence of an aqueous solution, which is an important factor because in the experiments dispersion and separation of CNT-DNA hybrids occur in the dilute electrolyte solution. It will be difficult to add an aqueous solution to the system, because *ab initio*

calculations can only be used for small systems.

Johnson *et al.* conducted a series of MD simulations [53] in an aqueous environment. In this work, the detailed analysis of CNT-DNA hybrid can be found. It includes possible configurations of CNT-DNA hybrids, the dynamical process of self-assembly of the hybrids and energetic properties of the hybrids. The major benefit of MD simulations is that they give valuable insights into dynamics and molecular details of the CNT-DNA hybrids. However, these simulations remain computationally expensive. They can be performed on systems with smaller dimensions with time scales between ten and several thousand nanoseconds. In addition, MD simulations rely on the molecular mechanics force field, but a reliable force field that can reflect the electronic response of the CNT is not yet available. In other words, in the above mentioned MD simulations [53], the interactions between the CNT atoms and all other atoms of the system (DNA, water and ions) is modeled mathematically using the Lennard-Jones potential [54]. CNTs with different chiralities differ only in structure, but not in their electronic properties. Zou *et al.* used coarse-grained MD modeling of DNA-CNT hybrid [55]. Modeling at the atomic scale is provided for CNT, whereas DNA bases and backbones are modeled using coarse particles. This modeling greatly reduces the number of degrees of freedom compared with MD calculations, allowing one to simulate larger systems in microsecond time scale. Zou *et al.* tested their results against the results from MD simulations, and the results were similar. At the continuum level, Lustig *et al.* proposed a simplified analytical model to the described IEC method for CNT-DNA hybrids in an electrolyte solution [56]. In their work, DNA is modeled as a helical line of discrete charges, CNT is modeled locally as a half-space (pure metallic or pure dielectric), and the electrolyte solution is modeled implicitly through the Debye-Hückel (DH) equation. Their model predicts that the metallic CNT-DNA hybrids elute from the column earlier than the semiconducting CNT-DNA hybrids. The continuum modeling is less computationally demanding compared with calculations mentioned above, because it significantly reduces the degrees of freedom of the electrolyte solution. This allows one to study larger systems than could be done using molecular simulations.

Currently, none of the methods mentioned above incorporate all the details for a CNT-DNA hybrid in an aqueous solution. For example, due to the restrictions of the existing computational resources, an aqueous environment was omitted in the works employing quantum mechanics calculations [19, 45, 49]. These calculations would be able to capture the difference in the electronic responses from different types of CNTs (metallic or semiconducting) due to DNA charges. However, because they are computationally expensive, it is impossible to implement them on systems with more than a few hundred atoms. Whereas, even though MD simulations are able to employ aqueous solutions in the desired systems and provide the full atomic picture of them, due to the nature of the force fields used in MD, it is impossible to capture the difference due to the electronic properties of CNTs. The continuum approach, on the other hand, allows one to trade the atomic details of CNT-DNA hybrids with the opportunity of incorporating electronic response due to CNT's core of a CNT-DNA hybrid in an electrolyte solution.

1.3 Overview of dissertation

This dissertation is devoted to the understanding of the electrostatic interaction between charged entities with electronically responsive substrates in an aqueous solution at a continuum level. In particular, it is devoted to the understanding of the interaction between DNA molecules (representing charged entities) and carbon nanotubes (representing electronically responsive structures). In this dissertation, it will be shown through a series of chapters, the importance of considering the electronic response of the electronically responsive substrate when the charged entity is located nearby. This understanding has significance not only for the understanding of the separation mechanism of the CNTs using DNA molecules, but also it has crucial importance in other areas as well [24–26]. From the very beginning, the main attention was given to the development of theoretical models, which would provide us with a better understanding of the interaction of CNT-DNA hybrids. To do this, fundamental studies for an initial model of the interaction between CNT and DNA are conducted at the continuum level. Compared with full atomic simu-

lations, the continuum approach allows a reduced degree of freedom of the system and closed analytical or semi-analytical solutions, which could be tested quicker at real time scales. From molecular simulations, one can make a judgment as to which interactions to consider [22], and then build a continuum model. Based on the results by Manohar *et al.* [22] and Lustig *et al.* [56], it can be seen that in a dilute electrolyte solution electrostatic interaction is most important for formation of CNT-DNA hybrids, as well as for separating CNT-DNA hybrids based on the electronic properties of the CNT. Here, it is proposed that due to the fact that CNTs have different electronic properties, the electric field induced by DNA charges will be affected differently depending on the CNTs core.

This dissertation is organized as follows, general preliminaries are presented in Chapter 2. Several models for the charged entities with electronically responsive structures (CNT-DNA hybrids) with an increasing level of complexity are considered in Chapters 3, 4, 5, and 6. The common feature for all models is the electrostatic interaction between a charged entity (a charged particle or a PE/DNA) and an electronically responsive substrate/cylinder (representing CNT) embedded in a dilute electrolyte solution.

The main body of the thesis is described as follows. The first attempt towards understanding the electrostatic interaction between the charged entity and the responsive structure is provided in Chapter 3. The main goal of this chapter is to show that there is a difference in the electronic response caused by a charged entity near an electronically responsive structure. The system, considered in Chapter 3, consists of a charged particle above the electronically responsive substrate embedded in a dilute electrolyte solution. The substrate can be metallic, dielectric or semiconducting. In a dilute electrolyte solution, our results demonstrate a distinct electronic response of the charged particle to a different substrate. Also, using the Derjaguin-Landau-Verwey-Overbeek (DLVO) theory [23], the equilibrium separation between a charged particle and a charged responsive substrate is obtained. According to the DLVO theory, the total contribution to the energy of the system consists of electrostatic and van der Waals contributions. The equilibrium separation between the particle and the substrate is determined by minimizing the sum of

Gibbs free energy consisting of electrostatics and vdW contributions. Our results demonstrate a distinct equilibrium pattern of the charged particle to a responsive substrate.

It should be mentioned that the system, considered in Chapter 3, can be viewed as the most simplified model to study the interaction of DNA molecule and CNT in the CNT-DNA hybrid. The charged particle represents the DNA charge, and the electronically responsive substrate, locally, represents CNT. In Chapter 3, it has been shown that the electrostatic interaction has crucial importance for such models. We also note that the model developed in this chapter has implications in cell adhesion, because the cells adhere to implants with diverse electronic properties [24]. In the area of cell adhesion, it is not only important to find a bio-compatible material (for example, in the field of joint replacement or in dentistry), but it is also necessary to know how well the implant integrates into the body. Cell adhesion to the implant surface is crucial to wound healing, tissue regeneration and many other applications [24, 57]. In orthopedic procedures, ceramic, metallic, or plastic implants are used [58, 59]. Whereas, in dentistry, titanium or zirconia (ceramic material) implants are preferred [60, 61].

The next attempt towards the understanding of the electrostatic interaction between a charged entity and an electronically responsive substrate is presented in Chapter 4. In this chapter, the charged entity is a polyelectrolyte (PE), and the primitive model of the PE is utilized. The PE is modeled as a uniformly charged long rigid cylinder [40, 62]. In the area of polyelectrolytes, the phenomenon of counterion condensation (CC) is important, and it is widely studied [40, 41]. In this chapter, the phenomenon of CC on the PE is studied. By utilizing Manning's theory mentioned in Section 1.2.1, it is shown how CC on the PE is affected by the presence of the electronically responsive cylinder (metallic or dielectric). It is found that the amount of CC on the PE depends on the nature of the electronically responsive cylinder. The model developed in this chapter, can be considered as a simplified model for CNT-DNA hybrid. The PE represents a DNA molecule, and the metallic/dielectric cylinder represents a CNT. It is shown that electrostatically driven phenomena depend on the electronic nature of the CNT.

In Chapter 5, a primitive model for a CNT-DNA hybrid and its application in DNA assisted separation of CNTs is described. In this chapter, we utilize the same model for a CNT-DNA hybrid that was presented in Chapter 4. By introducing a positively charged wall near a primitive model for a CNT-DNA hybrid, that is referred to as a PE-cylinder system, the binding force between the wall and the system is studied in order to understand the observations seen in DNA assisted CNT separation using IEC [19]. Our results show that the binding force due to the PE near a grounded metallic cylinder is weaker than that due to the PE near a neutral dielectric cylinder. In addition, it is shown that the charge of the metallic cylinder affects the magnitude and the direction of the binding force.

In Chapters 3, 4, and 5, CNT is modeled as an electronically responsive substrate/cylinder (simple metal, dielectric or semiconductor) and an analytical solution describing the electrostatic behavior of each system is obtained. In Chapter 6, we move one step closer towards a physically realistic model of CNT-DNA hybrid by considering the more exact response of CNT to DNA charges. To do this, quantum mechanics results for the one-dimensional universal density of states of the CNT are implemented [63]. The obtained results for the electric potential are in agreement with experimental observations [19].

Finally, a summary of the thesis along with the recommendations for future work is given in Chapter 7.

Bibliography

[1] R. Bakry, R. M. Vallant, M. Najam-ul Haq, M. Rainer, Z. Szabo, C. W. Huck, and G. K. Bonn, "Medicinal applications of fullerenes," *International journal of nanomedicine*, vol. 2, no. 4, pp. 639–649, 2007.

[2] B. Yadav and K. R., "Structure, properties and applications of fullerenes," *International Journal of Nanotechnology and Applications*, vol. 2, no. 1, pp. 15–24, 2008.

[3] F. Lange and J.-F. Nierengarten, *Fullerenes: principles and applications*. The Royal Society of Chemistry, 2007.

[4] M. Dresselhaus, G. Dresselhaus, and P. Eklund, *Science of Fullerenes and Carbon Nanotubes*. Academic Press, San Diego, 1996.

[5] R. Saito, G. Dresselhaus, and M. Dresselhaus, *Physical Properties of Carbon Nanotubes*. Imperial College Press, London, 1991.

[6] J. Guo, S. Goasguen, M. Lundstrom, and S. Datta, "Metal-insulator-semiconductor electrostatics of carbon nanotubes," *Applied physics letters*, vol. 81, no. 8, pp. 1486–1488, 2002.

[7] T. Tang and A. Jagota, "Model for Modulation of Conductance in a Carbon Nanotube Field Effect Transistor by Electrochemical Gating," *Journal of computational and theoretical nanoscience*, vol. 5, no. 10, pp. 1989–1996, 2008.

[8] Z. Guo, P. Sadler, and S. Tsang, "Immobilization and visualization of DNA and proteins on carbon nanotubes," *Advanced materials*, vol. 10, no. 9, pp. 701–703, 1998.

[9] T. Okada, T. Kaneko, R. Hatakeyama, and K. Tohji, "Electrically triggered insertion of single-stranded DNA into single-walled carbon nanotubes," *Chemical physics letters*, vol. 417, no. 4-6, pp. 288–292, 2006.

[10] H. Gao, Y. Kong, D. Cui, and C. Ozkan, "Spontaneous insertion of DNA oligonucleotides into carbon nanotubes," *Nano letters*, vol. 3, no. 4, pp. 471–473, 2003.

[11] R. Baughman, A. Zakhidov, and W. de Heer, "Carbon nanotubes - the route toward applications," *Science*, vol. 297, no. 5582, pp. 787–792, 2002.

[12] J. Salvetat, J. Bonard, N. Thomson, A. Kulik, L. Forro, W. Benoit, and L. Zuppiroli, "Mechanical properties of carbon nanotubes," *Applied physics a-materials science & processing*, vol. 69, no. 3, pp. 255–260, 1999.

[13] J. Makar and J. Beaudoin, "Carbon nanotubes and their application in the construction industry," tech. rep.

[14] Y. Huang, J. Wu, and K. C. Hwang, "Thickness of graphene and single-wall carbon nanotubes," *Physical review B*, vol. 74, no. 24, 2006.

[15] S. Sinnott and R. Andrews, "Carbon nanotubes: Synthesis, properties, and applications," *Critical reviews in solid state and materials sciences*, vol. 26, no. 3, pp. 145–249, 2001.

[16] C. Anderson and M. Record, "Polyelectrolyte theories and their applications to DNA," *Annual review of physical chemistry*, vol. 33, pp. 191–222, 1982.

[17] A. D. Jenkins, P. Kratochvil, R. F. T. Stepto, and U. Suter, "Glossary of basic terms in polymer science," *Pure & Appl. Chem*, vol. 68(12), pp. 2287–2311, 1996.

[18] R. Dias and B. Lindman, *DNA interactions with polymers and surfactants*. John Wiley, 2008.

[19] M. Zheng, A. Jagota, E. Semke, B. Diner, R. Mclean, S. Lustig, R. Richardson, and N. Tassi, "DNA-assisted dispersion and separation of carbon nanotubes," *Nature materials*, vol. 2, no. 5, pp. 338–342, 2003.

[20] M. Zheng, A. Jagota, M. Strano, A. Santos, P. Barone, S. Chou, B. Diner, M. Dresselhaus, R. McLean, G. Onoa, G. Samsonidze, E. Semke, M. Usrey, and D. Walls, "Structure-based carbon nanotube sorting by sequence-dependent DNA assembly," *Science*, vol. 302, no. 5650, pp. 1545–1548, 2003.

[21] X. Tu, S. Manohar, A. Jagota, and Z. M., "Dna sequence motifs for structure-specific recognition and separation of carbon nanotubes," *Nature*, vol. 460.

[22] S. Manohar, T. Tang, and A. Jagota, "Structure of homopolymer DNA-CNT hybrids," *Journal of physical chemistry C*, vol. 111, no. 48, pp. 17835–17845, 2007.

[23] J. Israelachvili, *Intermolecular And Surface Forces*. Academic Press, 2010.

[24] K. Anselme, "Osteoblast adhesion on biomaterials," *Biomaterials*, vol. 21, no. 7, pp. 667–681, 2000.

[25] J. Rusling, *Biomolecular films: design, function, and applications*. Surfactant science series, Marcel Dekker, 2003.

[26] Z. Tang, H. Wu, J. R. Cort, G. W. Buchko, Y. Zhang, Y. Shao, I. A. Aksay, J. Liu, and Y. Lin, "Constraint of DNA on Functionalized Graphene Improves its Biostability and Specificity," *SMALL*, vol. 6, no. 11, pp. 1205–1209, 2010.

[27] C. Passanisi, *Electrocardiography Essentials*. Delmar Publishers Inc; 1 edition, 2001.

[28] T. Schlick, *Molecular modeling and simulation: an interdisciplinary guide*. Interdisciplinary applied mathematics, Springer, 2002.

[29] C. Cramer and D. Truhlar, "Implicit solvation models: Equilibria, structure, spectra, and dynamics," *CHEMICAL REVIEWS*, vol. 99, no. 8, pp. 2161–2200, 1999.

[30] W. B. Russel, *Colloidal Dispersions*. Cambridge Univ. Press, Cambridge, UK, 1989.

[31] J. Lyklema, *Fundamentals of Interface and Colloid Science: Solid-liquid interfaces*. Fundamentals of Interface and Colloid Science, Academic Press, 1995.

[32] D. McQuarrie, *Statistical mechanics*. University Science Books, 2000.

[33] K. Kunze and R. Netz, "Salt-induced DNA-histone complexation," *Physical review letters*, vol. 85, no. 20, pp. 4389–4392, 2000.

[34] G. Manning, "Limiting laws and counterion condensation in polyelectrolyte solutions I. Colligative properties ," *Journal of Chemical Physics*, vol. 51, no. 3, pp. 924–933, 1969.

[35] G. Manning, "The critical onset of counterion condensation: A survey of its experimental and theoretical basis," *Berichte der bunsen-gesellschaft-physical chemistry chemical physics*, vol. 100, no. 6, pp. 909–922, 1996.

[36] A. Popov and D. Hoagland, "Electrophoretic evidence for a new type of counterion condensation," *Journal of polymer science part B-polymer physics*, vol. 42, no. 19, pp. 3616–3627, 2004.

[37] M. Young, B. Jayaram, and D. Beveridge, "Intrusion of counterions into the spine of hydration in the minor groove of B-DNA: Fractional occupancy of electronegative pockets," *Journal of the american chemical society*, vol. 119, no. 1, pp. 59–69, 1997.

[38] J. Lyklema, *Fundamentals of interface and colloid science*. No. v. 5 in Fundamentals of Interface and Colloid Science, Academic Press, 2005.

[39] G. Manning, "Molecular theory of polyelectrolyte solutions with applications to electrostatic properties of polynucleotides," *Quarterly reviews of biophysics*, vol. 11, no. 2, pp. 179–246, 1978.

[40] G. Manning, "Counterion condensation theory constructed from different models," *Physica A*, vol. 231, no. 1-3, pp. 236–253, 1996.

[41] G. S. Manning, "Counterion condensation on charged spheres, cylinders, and planes," *Journal of physical chemistry B*, vol. 111, no. 29, pp. 8554–8559, 2007.

[42] J. Ray and G. Manning, "An attractive force between two rodlike polyions mediated by the sharing of condensed counterions," *LANGMUIR*, vol. 10, no. 7, pp. 2450–2461, 1994.

[43] A. Szabó and N. Ostlund, *Modern quantum chemistry: introduction to advanced electronic structure theory*. Dover Publications, 1996.

[44] R. Parr and W. Yang, *Density-functional theory of atoms and molecules*. International series of monographs on chemistry, Oxford University Press, 1994.

[45] S. V. Rotkin, "Electronic Properties of Nonideal Nanotube Materials: Helical Symmetry Breaking in DNA Hybrids," in *Annual review of physical chemistry*, vol. 61 of *Annual Review of Physical Chemistry*, pp. 241–261, 2010.

[46] D. Frenkel and B. Smit, *Understanding molecular simulation: from algorithms to applications*. Computational science, Academic Press, 2002.

[47] R. Johnson, *Probing the Structure and Function of Biopolymer-Carbon Nanotube Hybrids with Molecular Dynamics*. Publicly accessible Penn Dissertations. Paper 5. http://repository.upenn.edu/edissertations/5, 2009.

[48] H. Gao and Y. Kong, "Simulation of DNA-nanotube interactions," *Annual review of materials research*, vol. 34, pp. 123–150, 2004.

[49] S. Meng, P. Maragakis, C. Papaloukas, and E. Kaxiras, "DNA nucleoside interaction and identification with carbon nanotubes," *Nano letters*, vol. 7, no. 1, pp. 45–50, 2007.

[50] B. R. Brooks, C. L. Brooks, III, A. D. Mackerell, Jr., L. Nilsson, R. J. Petrella, B. Roux, Y. Won, G. Archontis, C. Bartels, S. Boresch, A. Caflisch,

L. Caves, Q. Cui, A. R. Dinner, M. Feig, S. Fischer, J. Gao, M. Hodoscek, W. Im, K. Kuczera, T. Lazaridis, J. Ma, V. Ovchinnikov, E. Paci, R. W. Pastor, C. B. Post, J. Z. Pu, M. Schaefer, B. Tidor, R. M. Venable, H. L. Woodcock, X. Wu, W. Yang, D. M. York, and M. Karplus, "CHARMM: The Biomolecular Simulation Program," *Journal of computational chemistry*, vol. 30, no. 10, Sp. Iss. SI, pp. 1545–1614, 2009.

[51] S. Gowtham, R. H. Scheicher, R. Pandey, S. P. Karna, and R. Ahuja, "First-principles study of physisorption of nucleic acid bases on small-diameter carbon nanotubes," *Nanotechnology*, vol. 19, no. 12, 2008.

[52] Y. V. Shtogun, L. M. Woods, and G. I. Dovbeshko, "Adsorption of adenine and thymine and their radicals on single-wall carbon nanotubes," *Journal of physical chemistry C*, vol. 111, no. 49, pp. 18174–18181, 2007.

[53] R. Johnson, A. T. C. Johnson, and M. L. Klein, "Probing the structure of dna-carbon nanotube hybrids with molecular dynamics," *Nano Lett.*, vol. 8, no. 1, pp. 69–75, 2008.

[54] L. Girifalco, *Statistical mechanics of solids*. Monographs on the physics and chemistry of materials, Oxford University Press, 2000.

[55] J. Zou, W. Liang, and S. Zhang, "Coarse-grained molecular dynamics modeling of DNA-carbon nanotube complexes," *International journal for numerical methods in engineering*, vol. 83, no. 8-9, Sp. Iss. SI, pp. 968–985, 2010.

[56] S. Lustig, A. Jagota, C. Khripin, and M. Zheng, "Theory of structure-based carbon nanotube separations by ion-exchange chromatography of DNA/CNT hybrids," *Journal of physical chemistry B*, vol. 109, no. 7, pp. 2559–2566, 2005.

[57] G. Schneider, A. English, M. Abraham, R. Zaharias, C. Stanford, and J. Keller, "The effect of hydrogel charge density on cell attachment," *Biomaterials*, vol. 25, no. 15, pp. 3023–3028, 2004.

[58] F. Johnson and K. Virgo, *The bionic human: health promotion for people with implanted prosthetic devices*. Methods in molecular biology, Humana Press, 2006.

[59] C. Piconi, G. Maccauro, F. Muratori, and B. E., "Alumina and zirconia ceramics in joint replacements," *J. of Applied Biomaterials & Biomechanics*, vol. 1, no. , pp. 19–32, 2003.

[60] M. Gahlert, S. Roehling, M. Wieland, C. M. Sprecher, H. Kniha, and S. Milz, "Osseointegration of zirconia and titanium dental implants: a histological and histomorphometrical study in the maxilla of pigs," *Clinical oral implants research*, vol. 20, no. 11, pp. 1247–1253, 2009.

[61] R. Depprich, H. Zipprich, M. Ommerborn, E. Mahn, L. Lammers, J. Handschel, C. Naujoks, H.-P. Wiesmann, N. R. Kubler, and U. Meyer, "Osseointegration of zirconia implants: an SEM observation of the bone-implant interface," *Head & Face Medicine*, vol. 4-25, no. , p. 7 pages, 2008.

[62] S. Brenner and D. McQuarri, "Theory of Electrostatic interaction between paraller cylindrical polyelectrolytes," *Journal of Colloid and Interface Science*, vol. 44, no. 2, pp. 298–317, 1973.

[63] J. Mintmire and C. White, "Universal density of states for carbon nanotubes," *Physical review letters*, vol. 81, no. 12, pp. 2506–2509, 1998.

Chapter 2
Preliminaries

In this chapter the basics for electrostatics are described. The governing equations (GEs) for the electric potential in different medias are listed. As well as the boundary conditions (BCs) for the electric potential are explained.

2.1 The fundamentals

The simplified Maxwell equations for electrostatics are the following [1]

$$\nabla \cdot \mathbf{E} = \frac{\rho}{\varepsilon_0}, \tag{2.1}$$

and

$$\nabla \times \mathbf{E} = 0, \tag{2.2}$$

where ρ is the total electric charge per unit volume (charge density), and $\mathbf{E}$ is the electric field, and ε_0 is the permittivity of vacuum. Also, Eq. (2.1) can be written in terms of the dielectric displacement $\mathbf{D}$. In this case, the constitutive relation between $\mathbf{D}$ and $\mathbf{E}$ is the following

$$\mathbf{D} = \varepsilon_0 \mathbf{E}. \tag{2.3}$$

According to Eq. (2.2), the electric field is conservative, therefore there exists a scalar potential ϕ such that

$$\mathbf{E} = -\nabla \phi. \tag{2.4}$$

Therefore, from Eq. (2.1), the electric potential should satisfy the Poisson equation

$$\nabla^2 \phi = -\frac{\rho}{\varepsilon_0}. \tag{2.5}$$

If vacuum is replaced by a medium with dielectric constant ε_1, Eq. (2.1) becomes [2]

$$\nabla \cdot \mathbf{E} = \frac{\rho^f + \rho^p}{\varepsilon_0}, \tag{2.6}$$

where ρ^f is the free-charge density, and ρ^p is the polarized charged density defined as

$$\rho^p = -\nabla \cdot \mathbf{P}. \tag{2.7}$$

Here $\mathbf{P}$ is the polarization field defined as $\mathbf{P} = \chi\varepsilon_0\mathbf{E}$, and χ is the electric susceptibility of the medium ($\chi = 1 - \varepsilon_1$).

Using Eqs. (2.6) and (2.7), the equation for electrostatics in the medium becomes

$$\varepsilon_0\nabla \cdot \varepsilon_1\mathbf{E} = \rho^f, \tag{2.8}$$

or

$$\nabla \cdot \mathbf{D} = \rho^f. \tag{2.9}$$

In a medium, the constitutive relation between $\mathbf{D}$ and $\mathbf{E}$ is the following:

$$\mathbf{D} = \varepsilon_0\mathbf{E} + \mathbf{P}. \tag{2.10}$$

For a linear dielectric, it becomes $\mathbf{D} = \epsilon\mathbf{E}$, where ϵ is the permittivity defined as $\epsilon = \varepsilon_0\varepsilon_1$.

Using Eqs. (2.4) and (2.8), for a homogenous, linear medium, the Poisson equation is

$$\nabla^2\phi = -\frac{\rho^f}{\varepsilon_1\varepsilon_0}. \tag{2.11}$$

The Poisson equation can be used to obtain the governing equations for the electric potential in different media.

2.2 Governing equations for electric potential

In this section, the governing equations (GEs) for the electric potential are provided for different medias. Particularly, for an electrolyte solution, metallic, dielectric and semiconducting substances.

2.2.1 GE for electrolyte solution

As was mentioned above the electric potential should satisfy the Poisson equation

$$\nabla^2\phi = -\frac{\rho^f}{\varepsilon_1\varepsilon_0}, \tag{2.12}$$

where ρ^f is the free-charge density produced by ionic concentration [3], and ε_1 is the dielectric constant of an electrolyte solution. There are two competitive forces acting on the ions in an electrolyte solution. They are diffusive and electric forces. To maintain the equilibrium the following condition should be satisfied [3]

$$k_B T \nabla \ln n_k + q z_k \nabla \phi = 0, \tag{2.13}$$

where k_B is the Boltzmann constant, T is the temperature, $\mu = k_B T \ln n_k$ is the chemical potential of the kth type of ion in the solution, n_k is the number densities of kth type of ion, ϕ is the electric potential, z_k is the valence of the kth type of ion, and q is the unsigned charge of an electron. The first term represents the diffusive force, and the latter one represents the electric force. Thus the ions follow the Boltzmann distribution

$$n_k = n_k^0 \exp\left[\frac{-z_k q \phi}{k_B T}\right], \tag{2.14}$$

where n_k^0 is the bulk number density of kth type of ion. The free-charge density ρ^f is equal to the local excess of ionic charges arising from N ionic species, and it is related to the number density n_k by the following expression

$$\rho^f = \sum_{k=1}^{N} z_k q n_k. \tag{2.15}$$

Therefore, the Poisson-Boltzmann (PB) equation describing the electric potential in an electrolyte solution has the following form

$$\nabla^2 \phi = -\sum_k \frac{z q n_k^0}{\varepsilon_1 \varepsilon_0} \exp\left[\frac{-z_k q \phi}{k_B T}\right], \tag{2.16}$$

ε_1 is the dielectric constant of the solution.

The PB equation is a non-linear second order partial differential equation, the analytical solution is only possible for simple geometries [3]. When the electric potential energy is smaller than the thermal energy, that is

$$\left|\frac{q\phi}{k_B T}\right| << 1, \tag{2.17}$$

the PB equation can be linearized as

$$\nabla^2 \phi = \frac{z_k^2 q^2 n_k^0}{\varepsilon_1 \varepsilon_0 k_B T} \phi = k^2 \phi, \tag{2.18}$$

where $1/k$ is the Debye length of the electrolyte solution [3]. Equation (2.18) is called the Debye-Hückel equation.

2.2.2 GE for responsive substances

Semiconducting substance

The governing equation for the electric potential for a semiconductor can also be obtained from the Poisson equation in the following form [4]

$$\nabla^2\phi = -\frac{q}{\varepsilon_2\varepsilon_0}\left(p - n + N_D - N_A\right), \tag{2.19}$$

where N_D is the number density of ionized donors, N_A is the number density of ionized acceptors. In semiconductors, at room temperatures and without many impurities, the Boltzmann distribution is a good approximation [4], therefore, $p = n_i \exp(E_F/k_BT)$ is the number density of holes, $n = n_i \exp(-E_F/k_BT)$ is the number density of electrons, E_F is the Fermi level of the electrons, and n_i is the intrinsic carrier density [4] defined as

$$n_i = \sqrt{N_C N_V}\exp\left(-\frac{E_C - E_V}{2k_BT}\right). \tag{2.20}$$

Here, E_C and E_V are the bottom of the conduction band and the top of the valence band, respectively. N_C and N_V are the effective density of states in the conduction and the valence band, respectively [4]. For the uniformly doped semiconductor, N_D and N_A are independent of position.

Far from the surface the electric potential and all its derivatives are zero, it leads to the following condition

$$N_D - N_A = 2n_i \sinh\frac{E_F}{k_BT}, \tag{2.21}$$

and using the definitions of p and n, we have

$$p - n = 2n_i \sinh\frac{E_F}{k_BT}. \tag{2.22}$$

Therefore, Eq. (2.19) becomes

$$\nabla^2\phi = \frac{2n_i q}{\varepsilon_2\varepsilon_0}\left(\sinh\frac{q\phi + E_F}{k_BT} - \sinh\frac{E_F}{k_BT}\right). \tag{2.23}$$

Under the assumption that the electric potential is small inside a semiconductor, $q\phi/k_BT << 1$, Eq. (2.23) can be linearized as

$$\nabla^2\phi = k_2^2\phi, \tag{2.24}$$

where $1/k_2$ is the Debye length in the semiconductor [4] defined as

$$k_2^2 = \frac{2n_i q^2}{\varepsilon_2 \varepsilon_0 k_B T} \cosh \frac{E_F}{k_B T}. \tag{2.25}$$

Dielectric and metallic substances

There no free charges inside of a dielectric, that is, $\rho_f = 0$. Therefore, Eq. (2.11) becomes

$$\nabla^2 \phi = 0. \tag{2.26}$$

This means that the electric potential inside the dielectric matter is governed by the Laplace equation [5].

At equilibrium, the electric field inside of the metallic substance is zero [5]. This implies that the electric potential is constant inside of the metallic substance. For a grounded metallic substance, the electric potential is zero.

2.3 Boundary conditions

It will be shown below that the Maxwell equations written in the integral form can be used to derive boundary conditions (BCs) for surfaces between different media.

After applying the divergence theorem to Eq. (2.9), the Maxwell equation can be represented in the integral form

$$\oint_{S_\rho} \mathbf{D} \cdot \mathbf{n} da = \int_V \rho^f d^3x. \tag{2.27}$$

where S_ρ is the closed surface binding a finite volume V in space, da is an element of area on the surface, $\mathbf{n}$ is a unit vector normal to the surface at da point outward from V, and ρ^f is the free-charge density. This equation is Gauss' law, which states that the net flux $\mathbf{D}$ across a closed surface is equal to the charge contained inside.

The condition of discontinuity of the electric displacement can be obtained from the Gauss law. Let us consider a very shallow pillbox where the top and bottom sides are parallel to the surface as depicted in Figure 2.1 . Here, the area of the top and bottom sides of the pillbox is $\triangle a$. By applying Eq. (2.27) to this pillbox, the

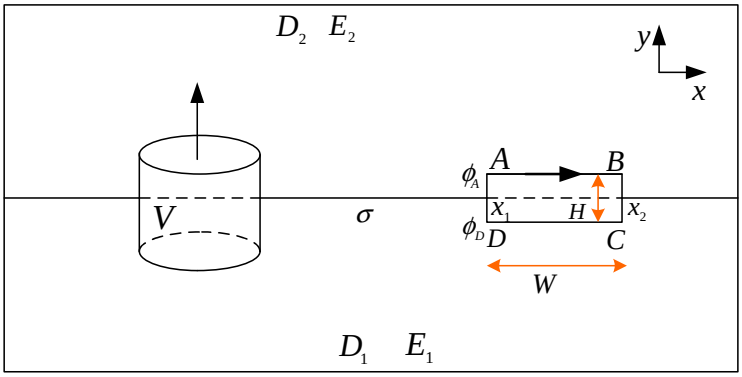

Figure 2.1: Diagram of the surface between two different types of media. The boundary between the two media carries a uniform surface charge density σ. The pillbox has volume V, and $\triangle a$ is the area of the top or bottom sides of the pillbox. The pillbox is located in the middle of two media. The normal vector $\mathbf{n}$ on the pillbox has direction from medium 1 to medium 2. $ABCD$ is a rectangular contour partly in both media. $\mathbf{E}_1$ and $\mathbf{D}_1$ are the electric field and the electric displacement in the medium 1. $\mathbf{E}_2$ and $\mathbf{D}_2$ are in medium 2, respectively.

integral on the left side takes the following form

$$\oint_{S_\rho} \mathbf{D} \cdot \mathbf{n} da = (\mathbf{D}_2 - \mathbf{D}_1) \cdot \mathbf{n} \triangle a. \tag{2.28}$$

Whereas the integral on the right side becomes

$$\int_V \rho^f d^3x = \sigma \triangle a. \tag{2.29}$$

Thus the normal components of $\mathbf{D}$ on either side of the boundary surface are related to

$$(\mathbf{D}_2 - \mathbf{D}_1) \cdot \mathbf{n} = \sigma. \tag{2.30}$$

This is the condition of discontinuity of the electric displacement across the interface. When $\sigma = 0$, it becomes a condition of continuity of the normal component of the electric displacement.

Another BC can be obtained by using Kelvin-Stoke's theorem for Eq. (2.2), that is

$$\oint_C \mathbf{E} \cdot d\mathbf{l} = \int_{S_c} \nabla \times \mathbf{E} \cdot d\mathbf{A} = 0, \tag{2.31}$$

where C is a closed contour in space, $d\mathbf{l}$ is a length element on the contour, S_c is an open surface spanning the contour C, and $d\mathbf{A}$ is a surface element on S_c with normal pointing outwards. Consider C to be the boundary of the contour $ABCD$ (See Figure 2.1). For the infinitesimal contour, the height H shrinks to zero, and the area of the surface S_c becomes zero. Therefore, we have

$$\oint_C \mathbf{E} \cdot d\mathbf{l} = 0, \tag{2.32}$$

which is equivalent to

$$\int_A^B \mathbf{E} \cdot d\mathbf{l} + \int_B^C \mathbf{E} \cdot d\mathbf{l} + \int_C^D \mathbf{E} \cdot \mathbf{dl} + \int_D^A \mathbf{E} \cdot d\mathbf{l} = 0, \tag{2.33}$$

as $H \to 0$, the second and the forth integrals become zero; hence

$$\int_A^B \mathbf{E} \cdot d\mathbf{l} + \int_C^D \mathbf{E} \cdot d\mathbf{l} = 0, \tag{2.34}$$

that is,

$$\int_A^B \mathbf{E}^{top} \cdot d\mathbf{l} - \int_D^C \mathbf{E}^{bottom} \cdot d\mathbf{l} = 0, \tag{2.35}$$

where $\mathbf{E}^{top}$ and $\mathbf{E}^{bottom}$ are the electric field on the top and bottom of the interface, respectively. From the equation above it follows that

$$\int_{x_1}^{x_2} \left(E_x^{top} - E_x^{bottom}\right) dx = 0. \tag{2.36}$$

This equation needs to be satisfied for any arbitrary path (i.e. $\forall\ x_1, x_2$); therefore the integral is zero only if the integrand is zero, resulting in

$$E_x^{top} = E_x^{bottom}. \tag{2.37}$$

This is the condition of continuity of the tangential component of the electric field. Also consider the electric potential

$$\phi_A - \phi_D = \int_D^A d\phi = \int_D^A \frac{\partial \phi}{\partial y} dy = \int_D^A (-E_y)\, dy = \int_D^A (-\mathbf{E}) \cdot d\ell. \tag{2.38}$$

Therefore

$$\phi_A + \int_D^A (-\mathbf{E}) \cdot d\mathbf{l} = \phi_D. \tag{2.39}$$

For a finite electric field, as $H \to 0$, the integral approaches zero, leaving

$$\phi_A = \phi_D, \ H \to 0. \tag{2.40}$$

This is the condition of continuity of the electric potential across the interface.

Bibliography

[1] J. Jackson, *Classical electrodynamics.* Wiley, 1999.

[2] R.P. Feynman, R.B. Leighton, M. Sands, *Feynman Lectures on Physics*, vol.2, Oxford, Addison-Wesley Publishing Company, Inc., 1964.

[3] W. B. Russel, *Colloidal Dispersions.* Cambridge Univ. Press, Cambridge, UK, 1989.

[4] A. Nussbaum, *Semiconductor Device Physics.* Prentice-Hall, NJ, 1962.

[5] Landau, L.D. and Lifshitz, E.M. and Pitaevskii, L.P., *Electrodynamics of continuous media,* Butterworth-Heinemann, 1984.

Chapter 3
Adhesion between a charged particle in an electrolyte solution and a charged substrate: Electrostatic and van der Waals interactions[1]

3.1 Introduction

The understanding of the interactions between charged molecules and substrates is of the utmost importance in both theoretical modeling and practical applications. For example, DNA biosensors involve immobilization and hybridization of DNA on surfaces of different electronic and chemical properties [1–5]; conductance change of nanowire nanosensors due to binding of charged molecules to receptors on a device surface has enabled ultra sensitive detection of virus and DNA sequences [6, 7]; recently, single-strand DNA (ssDNA) molecules have been found to have the ability to form a helical wrapping on the surface of a carbon nanotube (CNT) through π-stacking - the behaviors of the DNA-CNT hybrids vary with the electronic property of the CNT core (i.e., metal or semiconductor) allowing effective dispersion and separation of CNTs [8, 9]. In the area of cell adhesion and spreading, the nature of the substrate, its surface characteristics and charge densities are among the many factors that influence, for example, cell adhesion to natural or synthetic substrates which is an important area related to wound healing, tissue regeneration and many other medical applications [10–12]. Recent work by Hong and Brown [13] studied the electrostatic behavior of the charge regulated bacterial surface, which plays an important role in bacterial interactions with other surfaces and for bacterial adhesion. Manohar et al. [14] determined the binding energy between a nucleotide and

[1]Reprinted from Journal of Colloid and Interface Science, Volume 327, Malysheva O., Tang T., Schiavone P., "Adhesion between a charged particle in an electrolyte solution and a charged substrate: Electrostatic and van der Waals interactions", Pages 251-260, Copyright 2008, with permission from Elsevier.

graphite by using an AFM tip functionalized with a charged single-stranded DNA molecule and subsequently pulling the AFM tip from a graphite surface, which again involves interactions between charged objects and substrate. The majority of the aforementioned applications occur in an electrolytic environment. It is therefore of great interest to understand the interaction between charged molecules and substrates in electrolyte solutions, in particular when the substrate responds electronically to charge.

Approaches at different scales have been used to investigate and model the electrostatics of charged particles and polyions in electrolyte solutions. At the atomistic level, molecular simulations have enabled the study of the configuration and energetics of charged molecules in explicit solvents [15–22]. At the continuum level, the solvent has been represented by an effective dielectric medium [23], and the screening effect of the ions in the solution can be characterized using the Poisson-Boltzmann (PB) equation for the electric potential [24]

$$\nabla^2\phi = -\sum_i \frac{z_i q n_i^0}{\varepsilon_1\varepsilon_0} \exp\left[\frac{-z_i q\phi}{k_B T}\right], \tag{3.1}$$

In Eq. (3.1), ϕ is the electric potential in the solution, q is the unsigned charge of an electron, z_i and n_i^0 are respectively the valence and bulk number density of the i^{th} species of ions, ε_0 is the permittivity of free space, ε_1 is the dielectric constant of the solution, k_B is the Boltzmann constant and T is the temperature. The continuum approach significantly reduces the degrees of freedom of the solvent and allows studies on a much larger system than that which could be otherwise achieved by molecular simulations. Indeed, the PB equation has been widely used to capture the electrostatic interactions in many biological systems (for example, see the review by Fogolari et al. [25]).

In the case when the electric potential satisfies the estimate

$$\frac{q\phi}{k_B T} << 1, \tag{3.2}$$

Eq. (3.1) can be linearized to the well-known Debye-Hückel (DH) equation

$$\nabla^2\phi = k^2\phi, \tag{3.3}$$

where $1/k$ is the Debye length given by

$$k^2 = 4\pi l_B \sum_i z_i^2 n_i^0, \tag{3.4}$$

and $l_B = q^2/4\pi\varepsilon_0\varepsilon_1 k_B T$ is the Bjerrum length. The linearity of the DH equation means that analytic solutions ϕ can be obtained in many geometries. This is usually not possible for the original PB equation. In the case of certain polyions, however (especially biomolecules), the charge density is so high that the electric potential cannot be described by the linearized PB equation. To resolve the issue, Manning [26–28] proposed that the counterions in the solution will condense on the polyion to effectively reduce its charge density so that the electric potential in the solution can still be calculated using the DH equation with a modified polyion charge density. This theory of counterion condensation allows the electric potential to be represented analytically and has been widely used to characterize the electrostatics of highly charged molecules in electrolyte solution [29–33].

To date, most of the corresponding studies involving electrostatics in electrolyte solutions do not take into account the interaction between a charged molecule and a substrate when the substrate is known to respond to external charges electronically. To incorporate this effect, Tang et al. [34, 35] studied the counterion condensation of a line of charges near an uncharged metallic, dielectric or semiconducting substrate by solving the DH equation analytically. It was found that the behavior of the line of charges varies significantly depending on the substrate. In particular, when the line of charges is moved from the bulk solution to a metallic substrate, the counterions previously condensed on the polyion must all be released. On the other hand, the counterion condensation can increase, decrease, or remain unchanged near a dielectric substrate, depending on the value of its dielectric constant.

The van der Waals interaction is another universal interaction that is often considered significant in a molecule-substrate system. In fact, the interplay between electrostatic and van der Waals interactions is captured in the classical Derjaguin-Landau-Verwey-Overbeek (DLVO) theory [36]. In this theory, the total free energy between a charged molecule and a substrate is taken as the sum of the electrostatic and van der Waals free energies. The resulting local energy minima correspond to

equilibrium states of the molecule and determine its separation from the substrate. The equilibrium separation and the depth of the energy well at those local minima are both measures of the strength of the adhesion between the molecule and the substrate, which is an important factor in applications (see, for example, [37]).

In this paper, we consider the adhesion of a charged particle to an electronically responsive substrate with surface charge. In particular, we are interested in the equilibrium separation between the particle and the substrate and how this separation is affected by the surface charge of the substrate. We adopt the idea of the DLVO theory and incorporate the interplay of the electrostatics and van der Waals interactions. This often results in an equilibrium separation at short range, which we define as the "attached" state. Also, for sufficiently large separation, the interaction between the particle and the substrate becomes negligible, and we define this state as the "detached" state. We demonstrate how the location of the attached state and the transition from the detached state to the attached state are affected by the nature of the substrate (metal, dielectric, or semiconductor) and its surface charge.

The paper is organized as follows. In Section 3.2, we describe the physical problem and the mathematical approach. In Section 3.3, we calculate the electric potential due to a charged particle interacting with different types of substrates. We assume that the electric potential is sufficiently small so that the DH equation applies. This allows us to obtain the electric potential analytically. The electrostatic free energy between the particle and the substrate is then evaluated in Section 3.4. In Section 3.5, we derive expression for the van der Waals free energy between the particle and the substrate by integrating the Lennard-Jones (LJ) potential [38]. The equilibrium separation between the particle and the substrate is obtained in Section 3.6 using the DLVO theory. Finally, conclusions and discussion are given in Section 3.7.

3.2 Problem description

Consider a substrate with initially uniform charge density σ located in an electrolyte solution (see Figure 3.1). The substrate occupies the lower half space $z < 0$, and

the electrolyte solution occupies the upper half space $z > 0$. A particle of charge $Q = nq$ is located at a distance d above the substrate. Here q is the unsigned charge of an electron and n is an integer describing the total charge of the particle. The electrolyte solution has associated dielectric constant ε_1 and Debye length k_1^{-1}. The substrate can take the form of a metal, a dielectric (with dielectric constant ε_2) or a semiconductor (with dielectric constant ε_2 and Debye length k_2^{-1}). The electric potential in $z > 0$ is governed by the DH equation, while the equation governing the electric potential in the $z < 0$ depends on the electronic nature of the substrate and will be discussed separately in Section 3.3.

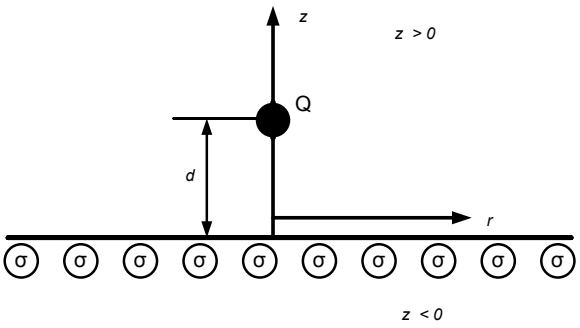

Figure 3.1: A particle of charge Q above a substrate with initially uniform surface charge density of σ. The upper half space ($z > 0$) is an electrolyte solution with dielectric constant ε_1 and Debye length k_1^{-1}. The lower half space ($z < 0$) can be a metal, a dielectric with dielectric constant ε_2 or a semiconductor with a dielectric constant ε_2 and Debye length k_2^{-1}.

As is demonstrated in Section 3.3, the boundary value problem (BVP) for the electric potential is linear for all three types of substrate (metal, dielectric and semiconductor). Consequently, we solve for the electric potential due to the charged particle and subsequently the electric potential due to the surface charge separately and then obtain the total solution by superposition. In addition, we make use of the Hankel transform technique [39] utilizing the axisymmetric nature of the problem considered (i.e., $\phi = \phi(r, z)$, r and z being the cylindrical coordinates shown in Figure 3.1). The electrostatic free energy is then calculated form the electric potential and the van der Waals free energy is found by integrating the pairwise 6-12 LJ potential between a particle and a substrate. The total free energy is then used to

determine the equilibrium separation between the particle and the substrate.

3.3 Electric potential of a charged particle near a substrate with surface charge

In this section, we establish the necessary governing equations and boundary conditions for the electric potential. This potential, obtained in closed form, is then used in Section 3.4 to calculate the electrostatic free energy.

3.3.1 Metallic substrate

For a metallic substrate, the differential equation and boundary conditions for the electric potential ϕ_Q in $z > 0$ due to the charge Q only are given by

$$\nabla^2 \phi_Q(r, z > 0) = k_1^2 \phi_Q(r, z > 0), \tag{3.5a}$$

$$\phi_Q(r, z = 0) = 0, \tag{3.5b}$$

$$\lim_{S_{Q\to 0}} \oint_{S_Q} (-\varepsilon_0 \varepsilon_1 \nabla \phi_Q) \cdot \mathbf{n} dA = Q. \tag{3.5c}$$

where S_Q denotes a surface enclosing the charge Q, and $\mathbf{n}$ is its outer unit normal. The solution ϕ_Q can be obtained by the method of images [40] and is given by

$$\phi_Q(r, z > 0) = \frac{Q}{4\pi\varepsilon_0\varepsilon_1} \left[\frac{e^{-k_1\sqrt{r^2+(z-d)^2}}}{\sqrt{r^2+(z-d)^2}} - \frac{e^{-k_1\sqrt{r^2+(z+d)^2}}}{\sqrt{r^2+(z+d)^2}} \right]. \tag{3.6}$$

The differential equation and boundary conditions for the electric potential ϕ_σ due to the initially uniform surface charge σ are given by

$$\nabla^2 \phi_\sigma(r, z > 0) = k_1^2 \phi_\sigma(r, z > 0), \tag{3.7a}$$

$$-\lim_{z\to 0+} \varepsilon_1 \frac{\partial \phi_\sigma}{\partial z} = \frac{\sigma}{\varepsilon_0}. \tag{3.7b}$$

The solution is found to be

$$\phi_\sigma(r, z > 0) = \frac{\sigma e^{-k_1 z}}{k_1 \varepsilon_0 \varepsilon_1}. \tag{3.8}$$

The total electric potential in $z > 0$ is the sum of Eqs. (3.6) and (3.8)

$$\phi(r, z > 0) = \frac{Q}{4\pi\varepsilon_0\varepsilon_1} \left[\frac{e^{-k_1\sqrt{r^2+(z-d)^2}}}{\sqrt{r^2+(z-d)^2}} - \frac{e^{-k_1\sqrt{r^2+(z+d)^2}}}{\sqrt{r^2+(z+d)^2}} \right] + \frac{\sigma e^{-k_1 z}}{k_1 \varepsilon_0 \varepsilon_1}. \tag{3.9}$$

It should be noted that the final charge distribution on the surface ($z = 0$) of the metal is non-uniform since the charges are allowed to move under the influence of the point charge Q.

Figure 3.2 plots the contours of the normalized electric potential $4\pi\varepsilon_0\varepsilon_1\phi d/Q$ for a fixed value $k_1 d = 1$ and three different values of the normalized surface charge $\sigma d^2/Q$. Figure 3.2 (a) shows that for intermediate $\sigma d^2/Q$, the main contribution to the electric potential near the charge comes from Q itself, indicated by the nearly circular contour around Q. As the distance from the charge increases, the effect of the surface charge becomes stronger. Also, far from the charge, the contours are almost parallel to the surface, indicating that the contribution from the point charge is negligible. For very large $\sigma d^2/Q$ (see Figure 3.2 (b)) and very small $\sigma d^2/Q$ (see Figure 3.2 (c)), the electric potential is governed by the surface charge and the point charge, respectively .

3.3.2 Dielectric substrate

In the case of a dielectric substrate, the differential equations governing the electric potential in $z > 0$ and $z < 0$ are, respectively

$$\nabla^2\phi(r, z > 0) = k_1^2\phi(r, z > 0), \tag{3.10a}$$

$$\nabla^2\phi(r, z < 0) = 0. \tag{3.10b}$$

The boundary conditions are

$$\lim_{S_{Q\to 0}} \oint_{S_Q} (-\varepsilon_0\varepsilon_1\nabla\phi)\cdot\mathbf{n}dA = Q, \tag{3.11a}$$

$$\lim_{z\to 0+}\phi = \lim_{z\to 0-}\phi, \tag{3.11b}$$

$$\lim_{z\to 0-}\varepsilon_2\frac{\partial\phi}{\partial z} - \lim_{z\to 0+}\varepsilon_1\frac{\partial\phi}{\partial z} = \frac{\sigma}{\varepsilon_0}, \tag{3.11c}$$

$$\phi(r, z\to\infty)\to 0, \tag{3.11d}$$

$$\phi(r, z\to -L) = 0. \tag{3.11e}$$

Eq. (3.11a) is the condition for the point charge Q. Eq. (3.11b) is the continuity condition for the electric potential on the interface, and Eq. (3.11c) describes the surface charge density σ on the interface. Eq. (3.11d) describes the requirement that

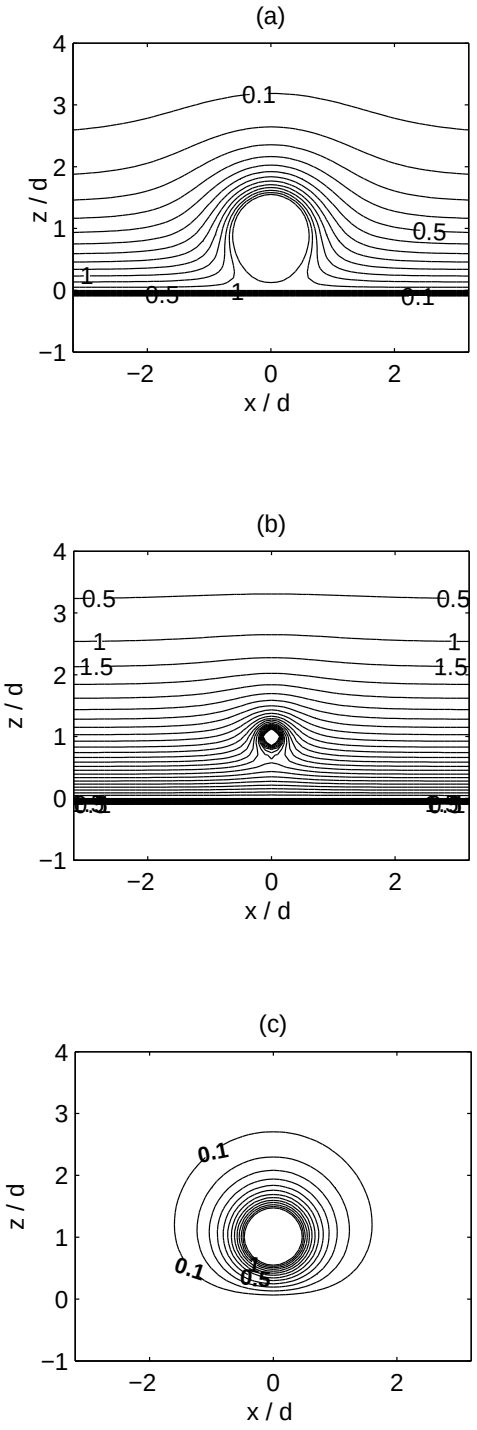

Figure 3.2: Normalized electric potential $4\pi\varepsilon_0\varepsilon_1\phi d/Q$ of a charged particle Q above a metallic substrate with initially uniform surface charge density σ. The three cases correspond to the same $k_1 d = 1$ and different values of $\sigma d^2/Q$: (a) $\sigma d^2/Q = 0.1$, (b)$\sigma d^2/Q = 1$, (c) $\sigma d^2/Q = 0.0001$.

ϕ vanishes far away from the charge in the electrolyte solution. Eq. (3.11e) implies that ϕ is zero at a distance L below the interface. This condition is necessary since the electric potential due to a uniform surface charge varies linearly in a dielectric and it is necessary to define a suitable reference energy. Physically, L is of the order of the characteristic length of the substrate, e.g., its thickness.

To solve Eqs. (3.10a) – (3.11e), we use the same approach as in [35]. Firstly, we assume that the electric potential on the interface $z = 0$ is some unknown function $\phi_0(r)$

$$\phi(r, 0) = \phi_0(r). \tag{3.12}$$

With Eq. (3.12), the electric potential ϕ, which satisfies Eq. (3.11b), in both $z > 0$ and $z < 0$ can be found separately in terms of ϕ_0. Finally, $\phi_0(r)$ is determined using the boundary condition Eq. (3.11c).

Upper half space, $z > 0$

Eqs. (3.10a), (3.11a), (3.11d) and (3.12) define the BVP for $\phi(r, z > 0)$. Due to axisymmetry, $\phi(r, z > 0)$ can be obtained using the Hankel transform of order zero [39]. The solution has been obtained in [35] and is given by

$$\phi(r, z > 0) = \frac{Q}{4\pi\varepsilon_0\varepsilon_1}\left[\frac{e^{-k_1\sqrt{r^2+(z-d)^2}}}{\sqrt{r^2+(z-d)^2}} - \frac{e^{-k_1\sqrt{r^2+(z+d)^2}}}{\sqrt{r^2+(z+d)^2}}\right] + \int_0^\infty \rho\Phi_0(\rho)e^{-z\sqrt{\rho^2+k_1^2}}J_0(\rho r)d\rho. \tag{3.13}$$

where Φ_0 is the Hankel transform of order 0 in the unknown potential ϕ_0 on the interface and J_0 is the 0^{th} order Bessel function of the first kind.

Lower half space, $z < 0$

Applying the Hankel transform to r in Eqs. (3.10b), (3.11e) and (3.12) results in the following transformed BVP in $z < 0$

$$\frac{\partial^2\Phi(\rho, z < 0)}{\partial z^2} - \rho^2\Phi(\rho, z < 0) = 0, \tag{3.14a}$$

$$\Phi(\rho, z \to -L) = 0, \tag{3.14b}$$

$$\Phi(\rho, 0) = \Phi_0(\rho). \tag{3.14c}$$

where $\Phi(r, z < 0)$ is the Hankel transform of order 0 in $\phi(r, z < 0)$. The solution to Eqs. (3.14a) – (3.14c) is given by

$$\Phi(\rho, z < 0) = \Phi_0(\rho)\frac{e^{\rho(z+L)} - e^{-\rho(z+L)}}{e^{\rho L} - e^{-\rho L}}, \tag{3.15}$$

which, in turn, gives the solution to the original BVP in $z < 0$ as

$$\phi(r, z < 0) = \int_0^\infty \rho\Phi_0(\rho)\frac{e^{\rho(z+L)} - e^{-\rho(z+L)}}{e^{\rho L} - e^{-\rho L}}J_0(\rho r)d\rho. \tag{3.16}$$

Boundary condition

To solve for the unknown function $\Phi_0(\rho)$ we substitute Eqs. (3.13) and (3.16) into the boundary condition Eq. (3.11c) and obtain the following equation

$$\int_0^\infty \rho\left[\varepsilon_2\rho\frac{1 + e^{-2\rho L}}{1 - e^{-2\rho L}} + \varepsilon_1\sqrt{\rho^2 + k_1^2}\right]\Phi_0(\rho)J_0(\rho r)d\rho = \\ = \frac{\sigma}{\varepsilon_0} + \frac{Qde^{-k_1\sqrt{r^2+d^2}}}{2\pi\varepsilon_0(r^2 + d^2)}\left(\frac{1}{\sqrt{r^2 + d^2}} + k_1\right), \tag{3.17}$$

which is an integral equation for $\Phi_0(\rho)$. After $\Phi_0(\rho)$ is obtained, the electrical potentials in the upper and lower half spaces are completely determined by Eqs. (3.13) and (3.16).

The left-hand side of Eq. (3.17) is indeed the inverse Hankel transform (of order zero) of the function $\left[\varepsilon_2\rho(1 + e^{-2\rho L})/(1 - e^{-2\rho L}) + \varepsilon_1\sqrt{\rho^2 + k_1^2}\right]\Phi_0(\rho)$. Therefore, applying the Hankel transform on both sides of Eq. (3.17) gives

$$\left[\varepsilon_2\rho\frac{1 + e^{-2\rho L}}{1 - e^{-2\rho L}} + \varepsilon_1\sqrt{\rho^2 + k_1^2}\right]\Phi_0(\rho) = \frac{\sigma}{\varepsilon_0}\int_0^\infty rJ_0(\rho r)dr \\ + \frac{Qd}{2\pi\varepsilon_0}\int_0^\infty r\frac{e^{-k_1\sqrt{r^2+d^2}}}{(r^2 + d^2)}\left(\frac{1}{\sqrt{r^2 + d^2}} + k_1\right)J_0(\rho r)dr. \tag{3.18}$$

The first and second integrals on the right-hand side of Eq. (3.18) are, respectively, given by $\delta(\rho)/\rho$ and $e^{-d\sqrt{\rho^2+k_1^2}}/d$ [41]. Consequently,

$$\Phi_0(\rho) = \frac{\sigma\delta(\rho)}{\varepsilon_0\rho\left[\varepsilon_2\rho\frac{1+e^{-2\rho L}}{1-e^{-2\rho L}} + \varepsilon_1\sqrt{\rho^2 + k_1^2}\right]} \\ + \frac{Qe^{-d\sqrt{\rho^2+k_1^2}}}{2\pi\varepsilon_0\left[\varepsilon_2\rho\frac{1+e^{-2\rho L}}{1-e^{-2\rho L}} + \varepsilon_1\sqrt{\rho^2 + k_1^2}\right]}. \tag{3.19}$$

The electric potentials in the upper and lower half spaces can now be obtained by substituting Eq. (3.19) into Eqs. (3.13) and (3.16), which results in

$$\phi(r, z > 0) = \frac{Q}{4\pi\varepsilon_0\varepsilon_1}\left[\frac{e^{-k_1\sqrt{r^2+(z-d)^2}}}{\sqrt{r^2+(z-d)^2}} - \frac{e^{-k_1\sqrt{r^2+(z+d)^2}}}{\sqrt{r^2+(z+d)^2}}\right] + \frac{Q}{2\pi\varepsilon_0}\int_0^\infty \frac{\rho e^{-(z+d)\sqrt{\rho^2+k_1^2}} J_0(\rho r)}{\left[\varepsilon_2\rho\frac{1+e^{-2\rho L}}{1-e^{-2\rho L}} + \varepsilon_1\sqrt{\rho^2+k_1^2}\right]} d\rho + \frac{\sigma e^{-zk_1}L}{\varepsilon_0(\varepsilon_1 k_1 L + \varepsilon_2)}, \quad (3.20)$$

$$\phi(r, z < 0) = \frac{Q}{2\pi\varepsilon_0}\int_0^\infty \frac{\rho e^{-d\sqrt{\rho^2+k_1^2}}}{\left(\varepsilon_2\rho\frac{1+e^{-2\rho L}}{1-e^{-2\rho L}} + \varepsilon_1\sqrt{\rho^2+k_1^2}\right)} \frac{e^{\rho(z+L)} - e^{-\rho(z+L)}}{e^{\rho L} - e^{-\rho L}} J_0(\rho r) d\rho + \frac{\sigma(L+z)}{\varepsilon_0(\varepsilon_1 k_1 L + \varepsilon_2)}. \quad (3.21)$$

The first two terms of the solution in Eq. (3.20) can be identified as the solution for a point charge Q above a metallic substrate. The third term is due to the nonzero potential on the interface. Compared with the solution for a substrate without surface charge [35], our solution has an additional factor $(1 + e^{-2\rho L})/(1 - e^{-2\rho L})$ which multiplies $\varepsilon_2\rho$ since the potential due to the surface charge is set to zero at $z = -L$. If we take $L \to \infty$, then $(1 + e^{-2\rho L})/(1 - e^{-2\rho L}) \to 1$, and the first three terms of Eq. (3.20) reduce to the exact solution of a point charge near an uncharged half space [35]. The final term of the solution in Eq. (3.20) is the electric potential due to the charged substrate alone, in the absence of the point charge.

Figure 3.3 shows the plots of the normalized electric potential $4\pi\varepsilon_0\varepsilon_1\phi d/Q$ of a charged particle Q above a dielectric substrate with surface charge density σ, for a series of different normalized surface charges $\sigma d^2/Q$ and fixed values of $k_1 d = 1, \varepsilon_2/\varepsilon_1 = 0.01$ and $L/d = 10$. Again, for $\sigma d^2/Q \geqslant 1$ (see Figure 3.3 (b)), the contribution from the point charge can be neglected while for $\sigma d^2/Q << 1$ (see Figure 3.3 (c)), the result is nearly identical to the case of a point charge alone [35]. For intermediate values of $\sigma d^2/Q$, the influence of the point charge and the surface charge are both significant (see Figure 3.3 (a)).

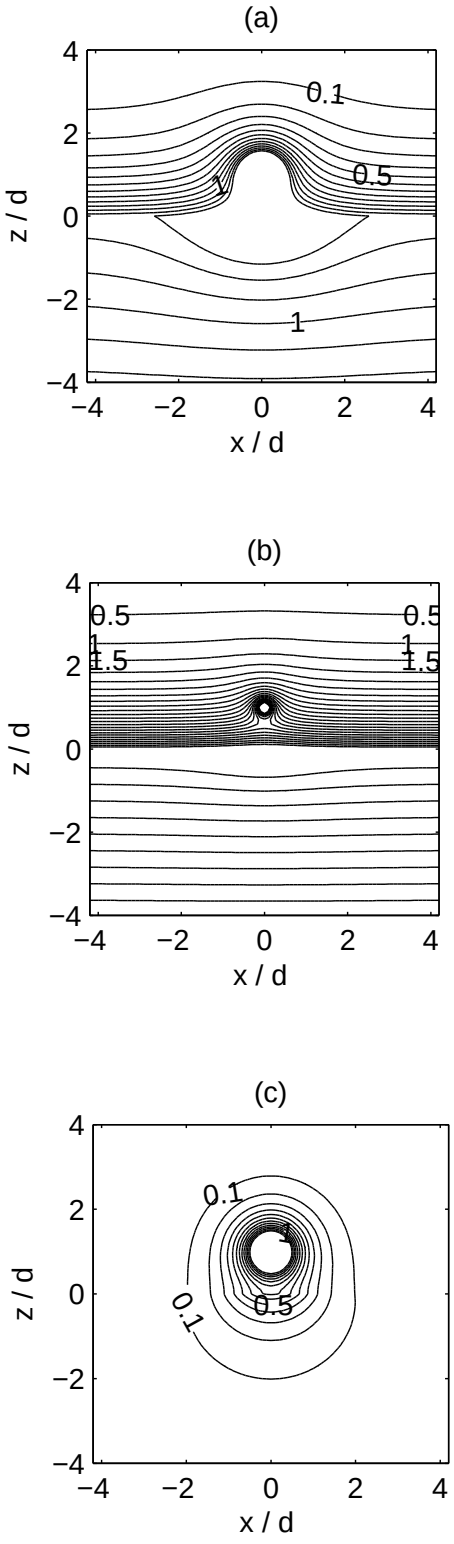

Figure 3.3: Normalized electric potential $4\pi\varepsilon_0\varepsilon_1 d\phi/Q$ of a charged particle Q above a dielectric substrate with surface charge density σ for three different values of $\sigma d^2/Q$: (a) $\sigma d^2/Q = 0.1$, (b) $\sigma d^2/Q = 1$, (c) $\sigma d^2/Q = 0.0001$. For all cases $k_1 d = 1$, $\varepsilon_2/\varepsilon_1 = 0.01$ and $L/d = 10$.

3.3.3 Semiconducting substrate

In $z > 0$, the electric potential satisfies the DH equation

$$\nabla^2\phi(r, z > 0) = k_1^2\phi(r, z > 0), \tag{3.22}$$

In $z < 0$, under the assumption that the electric potential satisfies Eq. (3.2), the Poisson equation for a semiconductor can be linearized to [34]

$$\nabla^2\phi(r, z < 0) = k_2^2\phi(r, z < 0). \tag{3.23}$$

Here k_2 is inverse Debye length of the semiconductor defined by

$$k_2^2 = \frac{2q^2 n_i}{\varepsilon_0\varepsilon_2 k_B T}\cosh\left(\frac{E_f}{k_B T}\right), \tag{3.24}$$

where n_i is the intrinsic carrier density and E_f is the difference between the current Fermi level and the intrinsic Fermi level of the electrons. The intrinsic carrier density, n_i, is proportional to $\exp(-E_g/2k_B T)$, where E_g is the band gap of the semiconductor.

The boundary conditions are

$$\lim_{S_{Q\to 0}} \oint_{S_Q} (-\varepsilon_0\varepsilon_1\nabla\phi)\cdot\mathbf{n}dA = Q, \tag{3.25a}$$

$$\lim_{z\to 0+}\phi = \lim_{z\to 0-}\phi, \tag{3.25b}$$

$$\lim_{z\to 0-}\varepsilon_2\frac{\partial\phi}{\partial z} - \lim_{z\to 0+}\varepsilon_1\frac{\partial\phi}{\partial z} = \frac{\sigma}{\varepsilon_0}, \tag{3.25c}$$

$$\phi(r, z\to\infty)\to 0, \tag{3.25d}$$

$$\phi(r, z\to -\infty)\to 0. \tag{3.25e}$$

Note that the boundary condition Eq. (3.25e) is different from Eq. (3.11e) for the case of a dielectric substrate, i.e. the characteristic length L is not necessary, since the electric potential decays exponentially in the semiconductor.

To find the electric potential we use the method described in Section 3.3.2 and [35]. That is, we first express ϕ in $z > 0$ and $z < 0$ in terms of the potential $\phi_0(r)$ on the interface, and then determine ϕ_0 using the boundary conditions.

Solution for $z > 0$ and $z < 0$

The solution for the electric potential in $z > 0$ in terms of $\phi_0(r)$ is given by [35]

$$\phi(r, z > 0) = \frac{Q}{4\pi\varepsilon_0\varepsilon_1}\left[\frac{e^{-k_1\sqrt{r^2+(z-d)^2}}}{\sqrt{r^2+(z-d)^2}} - \frac{e^{-k_1\sqrt{r^2+(z+d)^2}}}{\sqrt{r^2+(z+d)^2}}\right] + \int_0^\infty \rho\Phi_0(\rho)e^{-z\sqrt{\rho^2+k_1^2}}J_0(\rho r)d\rho, \quad (3.26)$$

and the solution for the electric potential in $z < 0$ is [35]

$$\phi(r, z < 0) = \int_0^\infty \rho\Phi_0(\rho)e^{z\sqrt{\rho^2+k_2^2}}J_0(\rho r)d\rho. \quad (3.27)$$

Boundary condition

Using Eqs. (3.26) and (3.27), (3.25c) becomes

$$\int_0^\infty \rho\left[\varepsilon_2\sqrt{\rho^2+k_2^2} + \varepsilon_1\sqrt{\rho^2+k_1^2}\right]\Phi_0(\rho)J_0(\rho r)d\rho = \frac{\sigma}{\varepsilon_0} + \frac{Qde^{-k_1\sqrt{r^2+d^2}}}{2\pi\varepsilon_0(r^2+d^2)}\left(\frac{1}{\sqrt{r^2+d^2}} + k_1\right). \quad (3.28)$$

$\Phi_0(\rho)$ can be obtained by applying a Hankel transform on both sides of Eq. (3.28). We obtain

$$\Phi_0(\rho) = \frac{\sigma\delta(\rho)}{\rho\varepsilon_0\left[\varepsilon_2\sqrt{\rho^2+k_2^2} + \varepsilon_1\sqrt{\rho^2+k_1^2}\right]} + \frac{Qe^{-d\sqrt{\rho^2+k_1^2}}}{2\pi\varepsilon_0\left[\varepsilon_2\sqrt{\rho^2+k_2^2} + \varepsilon_1\sqrt{\rho^2+k_1^2}\right]}. \quad (3.29)$$

The electric potentials Eqs. (3.26) and (3.27) are therefore given by

$$\phi(r, z > 0) = \frac{Q}{4\pi\varepsilon_0\varepsilon_1}\left[\frac{e^{-k_1\sqrt{r^2+(z-d)^2}}}{\sqrt{r^2+(z-d)^2}} - \frac{e^{-k_1\sqrt{r^2+(z+d)^2}}}{\sqrt{r^2+(z+d)^2}}\right] + \frac{Q}{2\pi\varepsilon_0}\int_0^\infty \frac{\rho e^{-(z+d)\sqrt{\rho^2+k_1^2}}J_0(\rho r)}{\left(\varepsilon_2\sqrt{\rho^2+k_2^2} + \varepsilon_1\sqrt{\rho^2+k_1^2}\right)}d\rho + \frac{\sigma e^{-zk_1}}{\varepsilon_0(\varepsilon_2k_2+\varepsilon_1k_1)}, \quad (3.30)$$

$$\phi(r, z < 0) = \frac{\sigma e^{zk_2}}{\varepsilon_0\left(\varepsilon_2k_2+\varepsilon_1k_1\right)}$$

$$+\frac{Q}{2\pi\varepsilon_0}\int_0^\infty \frac{\rho e^{z\sqrt{\rho^2+k_2^2}-d\sqrt{\rho^2+k_1^2}}}{\left(\varepsilon_2\sqrt{\rho^2+k_2^2}+\varepsilon_1\sqrt{\rho^2+k_1^2}\right)}J_0(\rho r)d\rho. \quad (3.31)$$

The solution $\phi(r, z > 0)$ in Eq. (3.30) can be interpreted as the sum of three parts. The first two terms can be identified as the solution for a point charge Q above a metallic substrate. The third term represents the solution due to the nonzero potential on the interface. The last term is due to the surface charge σ.

Figure 3.4 plots the contours of the normalized electric potential $4\pi\varepsilon_0\varepsilon_1\phi d/Q$ of a charged particle Q above a semiconductor substrate with surface charge density σ, for a series of different normalized surface charges $\sigma d^2/Q$ and with $k_1 d$, $k_2 d$ and $\varepsilon_2/\varepsilon_1$ fixed. We note behavior similar to the case of a dielectric substrate in that as the dimensionless quantity $\sigma d^2/Q$ decreases the effect of the surface charge also decreases. For $\sigma d^2/Q << 1$ the solution converges to the case of a charged particle only [35].

3.4 Electrostatic free energy

The electrostatic free energy due to the presence of the substrate is given by

$$G_{el} = Q\phi^*, \quad (3.32)$$

where ϕ^* is the electric potential evaluated at the location of the particle ($r = 0$, $z = d$) excluding the term $Qe^{-k_1\sqrt{r^2+(z-d)^2}}/4\pi\varepsilon_0\varepsilon_1\sqrt{r^2+(z-d)^2}$ due to the charge in the electrolyte solution alone (i.e., without the substrate).

To simplify the analysis, let us introduce the following normalization

$$g_{el} = \frac{G_{el}}{k_B T}, \quad \bar{k}_1 = k_1 l_B, \quad \overline{d} = \frac{d}{l_B}, \quad \overline{\sigma} = \frac{4\pi\sigma l_B^2}{q},$$
$$\overline{L} = \frac{L}{l_B}, \quad \varepsilon_{2/1} = \frac{\varepsilon_2}{\varepsilon_1}, \quad k_{2/1} = \frac{k_2}{k_1}, \quad \overline{\rho} = \rho d. \quad (3.33)$$

In Eq. (3.33) $\bar{k}_1$ is the normalized Debye length, which is a measure of the strength of the electrostatic interaction. $\overline{\sigma}$ is the normalized surface charge density. Substituting $\phi^* = \phi(r = 0, z = d) - Qe^{-k_1\sqrt{r^2+(z-d)^2}}/4\pi\varepsilon_0\varepsilon_1\sqrt{r^2+(z-d)^2}$ calculated from Eqs. (3.9) (metal), (3.20) (dielectric) and (3.30) (semiconductor) into

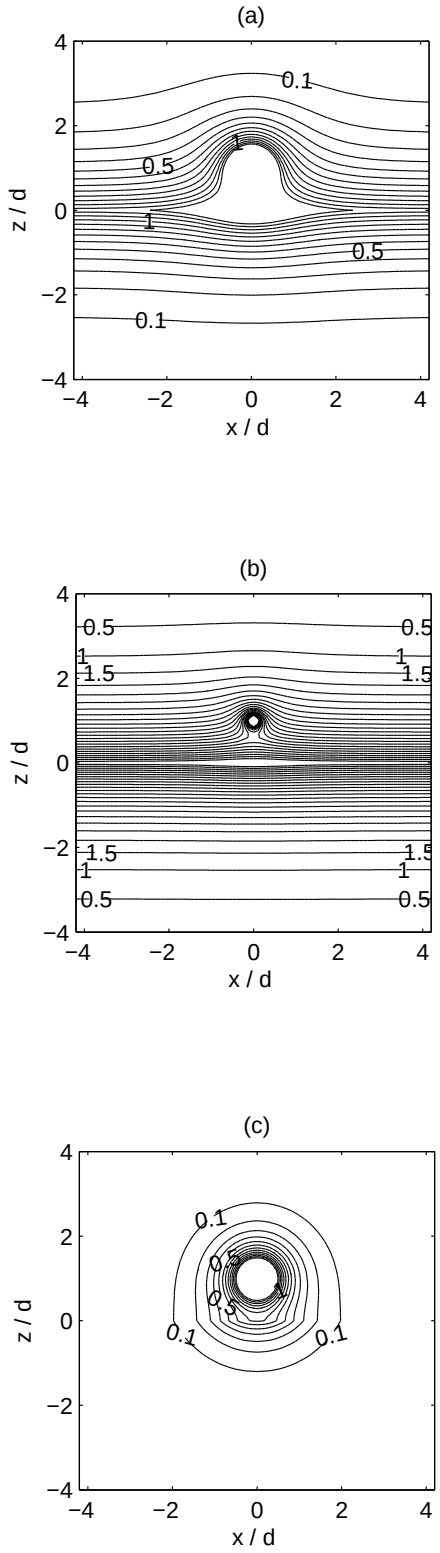

Figure 3.4: Normalized electric potential $4\pi\varepsilon_0\varepsilon_1 d\phi/Q$ of a charged particle above a semiconductor substrate with surface charge density σ for three different values of $\sigma d^2/Q$: (a) $\sigma d^2/Q = 0.1$, (b) $\sigma d^2/Q = 1$, (c) $\sigma d^2/Q = 0.0001$. For all cases $k_1 d = 1$, $k_2 d = 1$ and $\varepsilon_2/\varepsilon_1 = 0.01$.

Eq. (3.32), the normalized electrostatic free energies g_{el} in the cases of metallic, dielectric and semiconducting substrates are respectively given by

Metal:

$$g_{el} = -\frac{n^2 e^{-2\bar{k}_1 \overline{d}}}{2\overline{d}} + \frac{n\overline{\sigma} e^{-\bar{k}_1 \overline{d}}}{\bar{k}_1}. \tag{3.34}$$

Dielectric :

$$g_{el} = \frac{n^2}{2\overline{d}} \left[-e^{-2\bar{k}_1 \overline{d}} + 4 \int_0^\infty \frac{\overline{\rho} e^{-2\sqrt{\overline{\rho}^2 + (\bar{k}_1 \overline{d})^2}} d\overline{\rho}}{\varepsilon_{2/1} \overline{\rho} \frac{1+e^{-2\overline{\rho}\overline{L}/\overline{d}}}{1-e^{-2\overline{\rho}\overline{L}/\overline{d}}} + \sqrt{\overline{\rho}^2 + (\bar{k}_1 \overline{d})^2}} \right] + \frac{n\overline{\sigma} e^{-\bar{k}_1 \overline{d}} \overline{L}}{\bar{k}_1 \overline{L} + \varepsilon_{2/1}}. \tag{3.35}$$

Semiconductor :

$$g_{el} = \frac{n^2}{2\overline{d}} \left[-e^{-2\bar{k}_1 \overline{d}} + 4 \int_0^\infty \frac{\overline{\rho} e^{-2\sqrt{\overline{\rho}^2 + (\bar{k}_1 \overline{d})^2}} d\overline{\rho}}{\varepsilon_{2/1} \sqrt{\overline{\rho}^2 + k_{2/1}^2 (\bar{k}_1 \overline{d})^2} + \sqrt{\overline{\rho}^2 + (\bar{k}_1 \overline{d})^2}} \right] + \frac{n\overline{\sigma} e^{-\bar{k}_1 \overline{d}}}{\bar{k}_1 \left(1 + \varepsilon_{2/1} k_{2/1}\right)}. \tag{3.36}$$

The first term in Eq. (3.34) and the terms in the brackets of Eqs. (3.35)–(3.36) correspond to normalized electrostatic free energies due to the interaction between the charged particle and an uncharged substrate. In particular, they have a common term $-n^2 e^{-2\bar{k}_1 \overline{d}}/2\overline{d}$ due to the image charge, and the integrals in Eqs. (3.35)–(3.36) take into consideration the electronic response of dielectric and semiconductor, respectively. The last terms in Eqs. (3.34)–(3.36) are normalized electrostatic free energies due to the surface charge of the substrate. They are all proportional to the normalized surface charge density $\overline{\sigma}$ and decays exponentially with the separation between the charge and the substrate.

3.5 Van der Waals free energy

To obtain the van der Waals free energy between the particle and the substrate, we make use of the 6-12 LJ between two atoms [38]

$$u = -\frac{A}{r^6} + \frac{B}{r^{12}}, \tag{3.37}$$

where r is the distance between the two atoms, and A, B are constants. Eq. (3.37) can also be written in the form [42]

$$u = 4c\left[\left(\frac{r_o}{r}\right)^{12} - \left(\frac{r_o}{r}\right)^{6}\right], \tag{3.38}$$

where c is the depth of the potential well and r_o is the distance at which the potential $u = 0$. The depth c is related to the constants A and B by the equations $4cr_o^{12} = B$, and $4cr_o^6 = A$.

Assuming the particle contains N atoms and the atom number density in the substrate is ρ_1, the van der Waals free energy G_{vdw} between the particle and a substrate of thickness L can now be obtained by integrating Eq. (3.38), i.e.,

$$G_{vdw} = 8\pi N c\rho_1\left[\frac{r_o^{12}}{90}\left(\frac{1}{d^9} - \frac{1}{(d+L)^9}\right) - \frac{r_o^6}{12}\left(\frac{1}{d^3} - \frac{1}{(d+L)^3}\right)\right]. \tag{3.39}$$

Therefore, the normalized van der Waals energy $g_{vdw} = G_{vdw}/k_BT$ is given by

$$g_{vdw} = N_{vdw}\left[\frac{\bar{r}_o^{12}}{90}\left(\frac{1}{\overline{d}^9} - \frac{1}{(\overline{d}+\overline{L})^9}\right) - \frac{\bar{r}_o^6}{12}\left(\frac{1}{\overline{d}^3} - \frac{1}{(\overline{d}+\overline{L})^3}\right)\right], \tag{3.40}$$

where

$$N_{vdw} = \frac{8\pi N c\rho_1 l_B^3}{k_BT}, \quad \bar{r}_o = r_o/l_B. \tag{3.41}$$

In the case of a half space, i.e. $L \to \infty$, Eq. (3.40) reduces to

$$g_{vdw} = N_{vdw}\left[\frac{\bar{r}_o^{12}}{90\overline{d}^9} - \frac{\bar{r}_o^6}{12\overline{d}^3}\right]. \tag{3.42}$$

3.6 Equilibrium separation between the particle and the substrate

In this section, we determine the equilibrium separation between the particle and the substrate by calculating the corresponding total free energy given by the sum of

electrostatic and van der Waals free energies. In the normalized form,

$$g = g_{el} + g_{vdw}, \tag{3.43}$$

where g_{el} and g_{vdw} are given by Eqs. (3.34) – (3.36) and Eqs. (3.40) – (3.42), depending on the type and geometry of the substrate.

Clearly, g is a function of the normalized separation $\overline{d}$ and the dimensionless parameters $\bar{k}_1$, $\overline{\sigma}$, N_{vdw}, $\bar{r}_o$, $\overline{L}$ (in the case of the dielectric substrate only), $\varepsilon_{2/1}$ (in the case of the dielectric or semiconducting substrate) and $k_{2/1}$ (in the case of the semiconducting substrate only). In the following, we consider an electrolyte solution of low ionic strength, with Debye length of 100 nm and dielectric constant of 80. Then, at room temperature $T = 300K$, $\bar{k}_1 \approx 7 \times 10^{-3}$. The length scale r_o in the LJ potential is usually on the order of angstrom (Å). In the calculations which follow, we have taken $\bar{r}_o = 0.1429$ and $n = N = 1$. To get an order of magnitude estimate for the normalized van der Waals parameter N_{vdw}, we note that the number density ρ_1 is on the order of $1\ \mathring{A}^{-3}$, and the energy well depth c is of the order of 10^{-22}–10^{-20}. Therefore, the range of N_{vdw} is approximately from 2.1×10^2 to 2.1×10^4 for $N = 1$.

3.6.1 Metallic substrate

Figure 3.5 plots the normalized total energy $g(\overline{d})$ of a point charge Q above a metallic half space with initial surface charge density σ. In Figure 3.5 (a) the point charge and the surface charge are of the same sign, while in Figure 3.5 (b) the signs are opposite. In each plot, the different curves correspond to different surface charge density, characterized by different values of $\overline{\sigma}$. It can be seen that for each curve, there is an equilibrium state corresponding to the local energy minimum at short range ($\overline{d} < 1$). Also far from the substrate ($\overline{d} \geq 10^3$), $dg/d(\overline{d}) = 0$ and the interaction between the particle and the substrate is negligible. We identify the former state as the "attached" state and the latter state as the "detached" state.

It is interesting to see that for all situations, the location of the attached state is similar (with $\overline{d} \approx 0.1167$), that is, it does not vary much with the sign or the magnitude of the surface charge. Indeed, if one evaluates the van der Waals en-

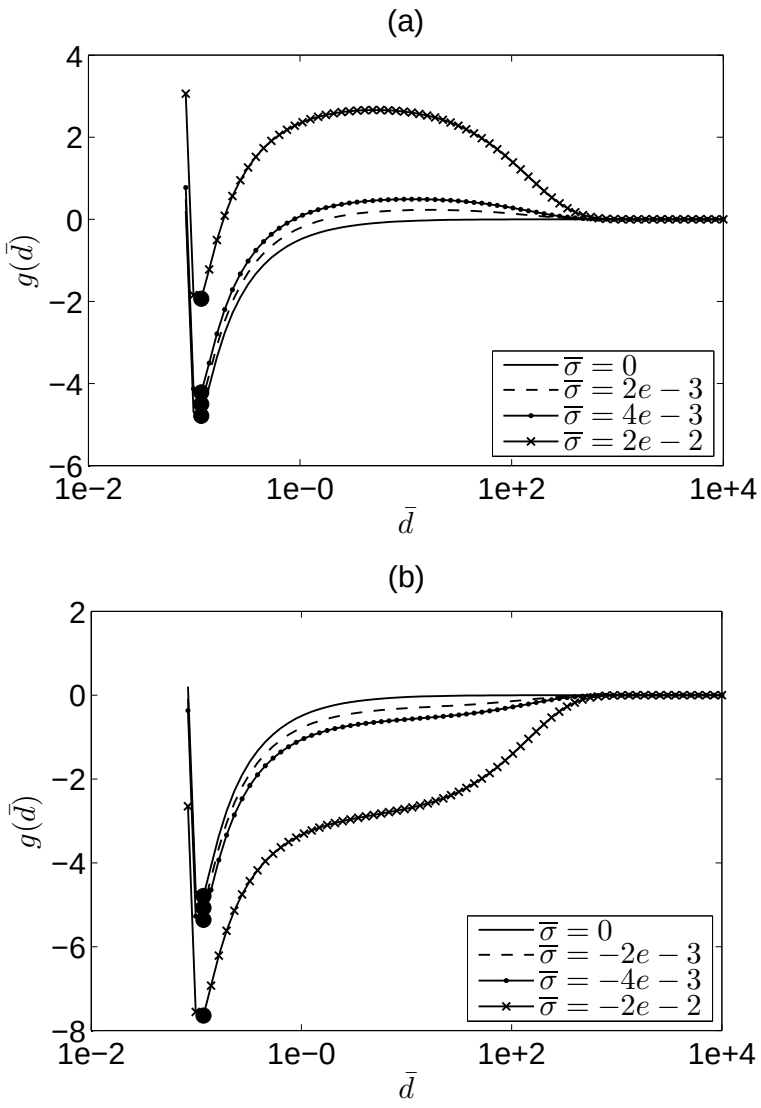

Figure 3.5: Normalized total energy $g(\bar{d})$ of a charged particle Q above a metallic half space with initial surface charge density σ, (a) $\bar{\sigma} > 0$, (b) $\bar{\sigma} < 0$. For all cases $n = N = 1, \bar{k}_1 = 7 \times 10^{-3}, N_{vdw} = 2.1 \times 10^3$, and $\bar{r}_o = 0.1429$. Different curves in each plot correspond to different normalized charge density $\overline{\sigma}$.

ergy minimum from Eq. (3.42), it is found to be ~ 0.1226. That is, in all cases, the location of the attached state is very close to the van der Waals minimum, i.e., the primary minimum in the classical DLVO theory. The energy pathway from the detached state to the attached state, however, is very sensitive to the sign and magnitude of the surface charge. In particular, without the surface charge, the interaction of the charge with the substrate is mainly attractive except when it is very close to the substrate and the van der Waals interaction becomes repulsive. This is expected since the point charge and its image charge induced by the metallic substrate attract each other. As the surface charge density of the same sign increases, i.e. as $\overline{\sigma}$ increases in Figure 3.5 (a), the energy barrier between the attached state and the detached state is raised, and the particle is more likely to stay at the detached state. If the surface charge density of opposite sign increases, i.e. as $|\overline{\sigma}|$ increases in Figure 3.5 (b), the energy corresponding to the attached state is greatly lowered, and attachment is much more favored.

3.6.2 Dielectric substrate

Figure 3.6 plots the normalized total energy $g(\overline{d})$ of a charged particle Q above a dielectric substrate with surface charge density σ . For these plots, we have taken $\overline{L} = 1.43 \times 10^4$, i.e. $L = 10\mu m$. Also, the dielectric constant $\varepsilon_2 = 10$ is used so that $\varepsilon_{2/1} = 0.125$. In the absence of the surface charge, the interaction between the particle and the substrate appears to be repulsive, and there is no local minimum at short range. That is, the particle stays at the detached state. Increasing the surface charge of the same sign strongly increases the repulsive force, as can be seen from Figure 3.6 (a).

The effect of introducing a surface charge of opposite sign on a dielectric substrate is quite different from the case of a metallic substrate. As shown in Figure 3.6 (b), increasing the surface charge not only lowers the total energy, but also changes the location of the attached state (marked by the dark circles). This change is sensitive to the magnitude of the surface charge. In particular, as $|\overline{\sigma}|$ varies from $2e-3$ to $2e-2$, the location of the energy minimum decreases by three folds (from approximately 14 to 5). Overall, the location of the attached state is at a much

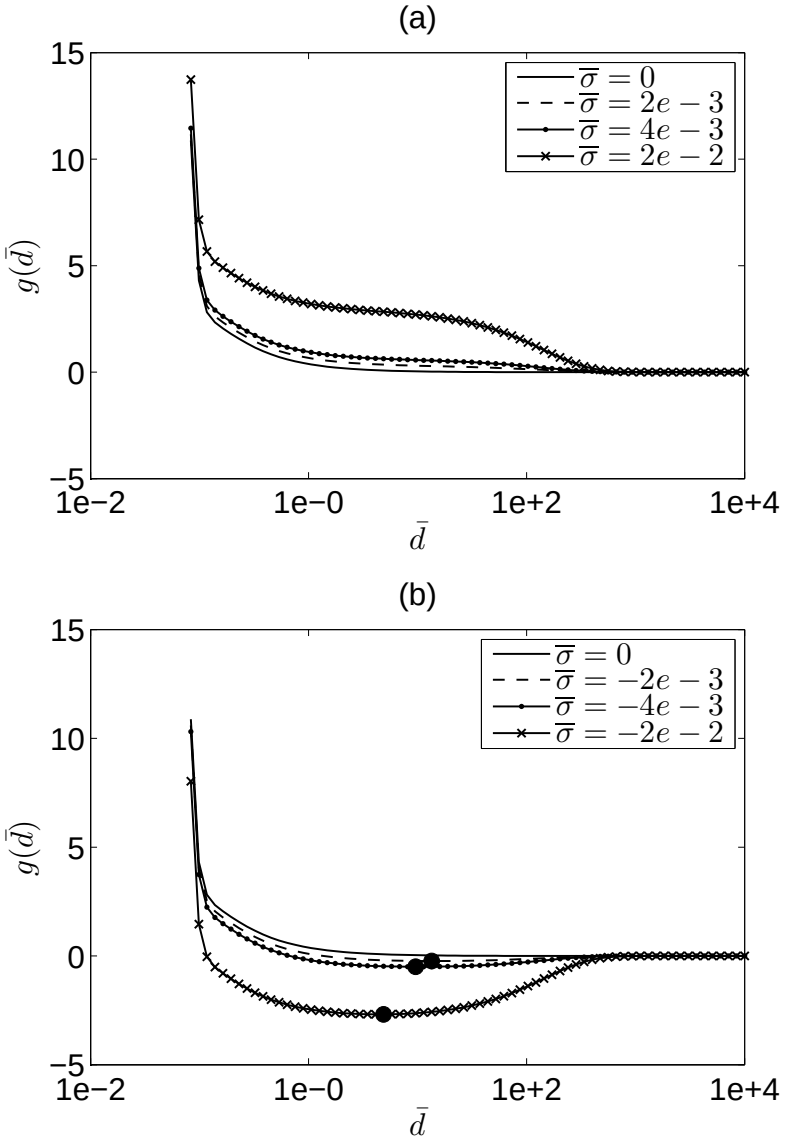

Figure 3.6: Normalized total energy $g(\bar{d})$ of a charged particle Q above a dielectric substrate with the surface charge density σ, (a) $\bar{\sigma} > 0$, (b) $\bar{\sigma} < 0$. For all cases, $n = N = 1, \bar{k}_1 = 7 \times 10^{-3}, \bar{L} = 1.43 \times 10^4, \varepsilon_{2/1} = 0.125, N_{vdw} = 2.1 \times 10^3$, and $\bar{r}_o = 0.1429$.

larger distance ($>> 1$) from the substrate than in the case of a metallic substrate (~ 0.1). This is certainly different from the classical DLVO theory where a primary minimum is always present near the van der Waals minimum.

3.6.3 Semiconducting substrate

Figures 3.7 and 3.8 show the normalized total energy $g(\overline{d})$ of a charged particle Q above a semiconducting half space with the surface charge density σ. $\overline{\sigma} > 0$ in Figure 3.7 and $\overline{\sigma} < 0$ in Figure 3.8. In each figure, we show the dependence of the normalized total energy on the normalized separation for two different Debye length ratios and four different surface charge densities. By varying the Debye length ratio k_2/k_1, the semiconducting substrate can behave in the same way as either a dielectric or a metallic substrate. Clearly, when the Debye length of the semiconductor k_2 is comparable to that of the electrolyte, as shown in Figures 3.7 (a) and 3.8 (a), $g(\overline{d})$ resembles the behavior of a dielectric substrate in Figure 3.6. When $k_2 >> k_1$, modifying the surface charge only changes the energy depth, and has little effect on the location of the attached state. This is similar to the case of a metallic substrate. The change in energy depth, however, is much smaller than what is shown in Figure 3.5. This is because the contribution of the surface charge to the electrostatic free energy, the last term in Eq. (3.36), is very small for large k_2/k_1.

3.7 Conclusions and discussion

The electrostatic free energy between a charged particle in an electrolyte solution and a metallic, dielectric, or semiconducting substrate is obtained by solving exactly the electric potential based on the DH theory of electrolyte. The van der Waals free energy is calculated based on the LJ potential between two atoms and is added to the electrostatic energy to determine the equilibrium separation between the particle and the substrate. At low ionic strength, our results show that the location of the attached state and the energy pathway from the detached to the attached state are quite different for different types of substrate. In particular, for a solution of Debye length equal to 100 nm, the location of the attached state for a metallic substrate

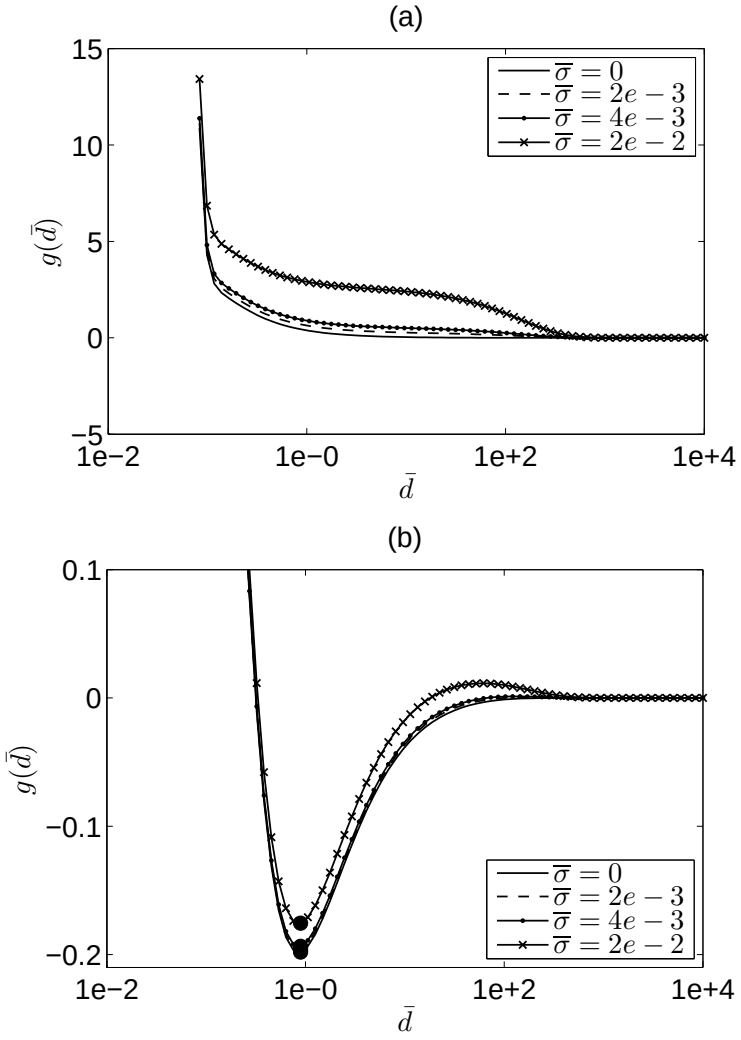

Figure 3.7: Normalized total energy $g(\bar{d})$ of a charged particle Q above a semiconductor half space with surface charge density σ and $\bar{\sigma} > 0$: (a) $k_{2/1} = 1$ and (b) $k_{2/1} = 1000$. For all cases $n = N = 1, \bar{k}_1 = 7 \times 10^{-3}, \varepsilon_{2/1} = 0.125, N_{vdw} = 2.1 \times 10^3$, and $\bar{r}_o = 0.1429$.

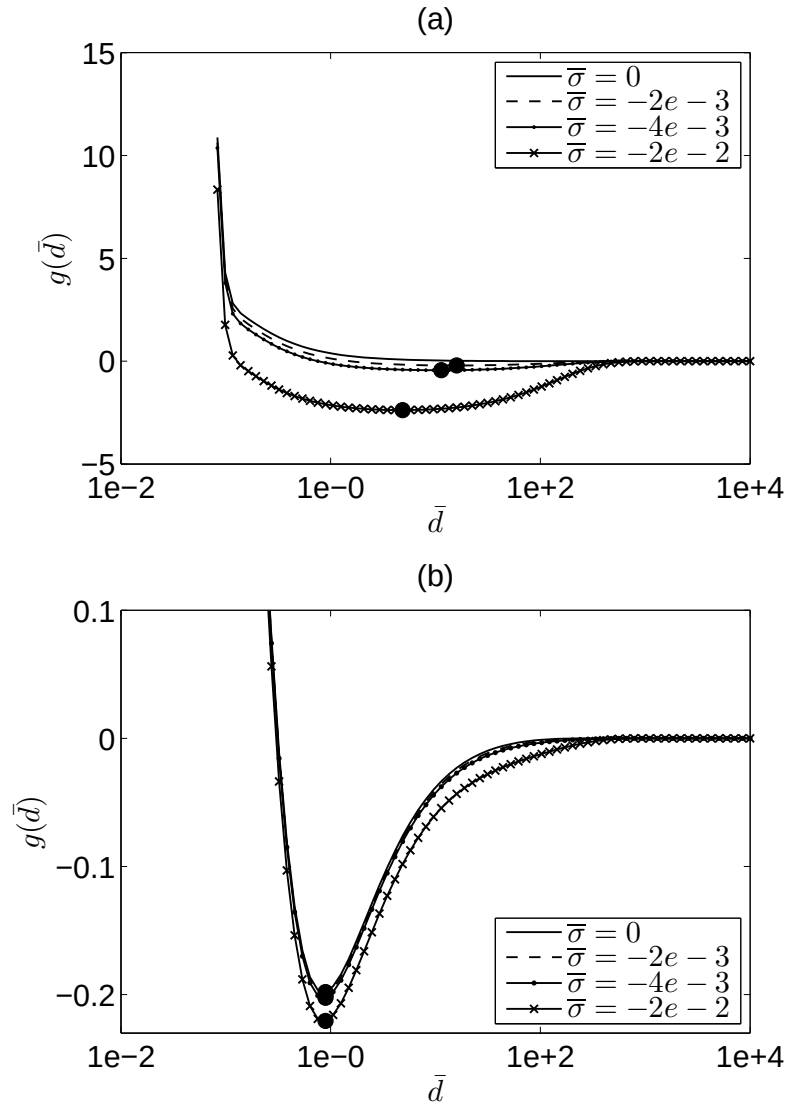

Figure 3.8: Normalized total energy $g(\bar{d})$ of a charged particle Q above a semiconductor half space with surface charge density σ and $\bar{\sigma} < 0$: (a) $k_{2/1} = 1$ and (b) $k_{2/1} = 1000$. For all cases $n = N = 1, \bar{k}_1 = 7 \times 10^{-3}, \varepsilon_{2/1} = 0.125, N_{vdw} = 2.1 \times 10^3$, and $\bar{r}_o = 0.1429$.

is always close to the van der Waals minimum, and does not vary much with the sign or the magnitude of the surface charge density. Increasing the surface charge (of opposite sign to that of the particle), however, significantly lowers the energy and facilitates the transition from the detached to the attached state. For a dielectric substrate, the attached state is located at a distance of around two orders of magnitude larger than in the case of a metallic substrate, and this equilibrium separation reduces as the opposite surface charge increases. The behavior of a semiconducting substrate can resemble that of a dielectric or a metal, depending on its Debye length relative to the Debye length of the electrolyte solution.

As mentioned before, the total free energy g is a function of the following dimensionless parameters: $g = g(\overline{d}, \bar{k}_1, \overline{\sigma}, N_{vdw}, \bar{r}_o, \overline{L}, \varepsilon_{2/1}, k_{2/1})$. For fixed $\overline{L}, \varepsilon_{2/1}$ and $k_{2/1}$, the normalized Debye length $\bar{k}_1$ measures the strength of the electrostatic interaction, including the contribution from the response of the substrate to the charge and that from the surface charge. $\overline{\sigma}$ captures the effect of the surface charge alone. N_{vdw} and $\bar{r}_o$ govern the effect of the van der Waals interaction. It is the competition of these three effects that contribute to the interesting phenomenon seen in Section 3.6. The results presented in Section 3.6 are produced using a Debye length of 100 nm, which corresponds to low ionic strength, strong electrostatic interactions and comparable contributions from the three effects. Clearly, larger N_{vdw} and $\bar{r}_o$ correspond to higher strength and longer range of the van der Waals interaction. If the van der Waals interaction is much larger than the electrostatic interaction, the effect of different substrate vanishes. More interesting is the competition between electrostatics due to the surface charge and the response of the substrate. In particular, with the same values for $\overline{\sigma}$, N_{vdw} and $\bar{r}_o$ as in Section 3.6, if the Debye length is reduced to 0.01 nm, the behaviors of the metallic substrate and the dielectric substrate are almost the same. This is because the electrostatic interaction is highly screened due to such a small Debye length. With Debye length equal to 0.1 nm, we can still see a significant difference between metallic and dielectric substrates. However, in this case, the contribution from $\bar{\sigma}$ is small enough so that the electrostatic interaction is governed by the response from the substrate, and therefore the energy curves for these different $\bar{\sigma}$'s converges to one for metal (with

one energy minimum) and one for dielectric (with no local energy minimum and completely repulsive interaction). As $\bar{\sigma}$ is increased, the same qualitative behavior as in Section 3.6 is again observed. Increasing $\bar{\sigma}$ by over three orders of magnitude diminishes the difference between substrates because for sufficiently large $\bar{\sigma}$, the last term in Eqs. (3.34)– (3.36) dominates the electrostatic free energy, which varies with $\overline{d}$ in the same way for all substrates. In summary, by varying $\bar{k}_1$ and $\bar{\sigma}$, different equilibrium separation and energy well depth for different substrates can be obtained. Since these two quantities are measures of the adhesion of the particle to the substrate, our results provide suggestions as to how to modulate the adhesion by changing the ionic strength of the solution, the electronic nature of the substrate and its surface charge density.

In the classical DLVO theory, it is possible to see a secondary minimum far away. In our calculations, we do not see a secondary minimum except for very weak electrostatic interaction and strong van der Waals interaction. For example, with Debye length of 1 nm, $\overline{\sigma} = 2 \times 10^2$, $N_{vdw} = 3.4 \times 10^3$ and $\bar{r}_o \simeq 0.7$, for both metallic and dielectric substrates, there is one energy minimum located at $\overline{d} \simeq 0.6$ and a second one located at $\overline{d} \simeq 18$. The second minimum corresponds to a very shallow energy well, i.e. around two orders of magnitude smaller than that of the first minimum. In addition, in this case, because of the small Debye length and large $\bar{\sigma}$, again the energy profiles for metallic and dielectric substrates approach each other.

The results presented here are based on the linearized PB equation, and are valid therefore only for electric potentials satisfying Eq. (3.2). Investigation of the cases where the electric potential does not satisfy Eq. (3.2) necessitates the solution of the nonlinear PB equation, which precludes analytical, closed-form solutions instead requiring numerical computations.

Finally, we mention that the retardation effect of van der Waals interaction is not considered in this work. Retardation may become important when the separation between the particle and the substrate exceeds a few nanometers [43] or the size of the particle is beyond the order of $1\mu m$ [44]. Under those situations, the current method of using the LJ potential may overestimate the van der Waals interaction.

Two approaches can be taken to include the retardation effect. The first is to use Lifshitz theory and consider the complete dielectric spectra of the materials. The second is to introduce a correction factor in the Hamaker constant which includes a characteristic wave length of the dispersion interaction [44]. For both approaches, closed-form expression for the van der Waals interaction is only possible for very simple geometries. Since the focus of this work is on how the electronic response of the substrate affects its interaction with the charged particle, we have neglected this effect and simply modeled the particle as a point. In addition, we expect the behaviors seen in this work to be present even if retardation is included. This is because retardation will weaken the van der Waals interaction, and therefore the difference between substrates due to electrostatic interaction will become more pronounced.

Bibliography

[1] M.J. Tarlov, A.B. Steel, in: J.F. Rusling (Ed.), Biomolecular Films: Design, Function, and Applications, in: Surfactant Science Series, vol. 111, Dekker, New York, 2003.

[2] C. Carrasco, A. Joubert, C. Tardy, N. Maestre, M. Cacho, M.F. Brana, C. Bailly, Biochemistry 42 (2003) 11751.

[3] E. Komarova, M. Aldissi, A. Bogomolova, Biosensors and Bioelectronics 21 (2005) 182.

[4] C.S. Riccardi, K. Dahmouche, C.V. Santilli, P.I. da Costa, H. Yamanaka, Talanta 70 (2006) 637.

[5] X.H. Lin, H.Y. Wan, Y.F. Zhang, J.H. Chen, Talanta 74 (2008) 944.

[6] F. Patolsky, G. Zheng, O. Hayden, M. Lakadamyali, X. Zhuang, C.M. Lieber, PNAS 101 (2004) 14017.

[7] J. Hahm, C.M. Lieber, Nano Lett. 4 (2004) 51.

[8] M. Zheng, A. Jagota, E.D. Semke, B.A. Diner, R.S. Mclean, S.R. Lustig, R.E. Richardson, N.G. Tassi, Nat. Mater. 2 (2003) 338.

[9] M. Zheng, A. Jagota, M.S. Strano, A.P. Santos, P. Barone, S.G. Chou, B.A. Diner, M.S. Dresselhaus, R.S. Mclean, G.B. Onoa, G.G. Samsonidze, E.D. Semke, M. Usrey, D.J. Walls, Science 302 (2003) 1545.

[10] G.B. Schneider, A.English, M.Abraham, R.Zaharias, C. Stanford, J. Keller, Biomaterials 25 (2004) 3023.

[11] K. Anselme, Biomaterials 21 (2000) 667.

[12] G. Schneider, K. Burridge, Exp. Cell Res. 214 (1994) 264.

[13] Y. Hong and D.G. Brown, Langmuir 24 (2008) 5003.

[14] S. Manohar, A.R. Mantz, C.-Y. Hui, A. Jagota, D.V. Vezenov, Submitted to ACS Nano (2008).

[15] T. Schlick, Molecular Modeling and Simulation, Springer-Verlag, New York, 2002.

[16] M. Le Bret, B.H. Zimm, Biopolymers 23 (1984) 271.

[17] P. Mills, C.F. Anderson, M.T. Record, J. Phys. Chem. 89 (1985) 3984.

[18] B. Jayaram, D.L. Beveridge, J. Phys. Chem. 95 (1991) 2506.

[19] A.P. Lyubartsev, L. Nordenskiöld, J. Phys. Chem. 101 (1997) 4335.

[20] H. Gao and Y. Kong, Annu. Rev. Mater. Res. 34 (2004) 123.

[21] S. Manohar, T. Tang and A. Jagota, J. Phys. Chem. C. 111 (2007) 17835.

[22] R.R. Johnson, A.T.C. Johnson, M.L. Klein, Nano Lett. 8 (2008) 69.

[23] C.J. Cramer and D.G. Truhlar, Chem. Rev. 99 (1999) 2161.

[24] W.B. Russel, D.A. Saville, W.R. Schowalter, Colloidal Dispersions, Cambridge Univ. Press, Cambridge, 1989.

[25] F. Fogolari, A. Brigo and H. Molinari, J. Mol. Recognit. 15 (2002) 377.

[26] G.S. Manning, J. Chem. Phys. 51 (1969) 924.

[27] G.S. Manning, Quart. Rev. Biophys. 11 (1978) 179.

[28] G.S. Manning, Physica A 231 (1996) 236.

[29] G.V. Ramanathan, J. Chem. Phys. 88 (1988) 3887.

[30] J. Naghizadeh, Cell Biophysics 11 (1987) 103.

[31] U. Mohanty, B.W. Ninham and I. Oppenheim, Proc. Natl. Acad. Sci. USA 93 (1996) 4342.

[32] B. O'Shaughnessy and Q. Yang, Phys. Rev. Lett. 94 (2005) 048302.

[33] G.S. Manning, J. Phys. Chem. B 111 (2007) 8554.

[34] T.Tang, A.Jagota, C.Y.Hui, J. Colloid interface Sci. 299 (2006) 564.

[35] T.Tang, C.Y.Hui, A.Jagota, J. Colloid interface Sci. 299 (2006) 572.

[36] J.N. Israelachvili, Intermolelucar and Surface Forces, second ed., Academic Press, London, 1992.

[37] M. Hermansson, Colloids and Surfaces B: Biointerfaces 14 (1999) 105.

[38] L.A. Girifalco, Statistical mechanics of solids, Oxford Univ. Press, Oxford, New York, 2000.

[39] I.N. Sneddon, The Use of Integral Transforms, MCGraw-Hill, New York, 1972.

[40] J.D.Jackson, Classical Electrodynamics, third ed., Wiley, New York, 1999.

[41] A. Erdelyi (Ed.), Tables of Integral Transforms, Bateman Manuscript Project, vol. II, MCGraw-Hill, New York, 1954.

[42] L. A. Girifalco, M. Hodak, and R. S. Lee, Phys. Rev. B, 62, 19 (2000) 13104.

[43] J. Gregory, Particles in Water: Properties and Processes, CRC Press, 2006.

[44] J. Gregory, J. Colloid Interface Sci., 83 (1981) 138.

Chapter 4
Counterion Condensation on a Polyelectrolyte near an Electronically Responsive Cylinder[1]

4.1 Introduction

The electrostatic interaction between a polyelectrolyte (PE) and a substrate has attracted a lot of attention in theoretical modeling as well as in practical applications, especially in nano- and biotechnology. For example, nanosensors based on nanowires have enabled the detection of viruses [1] or mutant DNA sequences [2] through the measurement of conductance changes in the nanowires; carbon nanotubes (CNTs) have been used to deliver drugs into specific areas [3]; immobilization and hybridization of DNA on the surface of biosensors [4], where the probe DNA molecules perform the role of detection elements, provide ways of finding viruses [5] and diseases [6, 7]. It has also been discovered that a single-stranded DNA (ssDNA) can form a helical wrapping on the surface of CNTs [8, 9] and effectively disperse and separate them according to their electronic properties. In addition, it has been found that DNA as well as small proteins [10] can be encapsulated inside a CNT [11, 12], which shows the potential of using CNT in gene therapy.

One of the models widely used to characterize the behaviors of PEs in a solution is Manning's theory of counterion condensation (CC) [13]. In the theory of CC, by considering the minimization of free energy of the PE in a dilute solution, it is predicted that if the charge density of the polymer exceeds a certain value, CC occurs in the vicinity of the PE, effectively reducing its charge density [13, 14]. Experimental evidence [15–18] and supporting computer simulations [19] exist behind

[1] Reprinted with permission from : "Counterion Condensation on a Polyelectrolyte near an Electronically Responsive Cylinder", Oxana Malysheva, Tian Tang and Peter Schiavone, J. Phys. Chem. C, 2010, 114 (9), pp 3781-3790. Copyright 2010 American Chemical Society.

the theory of CC. In particular, Gregor and Frederick [17] studied the pH titration curves for polyacrilic acid when different types of counterions were present. Their experimental data showed interesting dependence of the pH titration curves on a dimensionless polymer charge density ξ. Specifically, when ξ was lower than a critical value ξ_{crit}, these curves did not vary with different types of counterions. When $\xi > \xi_{crit}$, however, different pH titration curves were observed for different counterion types. This can be explained to be a result of condensed counterions on the polymer [15]. The paper by Young *et al.* provided visual support of CC from Monte Carlo simulations: the snapshot depicts condensed and uncondensed counterions [19]. In the recent report by Keyser *et al.*, the authors succeeded in the direct measurement of electric force on DNA in nanopore [18]. Using the obtained values for the force acting on the molecule, the effective charge on DNA was deduced for various salt concentrations. Here, the effective charge is the difference between the original bare charge and the charge of the condensed counterions [14]. The results validated the numerical accuracy of the effective charge of the DNA as predicted by Manning [14]. In addition, they confirmed the invariance of the effective charge to a wide variation of salt concentrations. Supported by laboratory observations, the theory of CC is also a mathematically convenient approach to characterize a PE system, since analytical expressions can often be obtained for the electric potential, using the linear Debye–Hückel (DH) equation with a reduced charge density, instead of the non-linear Poisson–Boltzmann formulation [20–23].

In a recent paper by Manning [24], CC on different charged geometrical shapes is examined. Existence and degree of CC are studied for small and large charged spheres, on charged walls, as well as on thin and thick charged cylinders. The terminologies "small "or "thin "here mean that the radius a of the sphere or cylinder is small compared to the Debye screening length [21–24] k^{-1}, that is, $ka \ll 1$. Meanwhile, the reference to "large"or "thick "means that a is comparable with k^{-1}, that is, $ka = O(1)$. It is found that in a solution with low but nonzero salt concentration, CC occurs on all geometrical shapes described above when the surface charge density of these geometries is beyond a critical value σ_{crit}. In the limit of zero salt concentration, however, Zimm–Le Bret [25] behavior is captured. In this

case, no CC exists on a charged sphere whereas all counterions are condensed on a charged plane, regardless of their surface charge densities. For a charged cylinder, CC exists to keep the surface charge density of the cylinder at or below σ_{crit}. In all cases, the charged entity is in a solution alone, and is not interacting with anything other than the electrolyte solution.

In this work, we explore the phenomenon of CC on a PE when it interacts with an electronically responsive cylinder. A nearby substrate can have a strong effect on the electric field of a charged entity in a solution and, therefore, on its overall behavior. One such example is the different degree of CC on a line of charges when it is above a metallic, dielectric, or semiconducting half space [26, 27]. Another example is the strong dependence of the equilibrium separation between a charged particle and a substrate on the electronic nature of the latter [28]. We are particularly interested in a PE near a cylinder because many novel nano-materials possess such a geometry, for example, nanowires, nanosensors, or CNTs. Through this work, we demonstrate how the CC on the PE can change when it is brought from the bulk solution to the neighborhood of an electronically responsive cylinder.

This paper is organized as follows. In Section 4.2, we describe the physical problem and the mathematical approach. In Sections 4.3 and 4.4, we separately study the cases of a PE near a metallic cylinder and near a dielectric cylinder. The degree of CC is obtained for each system by solving the boundary value problems for the electric potential and evaluating the free energy. Distinction between the two cases is demonstrated. Finally, discussion and conclusion are given in Section 4.5.

4.2 Problem description

The system under consideration consists of a PE and an electronically responsive cylinder, both embedded in a dilute electrolyte solution. The PE is modeled as a thin cylinder of radius a and the electronically responsive cylinder is of much larger radius r_0, that is, $a \ll r_0$. The axes of the PE and the cylinder are parallel and the distance between their centers is denoted by d. Both the PE and the cylinder

are assumed to be very long along their axes, so that the problem is essentially two-dimensional, as shown in Figure 4.1. The exterior region to the PE–cylinder system, denoted by D_0, is occupied by an electrolyte solution with a dielectric constant ε_1. The interior of the electronically responsive cylinder, D_1, can either be a metal or dielectric with dielectric constant ε_2; the interior of the PE, D_2, is assumed to be a vacuum. Two sets of coordinates are used for the convenience of the calculations, as shown in Figure 4.1. (r, ψ) are polar coordinates with the origin located at the center of the cylinder, whereas (r', ψ') are polar coordinates with the origin located at the center of the PE. These two sets of coordinates can be easily converted using the following relations

$$r(r', \psi') = \sqrt{(r')^2 + d^2 - 2dr' \cos \psi'}, \quad \psi(r', \psi') = \arctan \frac{r' \sin \psi'}{d - r' \cos \psi'}. \quad (4.1)$$

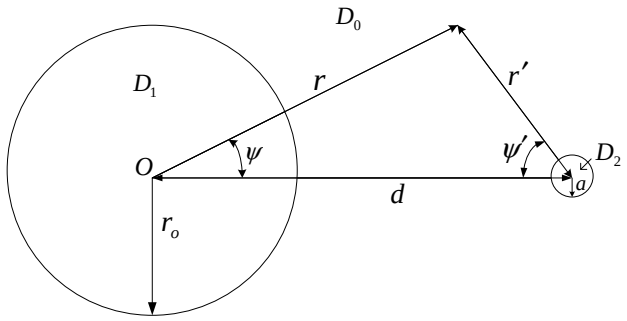

Figure 4.1: Geometry of the the metallic or the dielectric cylinder (left) and the PE (right). d is the distance between their centers, r_0 and a are the radii of the cylinder and the PE, respectively. (r, ψ) and (r', ψ') are polar coordinates with the origins at the centers of the cylinder and the PE, respectively. D_0 is the exterior region to the PE–cylinder system, D_1 is the interior region of the cylinder, and D_2 is the interior region of the PE.

We denote by σ the bare surface charge density of the PE before CC occurs and by θ the number of condensed counterions per bare unit surface charge on the PE. The total number of condensed counterions per unit length of the PE is $N\theta$, if Nq is the total bare charge per unit length, where q is the elementary charge. θ can be obtained from the equilibrium between two contributions to the free energy of the system. The first contribution is the electrostatic interaction between the PE

and the counterions, which tends to attract the counterions from the bulk solution to the vicinity of the PE. The other is the entropic effect, which tends to keep the counterions in a more random state, namely, in the bulk. The competition between these two contributions determines the amount of CC on the PE.

4.3 Polyelectrolyte near a metallic cylinder

In this section, we consider the cylinder, that is, domain D_1 in Figure 4.1, to be metallic. At equilibrium, the electric potential inside a metal must be constant. In particular, we assume that the metallic cylinder is grounded so that the electric potential inside is zero:

$$\phi_{in(l)}^{met} = 0 \text{ in } D_1. \tag{4.2}$$

Here the superscript "met" indicates the case of a PE near a metallic cylinder, the subscript "in(l)" is used to indicate the electric potential inside the large cylinder, as opposed to the electric potential inside the small cylinder representing the PE. The governing equation for the electric potential ϕ_{out}^{met} in the solution, that is, domain D_0, is given by the DH equation [23]

$$\nabla^2 \phi_{out}^{met} = k^2 \phi_{out}^{met} \text{ in } D_0, \tag{4.3}$$

where the subscript "out" is used to indicate the electric potential outside the two cylinders and k is the reciprocal of the Debye length [23]. Since we model the inside of the PE as a vacuum without any charges, the governing equation for the electric potential $\phi_{in(s)}^{met}$ in domain D_2 is

$$\nabla^2 \phi_{in(s)}^{met} = 0 \text{ in } D_2. \tag{4.4}$$

Each of the three functions ϕ_{out}^{met}, $\phi_{in(l)}^{met}$, $\phi_{in(s)}^{met}$ can be expressed in different sets of variables (r, ψ) or (r', ψ') shown in Figure 4.1. Boundary conditions for the electric potential may be more conveniently described in one coordinate system than the other, depending on the boundary. Without loss of generality, we use a single notation for the same function under different coordinate systems. The boundary conditions (BCs) are then given by

$$\lim_{r \to \infty} \phi_{out}^{met} = 0, \tag{4.5a}$$

$$\phi_{out}^{met}\Big|_{r=r_0} = 0, \tag{4.5b}$$

$$\phi_{out}^{met}\Big|_{r'=a} = \phi_{in(s)}^{met}\Big|_{r'=a}, \tag{4.5c}$$

$$\varepsilon_1 \frac{\partial \phi_{out}^{met}}{\partial r'}\Big|_{r'=a} - \frac{\partial \phi_{in(s)}^{met}}{\partial r'}\Big|_{r'=a} = -\frac{\sigma}{\varepsilon_0}. \tag{4.5d}$$

Equation (4.5a) states that the electric potential vanishes at infinity. Equations (4.5b) and (4.5c) are because the tangential component of the electric field has to be continuous across the interfaces. Equation (4.5d) is due to the condition that the normal component of the electric displacement is discontinuous on the PE–solution interface, and the difference is the surface charge density of the PE. Here ε_0 is the permittivity of the vacuum and ε_1 is the dielectric constant of the solution [29]. Equations (4.2)–(4.5d) constitute the boundary value problem (BVP) for the electric potential in the entire domain.

Due to the presence of the metallic cylinder the electric potential on the surface of the PE is not uniform, which makes exact analytical solution to the above BVP difficult if not impossible to obtain. In fact, we have tried to obtain the exact solution for the electric potential in all three domains in terms of series. However, application of the BCs results in a linear system of infinite dimension for the coefficients in the series, which is not solvable without making additional assumptions. It should be noted that here we are considering the situation where the radius of the PE is much smaller than that of the metallic cylinder, namely, $a \ll r_0$. Indeed, a PE is often modeled as a line of charges with its size essentially approaching zero. Using the line of charges model will require solving a three-dimensional problem, which is analytically more difficult. Hence, we adopt another popular model of a PE and smear out the charges onto the surface of a cylinder, but with a size much smaller compared to the other dimensions in the system. Under this condition, the non-uniformity of the electric potential on the surface of the PE is expected to be small. Therefore, we can modify the BCs on $r' = a$ by assuming that the electric potential on $r' = a$ is uniform. This assumption, together with Eq. (4.4), implies that the potential inside and on the surface of the PE is a constant. We take this constant to be the potential in the solution ϕ_{out}^{met} evaluated at a particular point, namely,

$(r' = a, \psi' = 0)$ or $(\psi = 0, r = d - a)$. That is

$$\phi_{in(s)}^{met} = \phi_{out}^{met}\big|_{r'=a}^{\psi'=0}. \tag{4.6}$$

With this approximation, the two BCs (4.5c) and (4.5d) are satisfied only at the point of $(r' = a, \psi' = 0)$. That is, the BCs modified from (4.5c) and (4.5d) are

$$\phi_{out}^{met}\big|_{r'=a}^{\psi'=0} = \phi_{in(s)}^{met}\big|_{r'=a}^{\psi'=0} = \phi_{in(s)}^{met}, \tag{4.7a}$$

$$\varepsilon_1 \frac{\partial \phi_{out}^{met}}{\partial r'}\bigg|_{r'=a}^{\psi'=0} = -\frac{\sigma}{\varepsilon_0}, \tag{4.7b}$$

Numerical calculations are performed to check the self-consistency of this approximation. In particular, the maximum percentage error for the approximated BCs is evaluated and the results are provided in Section 4.5.

To solve the above BVP, using the method of separation of variables for Eq. (4.3) and taking into account BC Eq. (4.5a), the electric potential in D_0 can be expressed using the following series

$$\phi_{out}^{met} = \sum_{n=0}^{\infty} a_n^{met} \cos(n\psi) K_n(kr) + C_0^{met} K_0(kr') \text{ in } D_0, \tag{4.8}$$

where $K_n(x)$ is the nth-order modified Bessel functions of the second kind. The unknown coefficients a_n^{met} and C_0^{met} are to be determined using the other BCs. The second term in Eq. (4.8) is the potential of the PE if it was located in an electrolyte solution alone, and the first term appears because of the existence of the metallic cylinder. The approximate solution to $\phi_{in(s)}^{met}$, according to Eq. (4.6), is therefore

$$\phi_{in(s)}^{met} = \sum_{n=0}^{\infty} a_n^{met} K_n\left[k(d-a)\right] + C_0^{met} K_0(ka) \text{ in } D_2. \tag{4.9}$$

So far the only equations that are not satisfied in the approximated BVP [Eqs. (4.3)–(4.5b) and (4.7a), (4.7b)] are Eqs. (4.5b) and (4.7b). These are used to determine the unknown coefficients a_n^{met} and C_0^{met}. Using Eq. (4.5b) and applying the properties of orthogonal functions, [30, 31] a_n^{met} can be found in terms of C_0^{met}

$$a_n^{met} = -C_0^{met} f_n^{met}, \tag{4.10}$$

where the dimensionless functions f_n^{met} are defined as follows

$$f_n^{met} = \begin{cases} \dfrac{\int_0^{2\pi} K_0[ka\Lambda(\psi)]d\psi}{2\pi K_0(kr_0)}, & n = 0 \\ \dfrac{\int_0^{2\pi} K_0[ka\Lambda(\psi)]\cos(n\psi)d\psi}{\pi K_n(kr_0)}, & n \neq 0. \end{cases} \tag{4.11}$$

Here the dimensionless function $\Lambda(\psi) = a^{-1}\sqrt{r_0^2 - 2r_0 d\cos\psi + d^2}$. Lastly, C_0^{met} can be obtained from BC Eq. (4.7b), with the utilization of the transformation between the two sets of coordinates, Eq. (4.1). The result is directly proportional to the surface charge density σ of the PE in the following form

$$C_0^{met} = \frac{\sigma}{k\varepsilon_0\varepsilon_1} \times \frac{1}{K_1(ka) + f_0^{met}K_1(kd-ka) + \frac{1}{2}\sum_{n=1}^{\infty} f_n^{met}K_{n+1}(kd-ka)}. \tag{4.12}$$

Therefore, the expressions for the electric potentials in the region exterior to the PE–metallic cylinder system and inside the PE are given, respectively, by

$$\phi_{out}^{met} = \frac{\sigma}{k\varepsilon_0\varepsilon_1} \times \frac{K_0(kr') - \sum_{n=0}^{\infty} f_n^{met}\cos(n\psi)K_n(kr)}{K_1(ka) + f_0^{met}K_1(kd-ka) + \frac{1}{2}\sum_{n=1}^{\infty} f_n^{met}K_{n+1}(kd-ka)} \text{ in } D_0, \tag{4.13}$$

$$\phi_{in(s)}^{met} = \frac{\sigma}{k\varepsilon_0\varepsilon_1} \times \frac{K_0(ka) - \sum_{n=0}^{\infty} f_n^{met}K_n(kd-ka)}{K_1(ka) + f_0^{met}K_1(kd-ka) + \frac{1}{2}\sum_{n=1}^{\infty} f_n^{met}K_{n+1}(kd-ka)} \text{ in } D_2. \tag{4.14}$$

With the above results for the electric potential, the electrostatic free energy per unit length of the PE can be obtained by applying the charging procedure [32, 33]. The result, when normalized by k_BT, k_B being the Boltzmann constant and T the temperature, is

$$g_{el}^{met} = \frac{N l_B (1 - z\theta)^2}{b} \times \frac{K_0(ka) - \sum_{n=0}^{\infty} f_n^{met} K_n(kd - ka)}{kaK_1(ka) + kaf_0^{met} K_1(kd - ka) + \frac{1}{2} ka \sum_{n=1}^{\infty} f_n^{met} K_{n+1}(kd - ka)}. \quad (4.15)$$

Here l_B is the Bjerrum length defined by $l_B = q^2/4\pi\varepsilon_0\varepsilon_1 k_B T$ and b is the length of the cylinder per unit surface charge, that is, $\sigma(2\pi ab) = q$. N and b are related by $Nb = 1$. The factor of $(1 - z\theta)^2$ is introduced to account for CC. Specifically, z is the unsigned valence of counterions. Since θ is the number of counterions per charge on the PE, the effective, reduced surface charge density of the PE now becomes $\sigma(1 - z\theta)$ [24].

To determine CC, we consider the total free energy that consists of g_{el}^{met} and the entropic free energy needed to transfer the counterions from the bulk to the PE. Normalized by $k_B T$, the entropic energy per unit length is given by [24, 26]

$$g_{en} = N\theta \ln \frac{\theta}{\gamma \nu c Q}, \quad (4.16)$$

where γ is the activity coefficient for the bulk solution, ν is the number of the counterions in the chemical formula of the salt, c is the bulk salt concentration, and Q is the internal partition function of the condensed layer. Finally, the normalized total free energy per unit length of the PE is

$$g^{met} = g_{el}^{met} + g_{en}. \quad (4.17)$$

At equilibrium, the amount of CC θ satisfies [34]

$$\frac{\partial g^{met}}{\partial \theta} = \frac{\partial g_{el}^{met}}{\partial \theta} + \frac{\partial g_{en}}{\partial \theta} = 0. \quad (4.18)$$

In the original work of Manning for a single PE in a dilute solution, as $c \to 0$, two singular terms appear on the left hand side of the above equation. One is from g_{en} and is logarithmic in c, which is apparent from Eq. (4.16). The other term is from the electrostatic energy, which possesses the same logarithmic singularity. The cancelation of the two singular terms gives the amount of CC [24]. In the current formulation, because of the presence of the metallic cylinder, the electrostatic

energy is different, and exhibits different asymptotic behaviors in the dilute limit. We will demonstrate in the following that depending on the distance d between the PE and the cylinder, different θ can be obtained. In the limit where d approaches ∞, the effect of the metallic cylinder diminishes, and our result reduces to the CC on a PE in a solution alone. When the two cylinders are close, all the counterions are released and $\theta = 0$.

To show these results, we first write Eq. (4.18) in the following form

$$\frac{\partial g^{met}}{\partial \theta} = -2zN\xi(1 - z\theta) \times \frac{K_0(ka) - \sum_{n=0}^{\infty} f_n^{met} K_n\left[ka\left(\frac{d}{a} - 1\right)\right]}{kaK_1(ka) + kaf_0^{met}K_1\left[ka(\frac{d}{a} - 1)\right] + \frac{1}{2}ka\sum_{n=1}^{\infty} f_n^{met}K_{n+1}\left[ka(\frac{d}{a} - 1)\right]} - 2N\ln(ka) + N\ln\frac{4\pi e\theta l_B N_A a^2 \sum_i \nu_i z_i^2}{\gamma\nu Q} = 0, \quad (4.19)$$

where $\xi \equiv l_B/b$ is the dimensionless surface charge density and e is the base of the natural logarithm. Note that the salt concentration c has been written in terms of the Debye length using the relation $c^{-1} = 4\pi l_B N_A k^{-2} \sum_i \nu_i z_i^2$, where N_A is Avogadro's number, ν_i is the number of the i^{th} type of ion in the chemical formula of the salt and z_i is its valence [14, 23]. The dimensionless quantity d/a represents a normalized separation between the two cylinders. In the limit of dilute solution, $ka \to 0$, and the second term in $\partial g^{met}/\partial\theta$ has a logarithmic singularity. The first term, due to electrostatics, may also be singular as $ka \to 0$, since

$$K_0(x \to 0) \sim -\ln x, \quad K_n(x \to 0) \sim \frac{1}{2}\Gamma(n)\left(\frac{1}{2}x\right)^{-n}, \quad (4.20)$$

where $\Gamma(n)$ is the Gamma function of integer n [35]. This singular behavior, however, can be affected by the normalized separation d/a. This is apparent, since for a fixed value of ka, if $d/a \to \infty$, then $K_n[ka(d/a - 1)] = K_n(x \to \infty) = 0$, instead of having the asymptotic behavior shown in Eq. (4.20). In fact, by first holding ka fixed and taking the limit of $d/a \to \infty$, one would expect the result to correspond to the CC of the PE in the solution alone, as the metallic cylinder is located infinitely far from the PE. This is confirmed by using $K_n(x \to \infty) = 0$ in $\partial g^{met}/\partial\theta$,

resulting in

$$-2zN\xi(1-z\theta)\frac{K_0(ka)}{kaK_1(ka)}-2N\ln(ka)+N\ln\frac{4\pi e\theta l_B N_A a^2\sum_i \nu_i z_i^2}{\gamma\nu Q}=0. \quad (4.21)$$

Now in the dilute limit where $ka \to 0$, there are two singular terms in the above expression, both logarithmic in ka. One comes from the entropic energy $-2N\ln(ka)$ and the other results from $K_0(ka)/kaK_1(ka) \sim -\ln(ka)$. Cancelation of these two terms retrieves the amount of CC on a PE isolated from the metallic cylinder [24]

$$\theta=\theta_0=\frac{1}{z}\left(1-\frac{1}{z\xi}\right). \quad (4.22)$$

If on the contrary, the PE is close to the metallic cylinder in the sense that d/a remains constant as $ka \to 0$, then using the asymptotic relation, Eq. (4.20), the equation to determine θ becomes

$$\frac{-2zN\xi(1-z\theta)\left[\frac{\ln(ka)}{\ln(ka\cdot r_0/a)}-1\right]}{1+\frac{1}{d/a-1}\frac{\ln(ka)}{\ln(ka\cdot r_0/a)}-\frac{1}{\pi(d/a-1)}\sum_{n=1}^{\infty}\left[n\left(\frac{r_0/a}{d/a-1}\right)^n\int_0^{2\pi}\ln\left[\Lambda(\psi)\right]\cos(n\psi)d\psi\right]}$$
$$\times\ln(ka)-2N\ln(ka)=0. \quad (4.23)$$

Detailed procedure to obtain this equation is given in Appendix A. Here the apparent non-singular terms are not included. Since r_0/a is a geometric factor that does not vary as $ka \to 0$, the term $\ln(ka)/\ln(ka\cdot r_0/a)$ approaches one, and therefore the first term in Eq. (4.23) is zero. This implies that if there were CC, the only singular term is from the entropic contribution, and equilibrium cannot be reached. Therefore, the amount of CC has to be zero when the PE is close to the metallic cylinder,

$$\theta=0. \quad (4.24)$$

At this point, one may wonder whether there exists a smooth transition between the two limiting cases demonstrated above. In particular, one may ask what happens when the PE is gradually moved from the bulk solution to the neighborhood of the metallic cylinder. To be able to see the transition, we introduce a scaling relation between the dimensionless separation d/a and the dimensionless Debye length ka

$$\frac{d}{a}=A\,(ka)^{-\alpha}, \quad (4.25)$$

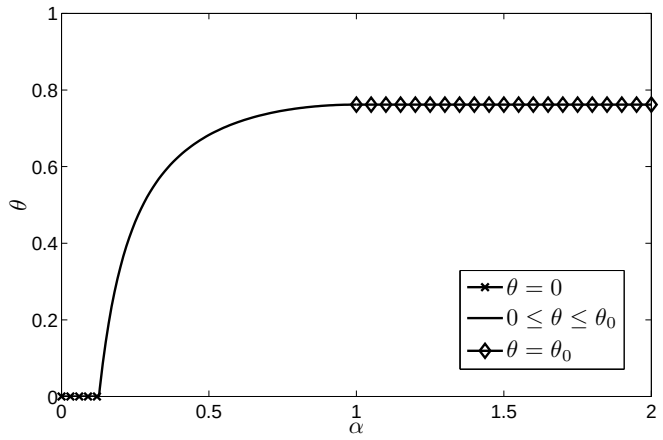

Figure 4.2: Dependence of the amount of CC θ on α for the PE–metallic cylinder system, where α is defined from the scaling relation, $d/a = A(ka)^{-\alpha}$, between the dimensionless separation d/a and the dimensionless Debye length ka. The solid line represents the smooth transition between the two limiting cases $\theta = 0$ and $\theta = \theta_0$. Here, $z = 1$ and $\xi = 4.2$.

where α is a non-negative number, and A is a non-negative constant. The situation of $\alpha \geq 1$ corresponds to a rapid increase of separation d/a during the dilution ($ka \to 0$), namely, the case of a PE alone. If $\alpha = 0$, then d/a remains fixed during the dilution, and the second limiting case above is retrieved. When $\alpha \in (0, 1)$, then the singularity of $\ln(d/a)$ is of the same order as that of $\ln(ka)$, that is, $\ln(d/a) \sim -\alpha \ln(ka)$. Hence, the amount of CC depends on α, which captures the magnitude of the separation relative to the dilution. A similar approach has been employed by Ray and Manning to investigate the interaction between two identically charged rodlike polyions at intermediate separation distances [36]. Applying Eq. (4.25) and conducting asymptotic analysis (See Appendix A for details) for $\alpha \in (0, 1)$, θ is found to be the solution to the following equation

$$-2zN\xi(1 - z\theta)\left[-1 + (1 - \alpha)^2\right] \ln(ka) - 2N \ln(ka) = 0. \tag{4.26}$$

resulting in

$$\theta = \frac{1}{z}\left[1 - \frac{1}{z\xi\alpha\,(2 - \alpha)}\right],\ \alpha \in (0, 1). \tag{4.27}$$

Figure 4.2 shows the CC θ as a function of α for $\alpha \in (0, 1)$. The calculations are performed for the case of univalent counterions $z = 1$, and the dimensionless

surface charge density $\xi = 4.2$. This value corresponds to the charge density of a double-stranded DNA (dsDNA) [15]. As expected, as α approaches 1, θ approaches the value given by Eq. (4.22). As α reduces, θ decreases, indicating that some of the counterions previously condensed are released. Before α reaches 0, θ has reduced to 0, corresponding to complete release of the counterions. Further decreasing α in Eq. (4.27) will result in negative θ, which is not physical. Therefore, θ stays to be 0 after complete release of the counterions.

In the absence of the metallic cylinder, the electric potential on the surface of the PE is given by [24]

$$\phi_0 = \frac{\sigma K_0(ka)}{\varepsilon_0 \varepsilon_1 k K_1(ka)}. \tag{4.28}$$

In the dilute limit of $ka \rightarrow 0$, the electric potential above exhibits logarithmic singularity. It is this singularity that contributes to the amount of CC given by Eq. (4.22). With the metallic cylinder, the electric potential is modified to Eq. (4.14) and the amount of CC is reduced. This reduction implies that the singularity in the electric potential has become smaller. In other words, the electric potential of the PE is weakened by the presence of the metallic cylinder.

4.4 Polyelectrolyte near a dielectric cylinder

For a PE near a dielectric cylinder, with the same geometry shown in Figure 4.1, the governing equation inside the cylinder (domain D_1) and the boundary condition on its surface have changed. In particular, assuming that there are no charges inside or on the surface of the dielectric cylinder, the governing equations for the electric potential now become

$$\nabla^2 \phi_{out}^{diel} = k^2 \phi_{out}^{diel} \text{ in } D_0, \tag{4.29}$$

$$\nabla^2 \phi_{in(l)}^{diel} = 0 \text{ in } D_1, \tag{4.30}$$

and

$$\nabla^2 \phi_{in(s)}^{diel} = 0 \text{ in } D_2. \tag{4.31}$$

Here the superscript "diel" represents the case of the dielectric cylinder, whereas the subscripts "out", "in(l)" and "in(s)" represents the domains of the electrolyte

solution, inside the dielectric cylinder and inside the PE, respectively. The boundary conditions, assuming uniform potential on the surface of the PE (and therefore inside), are

$$\lim_{r\to\infty} \phi_{out}^{diel} = 0, \tag{4.32a}$$

$$\phi_{in(l)}^{diel}\Big|_{r=r_0} = \phi_{out}^{diel}\Big|_{r=r_0}, \tag{4.32b}$$

$$\varepsilon_2 \frac{\partial \phi_{in(l)}^{diel}}{\partial r}\Big|_{r=r_0} = \varepsilon_1 \frac{\partial \phi_{out}^{diel}}{\partial r}\Big|_{r=r_0}, \tag{4.32c}$$

$$\phi_{in(s)}^{diel}\Big|_{r'=a}^{\psi'=0} = \phi_{out}^{diel}\Big|_{r'=a}^{\psi'=0}, \tag{4.32d}$$

$$\varepsilon_1 \frac{\partial \phi_{out}^{diel}}{\partial r'}\Big|_{r'=a}^{\psi'=0} = -\frac{\sigma}{\varepsilon_0}. \tag{4.32e}$$

The difference in BCs here from the case of PE–metallic cylinder system is Eq. (4.32c), which comes from the requirement that the normal component of the electric displacement is continuous on the surface of the dielectric cylinder [29]. As in Section 4.3, Eqs. (4.32d) and (4.32e) are approximated BCs on the surface of the PE.

We use a similar procedure to solve for the electric potential as introduced in Section 4.3. Applying the method of separation of variables to Eqs. (4.29) and (4.30) and using BC (4.32a), solutions for the electric potentials are given by $\phi_{out}^{diel} = \sum_{n=0}^{\infty} a_n^{diel} \cos(n\psi) K_n(kr) + C_0^{diel} K_0(kr')$ in D_0 and $\phi_{in(l)}^{diel} = \sum_{l=0}^{\infty} b_l^{diel} \cos(l\psi) r^l$ in D_1, respectively. The unknown coefficients a_n^{diel}, C_0^{diel}, b_l^{diel} are determined from the BCs (4.32b)–(4.32e). Finally, we obtain the following expressions for the electric potential outside the two cylinders and inside the PE

$$\phi_{out}^{diel} = \frac{\sigma}{\varepsilon_0 \varepsilon_1 k} \times \frac{K_0(kr') - \sum_{n=0}^{\infty} f_n^{diel} \cos(n\psi) K_n(kr)}{K_1(ka) + f_0^{diel} K_1(kd-ka) + \frac{1}{2}\sum_{n=1}^{\infty} f_n^{diel} K_{n+1}(kd-ka)} \text{ in } D_0, \tag{4.33}$$

$$\phi_{in(s)}^{diel} = \frac{\sigma}{\varepsilon_0 \varepsilon_1 k} \times \frac{K_0(ka) - \sum_{n=0}^{\infty} f_n^{diel} K_n(kd-ka)}{K_1(ka) + f_0^{diel} K_1(kd-ka) + \frac{1}{2}\sum_{n=1}^{\infty} f_n^{diel} K_{n+1}(kd-ka)} \text{ in } D_2, \tag{4.34}$$

where

$$f_n^{diel} = \begin{cases} \frac{1}{2\pi K_1(kr_0)} \int_0^{2\pi} \frac{(r_0 - d\cos(\psi))K_1[ka\Lambda(\psi)]}{a\Lambda(\psi)} d\psi, & n = 0 \\ \frac{\varepsilon_2}{\pi(\varepsilon_1+\varepsilon_2)K_n(kr_0)} \int_0^{2\pi} K_0\left[ka\Lambda(\psi)\right]\cos(n\psi)d\psi & \\ + \frac{\varepsilon_1 kr_0}{\pi(\varepsilon_1+\varepsilon_2)K_n(kr_0)n} \int_0^{2\pi} \frac{(r_0 - d\cos(\psi))K_1[ka\Lambda(\psi)]}{a\Lambda(\psi)} \cos(n\psi)d\psi, & n > 0. \end{cases} \tag{4.35}$$

The electric potential $\phi_{in(l)}^{diel}$ in D_1 is not used in further derivations and its final form is not included here.

The electrostatic free energy per unit length of the PE near the dielectric cylinder can be obtained by performing the charging procedure. Its normalized value by k_BT is

$$g_{el}^{diel} = N\xi(1 - z\theta)^2 \times \frac{K_0(ka) - \sum_{n=0}^{\infty} f_n^{diel} K_n(kd - ka)}{kaK_1(ka) + kaf_0^{diel}K_1(kd - ka) + \frac{1}{2}ka\sum_{n=1}^{\infty} f_n^{diel} K_{n+1}(kd - ka)}. \tag{4.36}$$

To determine θ, the entropic free energy Eq. (4.16) is added to Eq. (4.36) and the total free energy is minimized with respect to θ. Conducting asymptotic analysis of the resulting equation, letting $ka \to 0$ while keeping d/a fixed, the expression for the amount of CC in this case is given by

$$\theta = \frac{1}{z}\left[1 - \frac{1}{\xi z}\left(1 + \frac{\varepsilon_1}{\pi(\varepsilon_1+\varepsilon_2)}\sum_{n=1}^{\infty}\left(\frac{r_0/a}{d/a - 1}\right)^{n+1}\int_0^{2\pi} t_n d\psi\right)\right], \tag{4.37}$$

$$t_n = \frac{1}{\Lambda^2(\psi)}\left[\frac{r_0}{a}\cos(n\psi) + \frac{d}{a}\left(\frac{\varepsilon_2}{\varepsilon_1}\sin(\psi)\sin(n\psi) - \cos(\psi)\cos(n\psi)\right)\right].$$

When $\varepsilon_2/\varepsilon_1 = 1$ and $d > r_0$ (this is true since the interiors of the PE and the dielectric cylinder cannot overlap), the integral in the above expression can be shown to be exactly zero. Therefore, the amount of CC becomes identical to the CC on the PE if the dielectric cylinder is removed [14], θ_0 in Eq. (4.22), independent of the separation between the centers of the PE and the dielectric cylinder. When

$\varepsilon_2/\varepsilon_1 \neq 1$, numerical calculation of Eq. (4.37) shows that θ can be smaller or larger than θ_0. Specifically, as shown in Figure 4.3, when $\varepsilon_2/\varepsilon_1 > 1$, as the separation between the PE and the dielectric cylinder decreases, counterions are gradually released from the surface of the PE. This is in fact consistent with the results for the PE–metallic cylinder system, since metal can be considered to have infinitely large dielectric constant. When $\varepsilon_2/\varepsilon_1 < 1$, more CC is observed ($\theta > \theta_0$) as the separation between the PE and the dielectric cylinder decreases. These results suggest that the electric potential is strengthened by the dielectric cylinder when its dielectric constant is smaller than that of the solution, while weakened when its dielectric constant is larger than that of the solution. In all cases, as the separation between the PE and the dielectric cylinder approaches ∞, the electric potential of the PE–dielectric cylinder system approaches that of a PE alone in a solution, and $\theta \to \theta_0$.

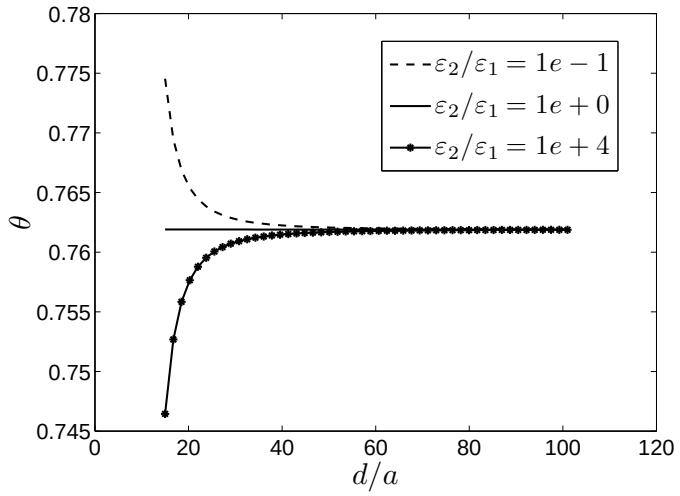

Figure 4.3: Dependence of the amount of CC θ on the dimensionless distance d/a between the PE and the dielectric cylinder, for different values of $\varepsilon_2/\varepsilon_1$. Here, $z = 1$, $\xi = 4.2$, $r_0/a = 10$ and $d/a \in [15, 100]$.

4.5 Conclusion and discussions

In this work, we studied the effect of an electronically responsive cylinder on the electrostatics of a PE within the framework of CC. Our results show that as the PE

is moved from the bulk solution to the vicinity of a metallic cylinder, the amount of counterions previously condensed on the PE is gradually released and eventually becomes zero. For a PE near a dielectric cylinder, the amount of CC on the PE depends on the dielectric constant of the cylinder ε_2 relative to that of the solution ε_1. When $\varepsilon_2/\varepsilon_1 > 1$, the counterions are gradually released from the surface of the PE as the PE approaches the cylinder. When $\varepsilon_2/\varepsilon_1 < 1$, however, more counterions are condensed on the surface of the PE. Lastly, when $\varepsilon_2/\varepsilon_1 = 1$, the amount of CC remains constant, independent of the separation between the PE and the dielectric cylinder.

To facilitate the calculations, we have made the approximation that the electric potential on the surface of the PE is uniform. We expect this approximation to be good as long as the size of the PE is much smaller than other dimensions in the system. In the following, we examine the self-consistency of this approximation. Specifically, we have assumed that the electric potential inside the PE $\phi_{in(s)}$ is a constant and is equal to the electric potential in the solution evaluated at the particular point of $(r' = a, \psi' = 0)$, i.e., $\phi_{in(s)} = \phi_{out}(r' = a, \psi' = 0)$. Here the superscripts met and $diel$ have been removed with the reference to the corresponding potential in each case. Under this assumption, $\phi_{in(s)} \neq \phi_{out}$ at any other points on the surface of the PE. In fact, the maximum difference between $\phi_{in(s)}$ and ϕ_{out} occurs at $(r' = a, \psi' = \pi)$. Below, we evaluate this difference through the percentage error defined as

$$\eta_1 = \left| \frac{\bar{\phi}_{out}\Big|_{\bar{r}'=\bar{a}}^{\psi'=\pi} - \bar{\phi}_{in(s)}}{\bar{\phi}_{out}\Big|_{\bar{r}'=\bar{a}}^{\psi'=\pi}} \right| \times 100, \tag{4.38}$$

where the normalized quantities are given by

$$\bar{\phi}_{out} = \varepsilon_0\varepsilon_1 k\phi_{out}/\sigma, \bar{\phi}_{in(s)} = \varepsilon_0\varepsilon_1 k\phi_{in(s)}/\sigma, \bar{r} = kr, \bar{r}' = kr',$$
$$\bar{r}_0 = kr_0, \bar{a} = ka, \bar{d} = kd. \tag{4.39}$$

Expressions for the normalized electric potential are provided in Appendix A. In addition, the jump condition for the electric displacement is approximated by $(\partial\phi_{out}/\partial r')\,|_{r'=a}^{\psi'=0} = -\sigma/\varepsilon_0\varepsilon_1$, i.e., $\left(\partial\bar{\phi}_{out}/\partial\bar{r}'\right)|_{\bar{r}'=\bar{a}}^{\psi'=0} + 1 = 0$. Elsewhere on the surface of the PE, $\partial\bar{\phi}_{out}/\partial\bar{r}' + 1 = 0$ is not satisfied and the greatest error occurs at

($\bar{r}' = \bar{a}, \psi' = \pi$). The following quantity

$$\eta_2 = \left| \frac{\partial \bar{\phi}_{out}}{\partial \bar{r}'} \Big|_{\bar{r}'=\bar{a}}^{\psi'=\pi} + 1 \right| \times 100, \tag{4.40}$$

is used to quantify the percentage error in the electric displacement.

Commonly used PE radius a ranges from 0.1 Å to 100 Å [37], while the Debye length is usually taken to be in the range of 0.1 nm to 100 nm. The normalized quantity $\bar{a}$ is hence between 10^{-4} and 100. In the following, we first calculate η_1 and η_2 for a dilute electrolyte with dielectric constant $\varepsilon_1 = 80$ and Debye length of 100 nm. The radius a of the PE is taken to be 10 Å, and the dielectric constant of the dielectric cylinder is $\varepsilon_2 = 1$. Hence $\bar{a} = 10^{-2}$ and $\varepsilon_2/\varepsilon_1 = 0.0125$. Figures 4.4–4.7 show the contour plots of η_1 and η_2 for the PE–metallic cylinder and the PE–dielectric cylinder systems, as a function of the normalized radius of the cylinder $\bar{r}_0$ and the normalized separation distance $\bar{d}$ between the PE and the corresponding cylinder. For the PE–metallic cylinder system, when $\bar{d} > 0.85$ and $\bar{r}_0 > 0.14$, η_1 is less than 5 percent (See Figure 4.4), while η_2 is less than 5 percent when $\bar{d}$ and $\bar{r}_0$ are larger than 1.9 and 0.35, respectively (See Figure 4.5). For the PE–dielectric cylinder system, η_1 is less than 0.5 percent when $\bar{d}$ is beyond 1.08 and $\bar{r}_0$ is beyond 0.42 (See Figure 4.6); when $\bar{d} > 1.55$ and $\bar{r}_0 > 0.5$, η_2 is within 0.5 percent (See Figure 4.7). For higher salt concentrations, it is expected that the approximation will be better due to the stronger screening from ions. This is confirmed through our numerical calculations. For example, for the dimensions $a = 10$ Å, $r_0 = 10$ nm, $d = 20$ nm, we found that: 1) for the PE–metallic cylinder system, $\eta_1 = 8.41\%$ and $\eta_2 = 9.67\%$ when $k^{-1} = 100$ nm, whereas $\eta_1 = 7.4 \times 10^{-3}\%$ and $\eta_2 = 1.28 \times 10^{-7}\%$ when $k^{-1} = 1$ nm; 2) for the PE–dielectric cylinder system, $\eta_1 = 0.67\%$ and $\eta_2 = 3.33\%$ when $k^{-1} = 100$ nm and $\eta_1 = 1.03 \times 10^{-6}\%$ and $\eta_2 = 5.38 \times 10^{-7}$ when $k^{-1} = 1$ nm.

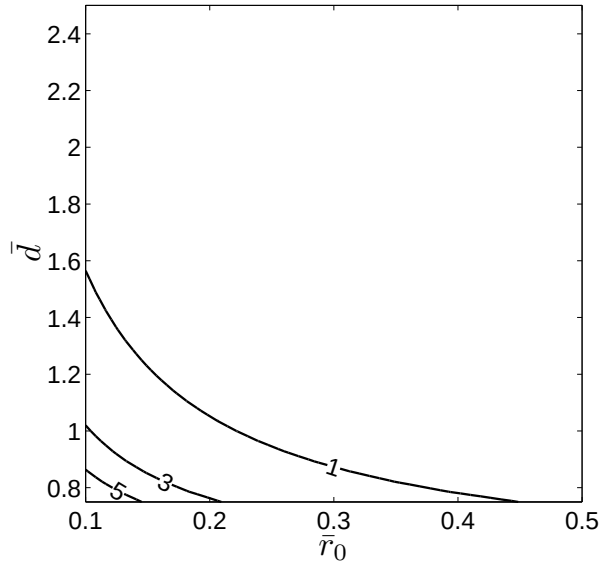

Figure 4.4: Percentage error η_1 for the PE–metallic cylinder system, where $\bar{r}_0$ is the normalized radius of the metallic cylinder and $\bar{d}$ is the normalized distance between the PE and the metallic cylinder. Here $\bar{a} = 10^{-2}$.

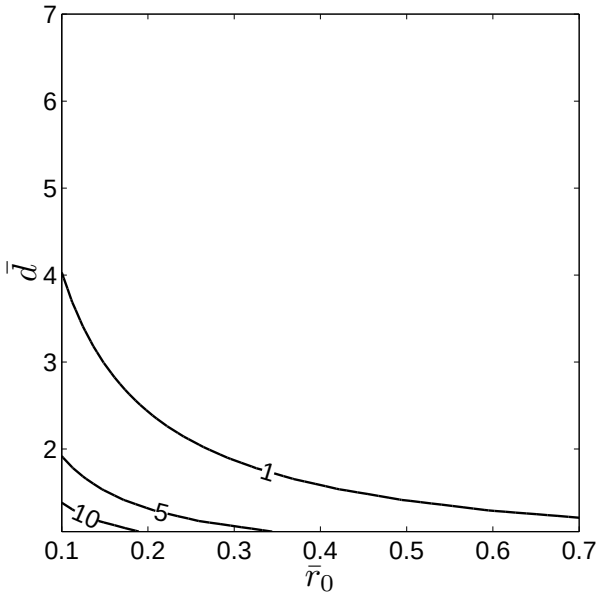

Figure 4.5: Percentage error η_2 for the PE–metallic cylinder system,where $\bar{r}_0$ is the normalized radius of the metallic cylinder and $\bar{d}$ is the normalized distance between the PE and the metallic cylinder. Here $\bar{a} = 10^{-2}$.

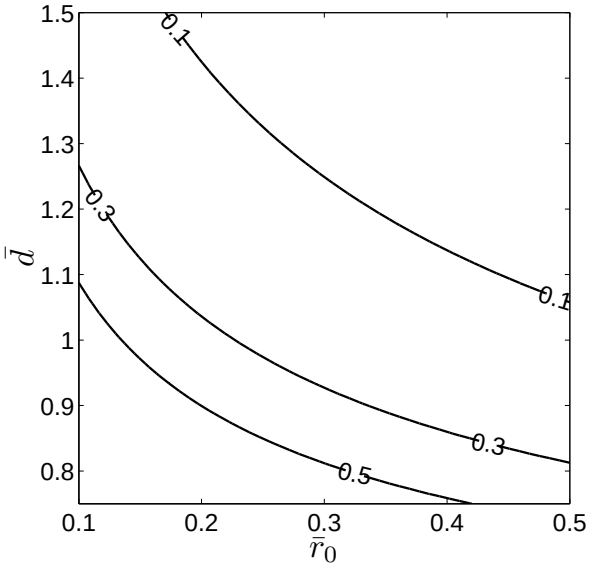

Figure 4.6: Percentage error η_1 for the PE–dielectric cylinder system,where $\bar{r}_0$ is the normalized radius of the dielectric cylinder and $\bar{d}$ is the normalized distance between the PE and the dielectric cylinder. Here $\bar{a} = 10^{-2}$ and $\varepsilon_2/\varepsilon_1 = 0.0125$.

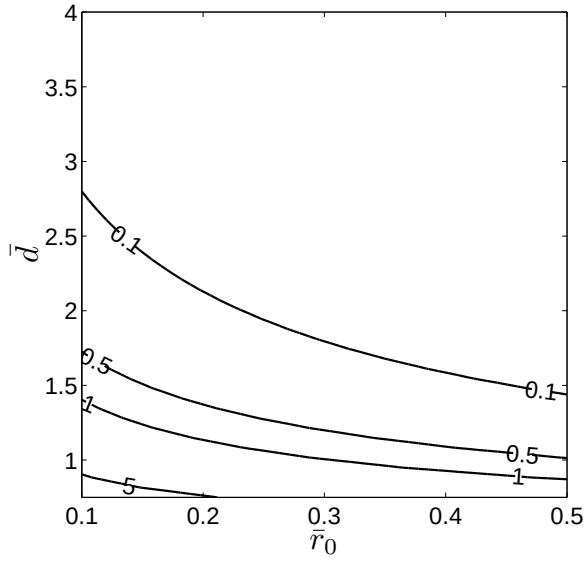

Figure 4.7: Percentage error η_2 for the PE–dielectric cylinder system,where $\bar{r}_0$ is the normalized radius of the dielectric cylinder and $\bar{d}$ is the normalized distance between the PE and the dielectric cylinder. Here $\bar{a} = 10^{-2}$ and $\varepsilon_2/\varepsilon_1 = 0.0125$.

Bibliography

[1] Patolsky, F.; Zheng, G.; Hayden, O.; Lakadamyali, M.; Zhuang, X.; Lieber, C.M. *Proc. Natl. Acad. Sci. U.S.A.* **2004**, *101*, 14017.

[2] Hahm, J. ; Lieber, C.M. *Nano Lett.* **2004**, *4*, 51.

[3] Bianco, A.; Kostarelos, K.; Prato, M. *Curr. Opin. Chem. Biol.* **2005**, *9*, 674.

[4] Tarlov, M.J., Steel, A.B., in: J.F. Rusling (Ed.), Biomolecular Films: Design, Function, and Applications, in: Surfactant Science Series, vol. 111, Dekker, New York, 2003.

[5] Komarova, E.; Aldissi, M.; Bogomolova, A. *Biosens. Bioelectron.* **2005**, *21*, 182.

[6] Riccardi, C.S.; Dahmouche, K.; Santilli, C.V.; da Costa, P.I.; Yamanaka, H. *Talanta* **2006**, *70*, 637.

[7] Lin, X.H.; Wan, H.Y.; Zhang, Y.F.; Chen, J.H. *Talanta* **2008**, *74*, 944.

[8] Zheng, M.; Jagota, A.; Semke, E.D.; Diner, B.A.; Mclean, R.S.; Lustig, S.R.; Richardson, R.E.; Tassi, N.G. *Nat. Mater.* **2003**, *2*, 338.

[9] Zheng, M.; Jagota, A.; Strano, M.S.; Santos, A.P.; Barone, P.; Chou, S.G.; Diner, B.A.; Dresselhaus, M.S.; Mclean, R.S.; Onoa, G.B.; Samsonidze, G.G.; Semke, E.D.; Usrey, M.; Walls, D.J. *Science* **2003**, *302*, 1545.

[10] Guo, Z.; Sadler, P.J.; Tsang, S.C. *Adv. Mater.* **1998**, *10*, 701.

[11] Okada, T.; Kaneko, T.; Hatakeyama, R.; Tohji, K. *Chem. Phys. Lett.* **2006**, *417*, 288.

[12] Gao, H.; Kong, Y.; Cui, D. *Nano Lett.* **2003**, *3*, 471.

[13] Manning, G.S. *J. Chem. Phys.* **1969**, *51*, 924.

[14] Manning, G.S. *Quart. Rev. Biophys. II* **1978**, *2*, 179.

[15] Manning, G.S. *Ber. Bunsen-Ges.* **1996**, *100*, 909.

[16] Ikegami, A. *J. Polym. Sci.* **1964**, *2*, 907.

[17] Gregor, H.P.; Frederick, M. *J. Polym. Sci.* **1957**, *23*, 451.

[18] Keyser, U. F.; Koeleman, B.E.; van Dorp S.; Krapf, D.; Smeets, R.M.M.; Lemay, S.G.; Dekker, N.H.; Dekker, C. *Nature Physics* **2006**, *2*, 473.

[19] Young, M. A.; Jayaram, B.; Beveridge, D. L. *J. Am. Chem. Soc.* **1997,** *119,* 59.

[20] Hill, T.L., An introduction to statistical thermodynamics, New York : Dover Publications, 1986.

[21] Brenner, S.L.; McQuarrie, D.A. *J. theor. Biol.* **1973**, *39*, 343.

[22] Brenner, S.L.; McQuarrie, D.A. *J. Colloid Interface Sci.* **1973**, *44*, 298.

[23] Russel, W.B., Saville, D.A., Schowalter, W.R., Colloidal Dispersions, Cambridge Univ. Press, Cambridge, 1989.

[24] Manning, G.S. *J. Phys. Chem B* **2007**, *111*, 8554.

[25] Zimm, B.H.; Le Bret M. *J. Biomol. Struct. Dyn.* **1983**, *1*, 461.

[26] Tang, T.; Jagota, A.; Hui, C.Y. *J. Colloid Interface Sci.* **2006**, *299*, 564.

[27] Tang, T.; Hui, C.Y.; Jagota, A. *J. Colloid Interface Sci.* **2006**, *299*, 572.

[28] Malysheva, O.; Tang, T.; Schiavone, P. *J. Colloid Interface Sci.* **2008**, *327*, 251.

[29] Jackson, J.D., Classical Electrodynamics, third ed., Wiley, New York, 1999.

[30] Cochran, J.A., Wiser, H.C., Rice, B.J., Advanced engineering mathematics, second ed., Brooks/Cole Publishing Company, Monterey, California, 1987.

[31] Davis, H.R., Fourier series and orthogonal functions, Allyn and Bacon, Inc., Boston, 1963.

[32] Israelachvili, J.N., Intermolelucar and Surface Forces, second ed., Academic Press, London, 1992.

[33] Lifson, S.; Katchalsky, A. *J. Polym. Sci.* **1954**, *13*, 43.

[34] Manning, G.S. *Macromolecules* **2007**, *40*, 8071.

[35] Abramovitz, M.; Stegun, I.A. Handbook of Mathematical Functions. Dover, New-York, 1965.

[36] Ray, J.; Manning, G.S. *Langmuir* **1994,** *10,* 2450.

[37] Stigter, D. *Biophys. J.*, **1995**, *69*, 380.

Chapter 5
Binding Force between a Charged Wall and a Complex formed by a Polyelectrolyte and an Electronically Responsive Cylinder[1]

5.1 Introduction

This work is motivated by the recent experiments of DNA-assisted carbon nanotube (CNT) separation using ion-exchange chromatography (IEC). CNT is a novel material that has shown promise in many practical applications [1–3]. However, before these applications become widely possible, it is necessary to resolve the fundamental problem of separating as-produced bundled CNTs according to their properties. In particular, depending on its chirality [4], a CNT can be metallic or semiconducting and the band gap of the latter is inversely proportional to its diameter [4]. Several methods have been proposed for separating CNTs in order to take advantage of their unique electronic properties [5–9]. In particular, Zheng *et al.* developed a method to separate CNTs according to their chiralities using single-stranded DNA (ssDNA) molecules [8, 9]. It was found that in an electrolyte solution ssDNA molecules form hybrids with CNTs by wrapping around them in a helical way, effectively dispersing the bundled CNTs. These CNT-DNA hybrids are negatively charged in an electrolyte solution because of the deprotonated phosphate groups on the DNA backbones. Applying the method of ion exchange chromatography (IEC), the CNT-DNA hybrids can be separated according to the electronic properties of the CNT core. In the IEC method, the negatively charged hybrids are adsorbed on a positively charged column. With increasing salt concentration, experimental results

[1]Reprinted with permission from : "Binding Force between a Charged Wall and a Complex formed by a Polyelectrolyte and an Electronically Responsive Cylinder", Oxana Malysheva, Tian Tang and Peter Schiavone, J. of Adhesion, 2011, 87, pp 251-271. Copyright 2011 Taylor&Francis Group, LLC. http://www.informaworld.com/smpp/title content=t713453635

show that the metallic CNT-DNA hybrids elute earlier from the oppositely charged column than the semiconducting CNT-DNA hybrids. Lustig *et al.* [10] developed an analytically tractable model for such an observation, where a CNT-DNA hybrid is presented by a metallic or a dielectric cylinder (representing the CNT) wrapped around by a helical line of charges (representing the DNA). The binding free energy of a hybrid to the positively charged column is compared to the energy of a hybrid suspended in a solution with counterion condensation (CC) [11]. These two quantities, together with the interaction energy between the solution and the column, define the elution free energy, which governs the elution of the CNT-DNA hybrids in IEC. It is shown that for the same tube radius and helical wrapping angle, the salt concentration at which elution occurs is smaller for hybrids with a metallic core than for those with a dielectric core, indicating that the former should elute earlier from the column. This is in agreement with experiments [8, 9]. However in [10], the electronic response of the CNT to the DNA charges is considered only at the level of image charges, which is approximate, and the CNT is modeled locally as a half space. A solution to the electric potential from a rigorously defined boundary value problem (BVP) is not provided.

In this work, we study the binding between a positively charged wall and a complex consisting of a negatively charged polyelectrolyte (PE) and an electronically responsive cylinder (shortened to PE-cylinder complex), immersed in an electrolyte solution. We take a different approach from [10] and directly calculate the binding force between them. The electronically responsive cylinder is again modeled as either a metal or a dielectric, but instead of using the image charge method, the field equations describing the electrostatics of metal or dielectric are rigorously incorporated and the corresponding boundary value problem for the electric potential is solved. We also consider a simpler geometry and model the PE as a thin cylinder near the electronically responsive cylinder. By thin cylinder we mean that the radius of the PE is much smaller than that of the responsive cylinder. Such simpler geometry allows us to obtain an analytical solution for the electric potential and the binding force. Through this work, we demonstrate how the binding force changes with the nature of the electronically responsive cylinder.

This paper is organized as follows, the problem description and applied methods are presented in Section 5.2. The expressions for the binding force between the PE-cylinder complexes and the charged wall are shown in Section 5.3. Finally, results and discussions are given in Sections 5.4 and 5.5, respectively.

5.2 Problem description

The system under consideration consists of a PE-cylinder complex and a charged wall embedded in a dilute electrolyte solution. The geometrical representation of the system is depicted in Figure 5.1. The electronically responsive cylinder is modeled as a cylinder with radius r_0; whereas, the PE is modeled as a thin charged cylinder of radius a. The diameter of a single-walled CNT (swCNT) ranges from 0.7 nm to 10 nm [4], and the commonly used radius of a PE ranges from 0.1 Å to 100 Å [12]. Since for ssDNA, its charges are confined in a small region around the backbone, we consider the case where the radius of the PE is much smaller than the radius of the responsive cylinder, that is, $a << r_0$. The axes of the PE and the cylinder are parallel and the distance between their centers is denoted by d. The charged wall is located parallel to the axes of the PE-cylinder complex at a distance d_2 from the center of the PE (See Figure 5.1). The separation distance between the center of the responsive cylinder and the wall is denoted as d_1 and it is equal to $d_1 = d + d_2$. The PE has a uniform surface charge density denoted as σ_{PE}. The wall has a uniform surface charge denoted as σ_{S}, which is of opposite sign to σ_{PE}, that is, $\sigma_{\text{S}}\sigma_{\text{PE}} < 0$. The PE-cylinder complex is assumed to be infinitely long and the charged wall is semi-infinite, so the problem can be considered two-dimensional, as shown in Figure 5.1. The exterior region to the PE-cylinder complex and the wall, which is denoted as D_0, is occupied by an electrolyte solution with dielectric constant ε_1. The interior of the electronically responsive cylinder D_1 can be a metallic substance or a dielectric with dielectric constant ε_2. The interior of the PE D_2 is assumed to be a vacuum with dielectric constant equal to 1. We denote by (r, ψ) and (x, y) the generic polar and Cartesian coordinates, respectively, with the origin located at the center of the cylinder; (r', ψ') are polar coordinates with the origin

located at the center of the PE. The electric potential is more conveniently described in one of the two sets of polar coordinates, depending on the domain. The Cartesian coordinates are used to calculate the binding force. These coordinates can be easily converted using the following relations

$$r = \sqrt{x^2 + y^2},\ \psi = \arctan\frac{y}{x},\ r' = \sqrt{(x-d)^2 + y^2},\ \psi' = \arctan\frac{y}{d-x}. \quad (5.1)$$

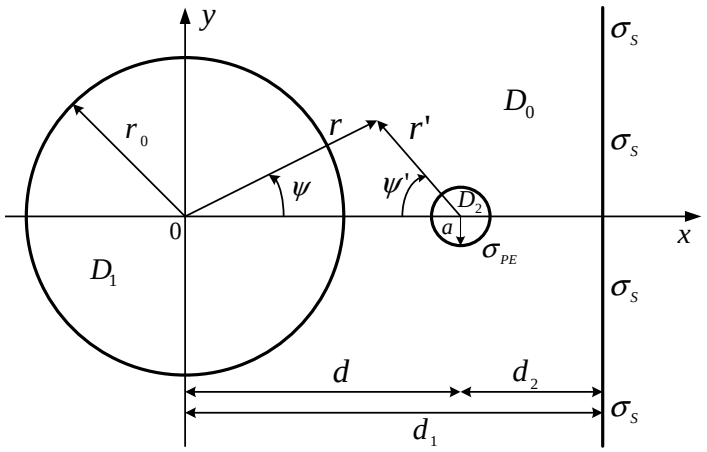

Figure 5.1: Geometry of the electronically responsive cylinder with radius r_0 and the PE with radius a near the charged wall. d is the distance between the centers of the cylinder and the PE, d_2 is the distance from the center of the PE to the charged wall, and d_1 is the distance between the center of the responsive cylinder and the wall. σ_{PE} and σ_S are the surface charge densities on the PE and the charged wall, respectively. (r, ψ) and (x, y) are polar and Cartesian coordinates with the origin at the center of the cylinder, and (r', ψ') are polar coordinates with the origin at the center of the PE. D_0 is the exterior region to the PE-cylinder complex and the wall; D_1 and D_2 are interior regions of the cylinder and the PE, respectively.

The BVP for the electric potential in the entire domain is described below. The governing equation for the electric potential ϕ_0 in D_0 is the Debye-Hückle equation [11, 13]

$$\nabla^2\phi_0 = k^2\phi_0 \text{ in } D_0, \quad (5.2)$$

where k is the inverse of the Debye length [13]. The Debye length defines the length in the electrolyte solution beyond which the electric potential is screened. It scales with the salt concentration c as $k^{-1} \sim c^{-1/2}$ [13], which means that as the

salt concentration increases, the Debye length decreases, and the electric potential becomes more screened. The governing equation for the electric potential ϕ_2 in D_2 is a Laplace equation

$$\nabla^2\phi_2 = 0 \text{ in } D_2, \tag{5.3}$$

where ∇^2 is the Laplacian. Equations (5.2) and (5.3) govern the electric potential in regions D_0 and D_2, no matter whether the cylinder is metallic or dielectric. In the following, superscript "met" or "diel" are used to differentiate the cases of metallic and dielectric cylinders. For example, for the PE-metallic cylinder complex ϕ_0^{met} and ϕ_2^{met} are the electric potentials in D_0 and D_2, respectively. The electric potential ϕ_1 inside the electronically responsive cylinder D_1, depends on the nature of the cylinder. Inside a metallic cylinder the electric field must vanish and therefore the electric potential is a constant independent of position [14, 15], that is,

$$\phi_1^{\text{met}} = \phi_c \text{ in } D_1, \tag{5.4}$$

where the superscript "met" stands for the metallic cylinder, and ϕ_c is a constant [14, 15]. The electric potential ϕ_1^{diel} inside a neutral dielectric cylinder D_1 satisfies [14]

$$\nabla^2\phi_1^{\text{diel}} = 0 \text{ in } D_1. \tag{5.5}$$

The boundary conditions (BCs) described below are the same for the PE-metallic cylinder and the PE-dielectric cylinder complexes. Consequently, the superscripts "met" and "diel" are omitted.

$$\lim_{r\to\infty} \phi_0 = 0, \tag{5.6a}$$

$$\phi_0\big|_{r=r_0} = \phi_1\big|_{r=r_0}, \tag{5.6b}$$

$$\phi_0\big|_{r'=a} = \phi_2\big|_{r'=a}, \tag{5.6c}$$

$$\varepsilon_1 \frac{\partial\phi_0}{\partial r'}\bigg|_{r'=a} - \frac{\partial\phi_2}{\partial r'}\bigg|_{r'=a} = -\frac{\sigma_{\text{PE}}}{\varepsilon_0}, \tag{5.6d}$$

where ε_0 is the permittivity of the vacuum. Equation (5.6a) describes the vanishing potential far away from the PE-cylinder complex, Eqs. (5.6b) and (5.6c) are the conditions of continuous potential across the surfaces of both the PE and the cylinder, and Eq. (5.6d) is the jump condition for the electric displacement across

the boundary of the PE [14]. In addition to the above BCs, for the PE-dielectric complex, another BC is required, that is, the continuity of the electric displacement on the surface of the dielectric cylinder [14]

$$\varepsilon_2 \frac{\partial \phi_1^{\text{diel}}}{\partial r}\Big|_{r=r_0} = \varepsilon_1 \frac{\partial \phi_0^{\text{diel}}}{\partial r}\Big|_{r=r_0}. \tag{5.7}$$

Once the electric potential ϕ_0 is solved from the BVP defined above, the expression for the force $\mathbf{F}$ on the charged wall due to the PE-cylinder complex can be derived. First, the electric field $\mathbf{E}$ in the electrolyte solution can be evaluated by $\mathbf{E} = -\nabla\phi_0$, where ∇ is the gradient. Then $\mathbf{F}$ can be calculated using

$$\mathbf{F} = \int_A \sigma_{\text{S}} \mathbf{E}\Big|_{x=d_1} dA,$$

where A is the surface of the charged wall, and dA is an infinitesimal element on the surface. It is clear that the y component of the force cancels out due to symmetry, and the only contribution to the total force is in the x (horizontal) direction, which we denote as F_{x}. Therefore, the binding force per unit length on the charged wall can be found using

$$F_{\text{x}} = -2\int_0^\infty \sigma_{\text{S}} \frac{\partial \phi_0}{\partial x}\Big|_{x=d_1} dy. \tag{5.8}$$

Due to the presence of the electronically responsive cylinder, the electric potential on the surface of the PE is not uniform, which makes an exact analytical solution for the electric potential impossible to obtain [16]. However, because $a << r_0$, it is appropriate to assume that the potential is uniform on the surface of the PE and is equal to the value of the electric potential at one particular point ($\psi = 0,\ r = d - a$) [16] . As a result, continuity of the electric potential and jump condition of the electric displacement (Eqs. (5.6c) and (5.6d), respectively) are satisfied only at that point, leading to two modified BCs

$$\phi_0\Big|_{r'=a}^{\psi'=0} = \phi_2\Big|_{r'=a}^{\psi'=0}, \tag{5.9a}$$

$$\varepsilon_1 \frac{\partial \phi_0}{\partial r'}\Big|_{r'=a}^{\psi'=0} = -\frac{\sigma_{\text{PE}}}{\varepsilon_0}. \tag{5.9b}$$

The validity of such an approximation has been proven by calculating the maximum error caused by the modified BCs [16].

To summarize, the BVP for the PE-metallic complex is defined by Eqs. (5.2), (5.3), (5.4) and Eqs. (5.6a), (5.6b), (5.9a), (5.9b), and the BVP for the PE-dielectric complex is defined by Eqs. (5.2), (5.3), (5.5) and Eqs. (5.6a), (5.6b), (5.7), (5.9a), (5.9b). Following the solution of the BVP, the binding force is calculated using Eq. (5.8).

5.3 Binding force

In this section, the expressions for the binding force per unit length on the charged wall are derived for the PE-metallic cylinder and the PE-dielectric cylinder complexes. For the sake of simplicity, the following normalized variables are introduced

$$\bar{r} = kr,\ \bar{r}' = kr',\ \bar{x} = kx,\ \bar{y} = ky,\ \bar{a} = ka,\ \bar{r}_0 = kr_0,\ \bar{d} = kd,\ \bar{d}_1 = kd_1,$$
$$\bar{d}_2 = kd_2, \bar{l}_{\mathrm{B}} = kl_{\mathrm{B}},\ \bar{\phi} = -\frac{\varepsilon_0\varepsilon_1}{l_{\mathrm{B}}\sigma_{\mathrm{PE}}}\phi,\ \bar{\phi}_c = -\frac{\varepsilon_0\varepsilon_1}{l_{\mathrm{B}}\sigma_{\mathrm{PE}}}\phi_c,\ \bar{F}_{\mathrm{x}} = -\frac{\varepsilon_0\varepsilon_1}{l_{\mathrm{B}}\sigma_{\mathrm{PE}}\sigma_{\mathrm{s}}}F_{\mathrm{x}}. \quad (5.10)$$

Here l_{B} is the Bjerrum length [13] defined as the distance at which the electrostatic interaction between two elementary charges is comparable to the thermal energy $k_{\mathrm{B}}T$, where k_{B} is the Boltzmann constant, and T is the absolute temperature in Kelvins. At room temperature (300 K) and in water, the Bjerrum length is approximately 7Å. Note that in Eq. (5.10), a minus sign is introduced for the normalization of F_{x} because $\sigma_{\mathrm{S}}\sigma_{\mathrm{PE}} < 0$; the minus sign ensures that the normalized force $\bar{F}_{\mathrm{x}}$ has the same sign as F_{x}. In addition, in the remainder of this work, we will discuss the results based on the consideration of $\sigma_{\mathrm{PE}} < 0$, since we are motivated by a negatively charged PE (ssDNA). However, our results are not limited only to the case of $\sigma_{\mathrm{PE}} < 0$. Such consideration is only meant to facilitate our explanations on the physics of the results.

Solving the BVP with the above normalization, Eq. (5.10), the normalized electric potential in the region exterior to the PE-cylinder complex is obtained as [16]

$$\bar{\phi}_0 = \bar{C}\left[K_0(\bar{r}') - \sum_{n=0}^{\infty} \bar{f}_n \cos(n\psi) K_n(\bar{r})\right] \text{ in } D_0, \quad (5.11)$$

where $K_n(u)$ are the n-th order modified Bessel functions of the second kind [17]. $\bar{f}_n$ are coefficients in the series; their expressions are given later in the subsections.

$\bar{C}$ is a coefficient with different mathematical expressions depending on the nature of the responsive cylinder. Equation (5.11) describes the electric potential in D_0 for both the PE-metallic cylinder and the PE-dielectric cylinder complexes. A superscript "met" will be added to $\bar{f}_n$ and $\bar{C}$ when the PE-metallic cylinder complex is considered, and "diel" when the PE-dielectric cylinder complex is considered. They are presented in the following subsections. Using Eqs. (5.8) and (5.11), the expressions for the binding force per unit length between the PE-cylinder complex and the charged wall can be derived.

5.3.1 PE-metallic complex

In this subsection the expression for the binding force between the charged wall and the PE-metallic cylinder complex is calculated. The expressions for the coefficients $\bar{f}_n^{\text{met}}$ and $\bar{C}^{\text{met}}$ in Eq. (5.11) are the following [16]

$$\bar{f}_n^{\text{met}} = \begin{cases} \bar{f}_0^{\text{grmet}} - \frac{\bar{\phi}_c}{\bar{C}^{\text{met}} K_0(\bar{r}_0)}, & n = 0 \\ \frac{1}{\pi K_n(\bar{r}_0)} \int_0^{2\pi} K_0\left(\sqrt{\bar{r}_0^2 - 2\bar{r}_0\bar{d}\cos\psi + \bar{d}^2}\right)\cos(n\psi)d\psi, & n > 0, \end{cases} \tag{5.12}$$

$$\bar{C}^{\text{met}} = \frac{\frac{\bar{\phi}_c}{K_0(\bar{r}_0)} K_1(\bar{d} - \bar{a}) - \frac{1}{\bar{l}_{\text{B}}}}{K_1(\bar{a}) + \bar{f}_0^{\text{grmet}} K_1(\bar{d} - \bar{a}) + \frac{1}{2}\sum_{m=1}^{\infty} \bar{f}_m^{\text{met}} K_{m+1}(\bar{d} - \bar{a})}, \tag{5.13}$$

where $\bar{f}_0^{\text{grmet}} = \int_0^{2\pi} K_0\left(\sqrt{\bar{r}_0^2 - 2\bar{r}_0\bar{d}\cos\psi + \bar{d}^2}\right) / \left(2\pi K_0(\bar{r}_0)\right) d\psi$. $\bar{f}_0^{\text{met}} = \bar{f}_0^{\text{grmet}}$ when the metallic cylinder is grounded ($\bar{\phi}_c = 0$). Using Eqs. (5.1), (5.8), (5.10), and (5.11) the expression for the normalized binding force $\bar{F}_{\text{x}}^{\text{met}}$ per unit length takes the following form

$$\bar{F}_{\text{x}}^{\text{met}} = 2\bar{C}^{\text{met}} \int_0^{\infty} \left[\bar{d}_2 \frac{K_1\left(\sqrt{\bar{d}_2{}^2 + \bar{y}^2}\right)}{\sqrt{\bar{d}_2^2 + \bar{y}^2}} - \left(\bar{d}_2 + \bar{d}\right) \bar{f}_0^{\text{met}} \frac{K_1\left(\sqrt{\left(\bar{d}_2 + \bar{d}\right)^2 + \bar{y}^2}\right)}{\sqrt{\left(\bar{d}_2 + \bar{d}\right)^2 + \bar{y}^2}} \right.$$
$$\left. - \sum_{n=1}^{\infty} \bar{f}_n^{\text{met}} \frac{n\cos\left[(n+1)\,\beta\right] K_n\left(\sqrt{\left(\bar{d}_2 + \bar{d}\right)^2 + \bar{y}^2}\right)}{\sqrt{\left(\bar{d}_2 + \bar{d}\right)^2 + \bar{y}^2}} \right] d\bar{y}, \tag{5.14}$$

where $\beta = \psi(\bar{x} = \bar{d}_1) = \arctan\left(\bar{y}/\bar{d}_1\right)$.

5.3.2 PE-dielectric complex

Following the same procedure, the expression for the normalized electric potential due to the presence of the dielectric cylinder is given by Eq. (5.11) with coefficients $\bar{f}_n^{\text{diel}}$ and $\bar{C}^{\text{diel}}$ in the following form [16]

$$\bar{f}_n^{\text{diel}} = \begin{cases} \frac{1}{2\pi K_1(\bar{r}_0)} \int_0^{2\pi} \frac{\left[\bar{r}_0 - \bar{d}\cos(\psi)\right] K_1\left(\sqrt{\bar{r}_0^2 - 2\bar{r}_0\bar{d}\cos\psi + \bar{d}^2}\right)}{\sqrt{\bar{r}_0^2 - 2\bar{r}_0\bar{d}\cos\psi + \bar{d}^2}} d\psi, & n = 0 \\ \frac{n\varepsilon_{21}}{\pi n(1+\varepsilon_{21})K_n(\bar{r}_0)} \int_0^{2\pi} K_0\left(\sqrt{\bar{r}_0^2 - 2\bar{r}_0\bar{d}\cos\psi + \bar{d}^2}\right)\cos(n\psi)d\psi & \\ + \frac{\bar{r}_0}{\pi n(1+\varepsilon_{21})K_n(\bar{r}_0)} \int_0^{2\pi} \frac{\left[\bar{r}_0 - \bar{d}\cos(\psi)\right] K_1\left(\sqrt{\bar{r}_0^2 - 2\bar{r}_0\bar{d}\cos\psi + \bar{d}^2}\right)}{\sqrt{\bar{r}_0^2 - 2\bar{r}_0\bar{d}\cos\psi + \bar{d}^2}} \cos(n\psi)d\psi, & n > 0, \end{cases} \tag{5.15}$$

$$\bar{C}^{\text{diel}} = -\frac{1}{\bar{l}_{\text{B}}\left[K_1(\bar{a}) + \bar{f}_0^{\text{diel}}K_1(\bar{d}-\bar{a}) + \frac{1}{2}\sum_{m=1}^{\infty}\bar{f}_m^{\text{diel}}K_{m+1}(\bar{d}-\bar{a})\right]}. \tag{5.16}$$

Here $\varepsilon_{21} = \varepsilon_2/\varepsilon_1$ is the ratio of the dielectric constant of the dielectric cylinder to that of the electrolyte solution. The detailed derivation of the above expressions can be found in [16]. The normalized binding force $\bar{F}_{\text{x}}^{\text{diel}}$ per unit length in this case is given by

$$\bar{F}_{\text{x}}^{\text{diel}} = 2\bar{C}^{\text{diel}} \int_0^{\infty} \left[\bar{d}_2 \frac{K_1\left(\sqrt{\bar{d}_2{}^2 + \bar{y}^2}\right)}{\sqrt{\bar{d}_2^2 + \bar{y}^2}} - \left(\bar{d}_2 + \bar{d}\right) \bar{f}_0^{\text{diel}} \frac{K_1\left(\sqrt{\left(\bar{d}_2 + \bar{d}\right)^2 + \bar{y}^2}\right)}{\sqrt{\left(\bar{d}_2 + \bar{d}\right)^2 + \bar{y}^2}} \right.$$
$$\left. - \sum_{n=1}^{\infty} \bar{f}_n^{\text{diel}} \frac{n\cos\left[(n+1)\,\beta\right] K_n\left(\sqrt{\left(\bar{d}_2 + \bar{d}\right)^2 + \bar{y}^2}\right)}{\sqrt{\left(\bar{d}_2 + \bar{d}\right)^2 + \bar{y}^2}} \right] d\bar{y}. \tag{5.17}$$

5.4 Results

In this section, we provide the results for the normalized binding force $\bar{F}_{\text{x}}$ on the charged wall due to the PE-cylinder complex. As was mentioned earlier, the common range for the radius of the swCNT is $[3.5;\ 50]$ Å and we consider the radius a of the PE to be much smaller than r_0, in the range of 0.1 to 10 Å. The Debye length of the electrolyte solution is usually in the range of 0.1 nm to 100 nm. Therefore, the ranges for the following normalized quantities are $\bar{r}_0 \in 3.5 \times 10^{-3}$ to 50 and $\bar{a} \in$

10^{-4} to 10, respectively. The normalized distance $\bar{d}$ between the PE and the cylinder is taken to be $\bar{d} \geqslant 1.5\bar{r}_0$. The dielectric constant of the electrolyte solution is taken to be equal to that of water, that is, $\varepsilon_1 = 80$. Different values for the dielectric constant ε_2 of the dielectric cylinder are considered, such that the normalized ratio ε_{21} ranges from 0.1 to 100.

Figure 5.2 plots the normalized binding force $\bar{F}_{\rm x}$ versus the normalized separation distance $\bar{d}_2$ between the center of the PE and the charged wall for the following sets of parameters: $\bar{a} = 10^{-2}$, $\bar{r}_0 = 0.1$, $\bar{d} = 1.5\bar{r}_0$, and $\varepsilon_{21} = 0.1$. One of the curves (solid and labeled as "dielectric") corresponds to $\bar{F}_{\rm x}$ due to the PE near a neutral dielectric cylinder. The other curves correspond to $\bar{F}_{\rm x}$ due to the PE near a metallic cylinder with different electric potential $\bar{\phi}_c$. Positive values of $\bar{F}_{\rm x}$ (and positive value of $F_{\rm x}$) indicate that the force on the wall acts to the right (See Figure 5.1), away from the PE. This corresponds to repulsive force between the wall and the PE-cylinder complex. Similarly, negative values of $\bar{F}_{\rm x}$ mean that the force is attractive. At the same distance $\bar{d}_2$, the larger the magnitude of the negative force, the more attractive this force is. Similarly, the larger the positive force, the more repulsive it gets. For each curve on this figure, as the separation distance $\bar{d}_2$ increases, the magnitude of the normalized binding force decreases. As $\bar{d}_2$ approaches ∞, the charged wall and the PE-cylinder complex are infinitely far apart and there is no longer binding force between them.

Let us first compare $\bar{F}_{\rm x}$ due to a dielectric cylinder and that due to a grounded metallic cylinder ($\bar{\phi}_c = 0$). Clearly $\bar{F}_{\rm x}$ in both cases is attractive. However, the magnitude of $\bar{F}_{\rm x}$ due to the dielectric cylinder is larger than that due to the grounded metallic cylinder (See Figure 5.2). In fact, in the absence of the electronically responsive cylinder, the expressions for the electric potential $\bar{\phi}_0^{\rm PE}$ in D_0 [16] and the binding force $\bar{F}_{\rm x}^{\rm PE}$ on the charged wall are respectively given by

$$\bar{\phi}_0^{\rm PE} = -\frac{1}{\bar{l}_B}\frac{K_0(\bar{r}')}{K_1(\bar{a})} \text{ in } D_0, \tag{5.18}$$

$$\bar{F}_{\rm x}^{\rm PE} = -\frac{2\bar{d}_2}{\bar{l}_B K_1(\bar{a})}\int_0^\infty \frac{K_1(\sqrt{\bar{d}_2^2+\bar{y}^2})}{\sqrt{\bar{d}_2^2+\bar{y}^2}}d\bar{y}, \tag{5.19}$$

where superscript "PE" stands for the PE alone (no electronically responsive cylinder nearby). The normalization for $\bar{\phi}_0^{\rm PE}$ and $\bar{F}_{\rm x}^{\rm PE}$ is similar to the one introduced in

Eq. (5.10). Comparing calculation from Eq. (5.19) with those in Figure 5.2 shows that the magnitude of $\bar{F}_{\mathrm{x}}^{\mathrm{PE}}$ is smaller than that due to the PE-dielectric cylinder complex, and larger than that due to the PE-grounded metallic cylinder complex. This observation can be explained by the following. The negatively charged PE causes free charges on the surface of the metallic cylinder to redistribute themselves. These redistributed charges create an electric field that weakens the original field of the PE, which in turn results in smaller binding force. The dielectric cylinder considered here, however, has an opposite influence on the binding force because its dielectric constant ε_2 is less than that of the electrolyte solution ε_1. The dielectric constant measures the ability of a material to be polarized by an external field; it is a factor by which the external electric field is reduced. Introducing a dielectric cylinder with $\varepsilon_2 < \varepsilon_1$ near the PE effectively replaces the electrolyte with a material of smaller polarization, therefore strengthening the original field of the PE alone and increasing the binding force. In fact, metal can be considered as having a dielectric constant approaching ∞, that is, much larger than ε_1. This is consistent with the weakening effect addressed earlier.

If a non-grounded metallic cylinder is located near the PE, then $\bar{F}_{\mathrm{x}}$ can be attractive or repulsive depending on $\bar{\phi}_c$, as can be seen from Figure 5.2. Different values of $\bar{\phi}_c$ and its sign drastically influence the magnitude and the direction of $\bar{F}_{\mathrm{x}}$. The metallic cylinder has a positive or a negative potential when the net charge on the metallic cylinder is positive or negative, respectively [14]. The observed behavior of the force can be explained by the two effects of the non-grounded metallic cylinder: the screening effect due to charge redistribution and the effect of the net charge. For a grounded metallic cylinder only the screening effect plays a role, because the net charge is zero. For a positively charged metallic cylinder near the PE, $\bar{F}_{\mathrm{x}}$ is slightly attractive or repulsive depending on the magnitude of $\bar{\phi}_c$. This happens because at the location of the wall, the x component of the electric field due to the PE alone points towards the PE itself. The screening effect of the metallic cylinder weakens this field. In addition, the net positive charge on the metal introduces an electric field whose x-component points away from the PE at the wall. This further reduces the field of the PE and can even cause the binding force to be repulsive. The larger

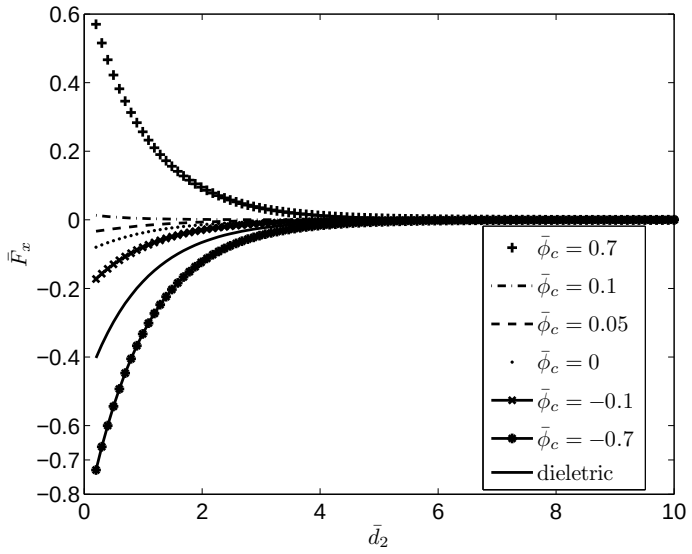

Figure 5.2: Normalized binding force $\bar{F}_x$ per unit length on the charged wall due to the PE near the metallic or the dielectric cylinder. The solid line represents the binding force between the PE-dielectric cylinder complex and the charged wall, and all the other curves are for the PE-metallic cylinder complex. Different values for $\bar{\phi}_c$ correspond to different electric potentials of the metallic cylinder for the PE-metallic cylinder complex. Here, $\bar{a} = 10^{-2}$, $\bar{r}_0 = 0.1, \varepsilon_{21} = 0.1$ and $\bar{d} = 1.5\bar{r}_0$.

the magnitude of $\bar{\phi}_c$, the more repulsive the force on the charged wall. On the other hand, due to the presence of a negatively charged metallic cylinder, $\bar{F}_{\mathrm{x}}$ is always attractive, and the strength of attraction increases with the magnitude of $\bar{\phi}_c$. This occurs because although the screening effect of the metal weakens the electric field of the PE, the net negative charges strengthen it. The overall result is $\bar{F}_{\mathrm{x}}$ being more attractive than the case of a grounded metallic cylinder. The larger the magnitude of $\bar{\phi}_c$, the stronger the attraction becomes. For $\bar{\phi}_c = -0.7$, $\bar{F}_{\mathrm{x}}$ is even more attractive than the force in the case of a dielectric cylinder. This manifests the dominance of the effect of the net charge on the metallic cylinder.

Figure 5.3 plots $\bar{F}_{\mathrm{x}}$ versus $\bar{d}_2$ for $\bar{d} = 5\bar{r}_0,\ \bar{a} = 10^{-2},\ \bar{r}_0 = 0.1$, and $\varepsilon_{21} = 0.1$, that is, the separation distance between the PE and the cylinder has been increased. As in the previous figure, one curve corresponds to the normalized force due to the PE near the dielectric cylinder and the other curves correspond to cases of metallic cylinders with different values of $\bar{\phi}_c$. By comparing Figures 5.2 and 5.3, we can see

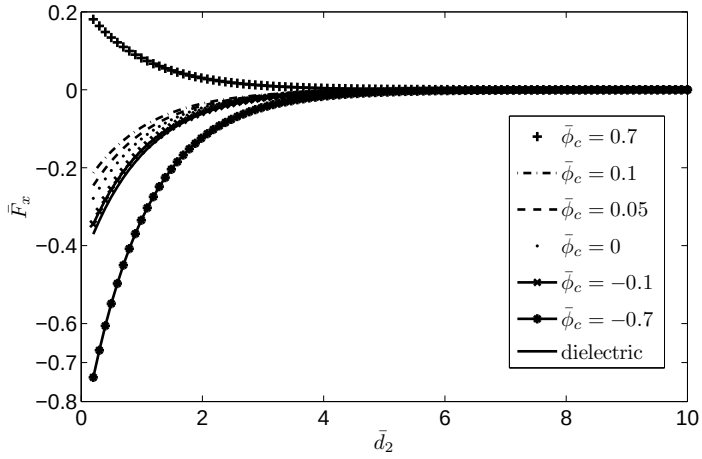

Figure 5.3: Normalized binding force $\bar{F}_x$ per unit length on the charged wall due to the PE-metallic cylinder or the PE-dielectric cylinder complexes. The solid line represents the binding force between the PE-dielectric complex and the charged wall, and all the other curves are for the PE-metallic cylinder complex. Different values for $\bar{\phi}_c$ correspond to different electric potentials of the metallic cylinder for the PE-metallic cylinder complex. Here, $\bar{a} = 10^{-2}$, $\bar{r}_0 = 0.1, \varepsilon_{21} = 0.1$, and $\bar{d} = 5\bar{r}_0$.

that by moderately increasing the separation distance between the PE and the cylinder (from $\bar{d} = 1.5\bar{r}_0$ to $\bar{d} = 5\bar{r}_0$), the binding force can change its magnitude as well as direction. Specifically, for the dielectric cylinder, as $\bar{d}$ increases, the curve shifts upwards, that is, the magnitude of $\bar{F}_{\mathrm{x}}$ reduces, indicating that the binding force is less attractive. This is expected since as $\bar{d}$ increases, the influence of the dielectric cylinder, strengthening the electric field of the PE, becomes smaller. For the metallic cylinder, as $\bar{d}$ increases from $\bar{d} = 1.5\bar{r}_0$ to $\bar{d} = 5\bar{r}_0$, the curves shift downwards, which corresponds to increased attraction (See $\bar{\phi}_c = -0.7, -0.1, 0, 0.05$), reduced repulsion (See $\bar{\phi}_c = 0.7$), or changing from repulsion to attraction (See $\bar{\phi}_c = 0.1$). Interestingly, however, as $\bar{d}$ is further increased, different change in $\bar{F}_{\mathrm{x}}$ is observed for positively and negatively charged metallic cylinders. This is discussed with the next two figures.

Each subplot in Figures 5.4 and 5.5 shows $\bar{F}_{\mathrm{x}}$ versus $\bar{d}_2$ due to the PE-metallic cylinder complex with a given $\bar{\phi}_c$ but with different values of $\bar{d}$. For these plots, we have taken $\bar{a} = 10^{-2}, \bar{r}_0 = 0.1$, and $\varepsilon_{21} = 0.1$. In Figure 5.4a, the electric potential on the metallic cylinder is chosen to be $\bar{\phi}_c = 0.7$; whereas $\bar{\phi}_c = -0.7$ is

used in Figure 5.4b. Figure 5.5 corresponds to metallic cylinder of much less net charge, with $\bar{\phi}_c = 0.1$ in Figure 5.5a and $\bar{\phi}_c = -0.1$ in Figure 5.5b. It is expected as $\bar{d} \to \infty$, the different curves shown in each figure converge to a single one that is associated with the binding force $\bar{F}_{\text{x}}^{\text{PE}}$ on the charged wall due to the PE alone, given by Eq. (5.19). Therefore, we also plot $\bar{F}_{\text{x}}^{\text{PE}}$ and it is labeled as "PE". As can be seen from Figures 5.4a and 5.5a, when a positively charged metallic cylinder is present, as $\bar{d}$ increases, the binding force first changes from repulsive to attractive. This happens because with $\bar{d}$ increasing, the influence of the net positive charge and the screening effect of the metal, both weakening the electric field of the PE, reduces. As $\bar{d}$ further increases, the binding force approaches from above to that of the PE alone, which shows that both effects diminish their influence. For the PE near a negatively charged metallic cylinder, from Figures 5.4b and 5.5b, it is seen that as $\bar{d}$ increases, the binding force first becomes more attractive. However, as $\bar{d}$ increases further, $\bar{F}_{\text{x}}$ becomes less attractive, and approaches from below to that of the PE alone. That is, $\bar{F}_{\text{x}}$ exhibits non-monotonic variation with $\bar{d}$. As mentioned earlier, the negative charge on the cylinder strengthens the electric field of the PE and compete with the screening from the metal. Take Figure 5.5b for example. At small separation (e.g., $\bar{d} = 1.5\bar{r}_0$), $\bar{F}_{\text{x}}$ is less attractive than that of the PE alone, indicating that the screening effect is more significant than the effect of the net charge. As $\bar{d}$ increases (from $\bar{d} = 1.5\bar{r}_0$ to $\bar{d} = 5\bar{r}_0$), the binding force becomes more attractive, and the curve approaches that of the PE alone. By increasing $\bar{d}$ further (from $\bar{d} = 5\bar{r}_0$ to $\bar{d} = 11.5\bar{r}_0$), $\bar{F}_{\text{x}}$ becomes slightly more attractive than that of the PE alone. This is an indication that at such a separation, the net negative charge has become the dominant effect.

To further explain the above observations, Figure 5.6 shows $\bar{F}_{\text{x}}$ versus $\bar{d}$ due to the PE near a grounded or a negatively charged metallic cylinder, calculated at a particular distance $\bar{d}_2 = 2\bar{r}_0$ between the PE and the wall. Different curves on this plot correspond to the binding force with different values of the electric potential $\bar{\phi}_c$. All the curves exhibit an initial increase in attraction with increasing $\bar{d}$. Since the two competing effects of a negatively charged metallic cylinder (screening and net charge) both decrease with increasing $\bar{d}$, the initial increase in attraction im-

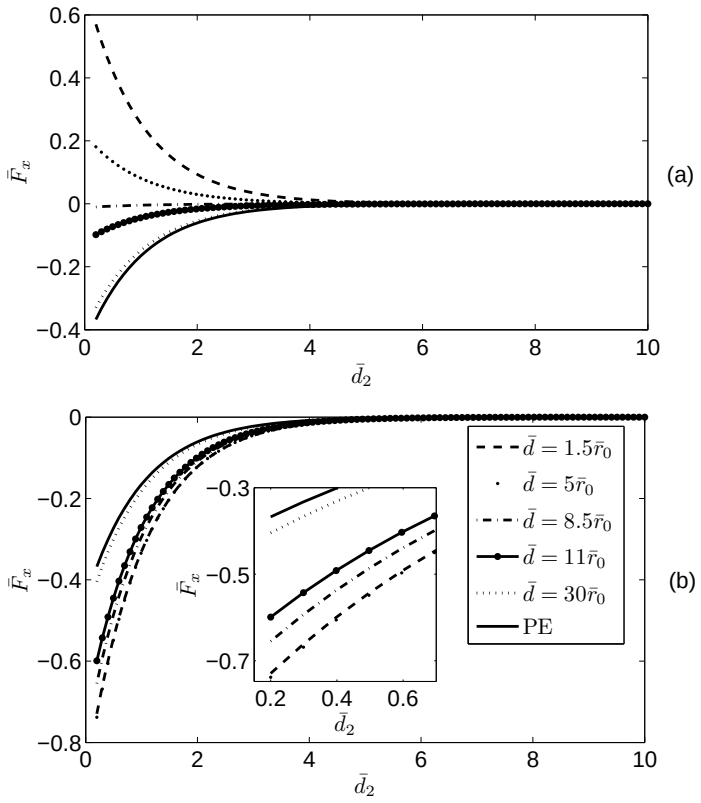

Figure 5.4: Normalized binding force $\bar{F}_x$ per unit length on the charged wall due to the PE-metallic cylinder complex or the PE alone (i.e. without the presence of the responsive cylinder). The metallic cylinder with a particular $\bar{\phi}_c$ is considered: a) $\bar{\phi}_c = 0.7$ and b) $\bar{\phi}_c = -0.7$. The solid line represents the binding force between the charged wall and the PE alone, and the rest are for the PE-metallic cylinder complex with the same specified $\bar{\phi}_c$ but different separation distances $\bar{d}$ between the metallic cylinder and the PE. Here, $\bar{a} = 10^{-2}$, $\bar{r}_0 = 0.1$, and $\varepsilon_{21} = 0.1$. The legends are the same for the top and the bottom figures.

plies that the screening effect decays faster at short range. For some curves (e.g. $\bar{\phi}_c = -0.5$), $\bar{F}_{\mathrm{x}}$ reaches a minimum (maximum attraction) at a certain distance $\bar{d}$. Afterwards, the attraction decreases, indicating that the effect of the net charge, which is strengthening the electric field, decays faster at long range. The competition between these two effects is the reason for the observed non-monotonic behavior in Figures 5.4b and 5.5b. As the value of the electric potential $\bar{\phi}_c$ approaches zero, the observed minimum in $\bar{F}_{\mathrm{x}}$ vanishes. This is expected because for the grounded metallic cylinder, screening is the only effect on the electric field of

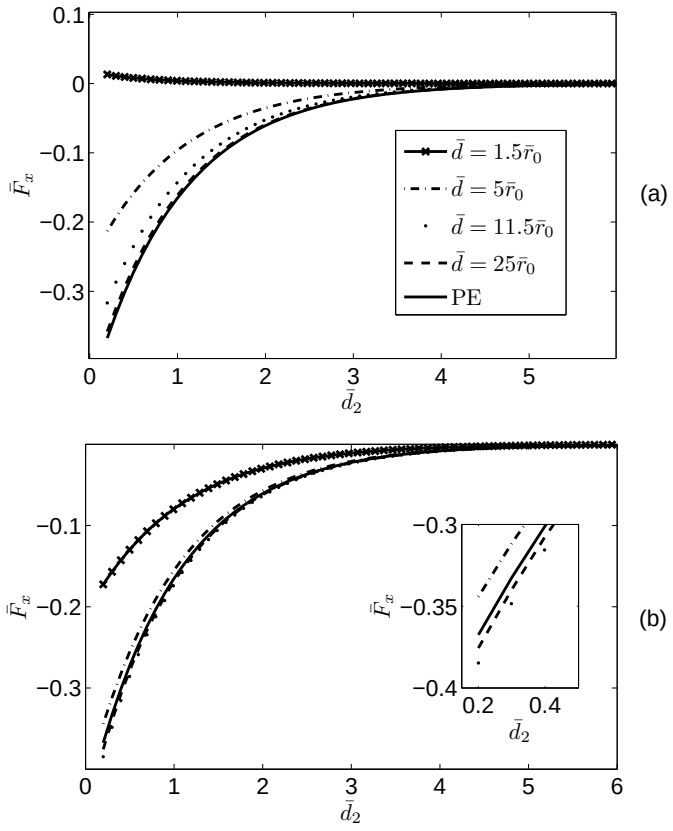

Figure 5.5: Normalized binding force $\bar{F}_x$ per unit length on the charged wall due to the PE-metallic cylinder complex or the PE alone (i.e. without the presence of the responsive cylinder). The metallic cylinder with a particular $\bar{\phi}_c$ is considered: a) $\bar{\phi}_c = 0.1$ and b) $\bar{\phi}_c = -0.1$. The solid line represents the binding force between the charged wall and the PE alone, and the rest are for the PE-metallic cylinder complex with the same specified $\bar{\phi}_c$ but different separation distances $\bar{d}$ between the metallic cylinder and the PE. Here, $\bar{a} = 10^{-2}$, $\bar{r}_0 = 0.1$, and $\varepsilon_{21} = 0.1$. The legends are the same for the top and the bottom figures.

the PE.

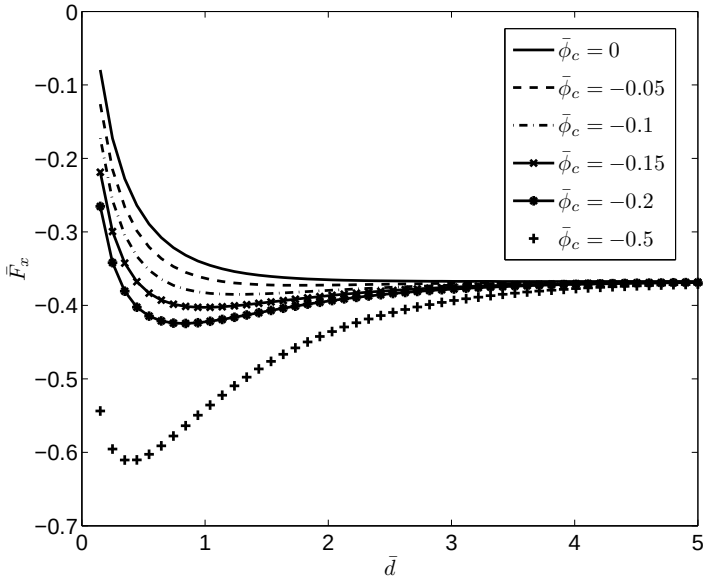

Figure 5.6: Normalized binding force $\bar{F}_x$ on the charged wall due to the PE near a grounded or a negatively charged metallic cylinder versus the separation distance $\bar{d}$ between the PE and the metallic cylinder. This force is calculated at the distance $\bar{d}_2 = 2\bar{r}_0$ from the center of the PE to the wall. Different curves correspond to different values of the electric potential $\bar{\phi}_c$ on the surface of the metallic cylinder. Here, $\bar{a} = 10^{-2}$, $\bar{r}_0 = 0.1$, and $\varepsilon_{21} = 0.1$.

Figure 5.7 shows $\bar{F}_{\rm x}$ versus $\bar{d}_2$ for the PE-dielectric cylinder complex with different dielectric constant ratio ε_{21}. Also shown is $\bar{F}_{\rm x}^{\rm PE}$ due to PE alone. As can be seen from Figure 5.7 and its insert, as ε_{21} increases, the magnitude of the binding force decreases. This is expected since larger ε_2 implies stronger polarization inside the dielectric cylinder, and therefore weaker electrostatic interaction. As mentioned earlier, the dielectric cylinder effectively replaces part of the electrolyte solution. As a result, $\bar{F}_{\rm x}$ due to the dielectric cylinder with $\varepsilon_2 < \varepsilon_1$ is more attractive than $\bar{F}_{\rm x}^{\rm PE}$. Whereas, $\bar{F}_{\rm x}$ due to the dielectric cylinder with $\varepsilon_2 > \varepsilon_1$ is less attractive than $\bar{F}_{\rm x}^{\rm PE}$. Nevertheless, the dielectric constant does not seem to have a strong impact on the binding force.

To summarize, in this paper, we derive the expressions for the binding force between a PE-cylinder complex and an oppositely charged wall. Our results show that the binding force due to the PE-metallic cylinder complex is different from that

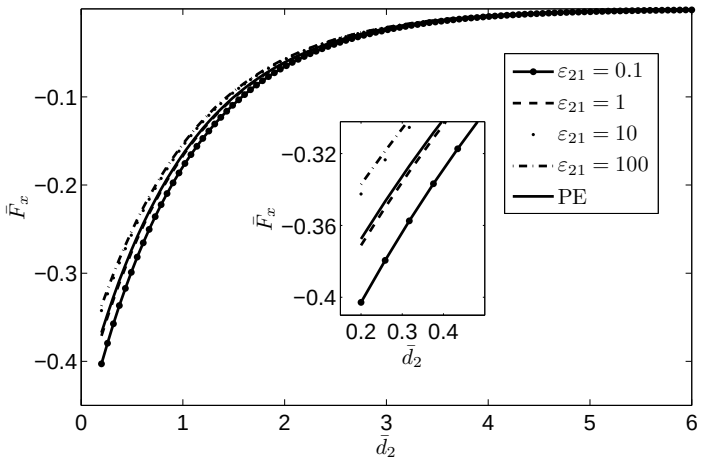

Figure 5.7: Normalized binding force $\bar{F}_x$ per unit length on the charged wall due to the PE-dielectric cylinder complex or the PE alone. The solid line represents the binding force between the charged wall and the PE alone, and all the others curves correspond to the PE-dielectric cylinder complex with different ratios of dielectric constants ε_{21}. Here, $\bar{a} = 10^{-2}$, $\bar{r}_0 = 0.1$ and $\bar{d} = 1.5\bar{r}_0$.

due to the PE-dielectric cylinder complex. This difference depends on the value of the electric potential on the metallic cylinder. For the PE-grounded metallic cylinder complex the binding force is weaker than that between the PE-dielectric cylinder complex and the charged wall. For the PE-positively charged metallic cylinder complex, the binding force is less attractive or even repulsive compared with the PE-grounded cylinder complex. For the PE-negatively charged metallic cylinder, the binding force can be less or more attractive compared with the PE-dielectric cylinder complex, depending on the magnitude of the net negative charge. This is due to the two competing effects on the electric field of the PE: weakening from the metal and strengthening from the net negative charge. The separation between the PE and the cylinder also has a strong impact on the binding force. Specifically, as the cylinder is moved away from the PE, both the effects of screening and net charge decay, but weakening decays faster at short range; whereas, the effect of the net charge decays faster at long range.

5.5 Discussions

To discuss our results in connection with experiments, we note that during IEC [8, 9], the CNT-DNA hybrids associated with metallic CNTs elute from the charged column before those associated with semiconducting CNTs. This indicates that at the same salt concentration, the force between the metallic CNT-DNA hybrids and the column is weaker. Our calculations also show that the existence of a grounded metallic cylinder weakens the electric field of the PE and results in a smaller binding force compared with the case of a neutral dielectric cylinder. Of course, in the experiments, the CNT-DNA hybrids are suspended in a solution and the CNT may in fact carry a certain amount of charge [18]. Our results show that the binding force for a negatively charged metallic cylinder can be significantly larger. The fact that the metallic CNT-DNA hybrids elute first in the IEC seems to indicate that the metallic tubes in these experiments [8, 9] at least do not carry much stronger negative charges compared with the semiconducting tubes. We recognize that there are some differences between the model presented here and the hybrids in the experiments. For example, we have used a dielectric cylinder instead of a semiconductor. And we have used a simpler geometry in order to obtain analytical expressions for the binding force. However, with these simplifications, it is encouraging to see that the results qualitatively agree with experiments.

To review the procedure of calculating the binding force in this work, we first calculated the electric field of the PE-cylinder complex. This electric field is evaluated at the location of the charged wall and the force is calculated by multiplying the field with the surface charge density and integrating the result over the wall. Such an approach implicitly assumes that the charged wall does not alter the electric field of the complex. In addition, self interaction due to the charges on the wall is not included. The charged wall is brought in only to measure the force due to the PE-cylinder complex. In other words, by calculating the force, we are essentially addressing the strength of the electric field due to the PE-cylinder complex and how it is affected by the electronic nature of the cylinder. The above procedure is often used when calculating force/energy between charged entities [10, 19].

The response of the wall can be included by adding to the boundary value problem another equation governing the electric potential inside the wall and appropriate boundary conditions across the wall. But because in this work, we focus on how the responsive cylinder affects the electric field of the PE, we have neglected this effect.

In this paper, we use a simplified geometry for the PE-cylinder complex near the charged wall. This simplification has allowed us to obtain an analytical expression for the binding force between the PE-cylinder system and the wall, which in turn has facilitated the demonstration that the binding force strongly depends on the nature of the responsive cylinder. A better representation of the DNA-CNT hybrid would be a helix of charges wrapped around the CNT, which would prohibit an analytical solution. Finite element simulation on this problem is being conducted and the results will be reported elsewhere.

Usually when a highly charged particle is embedded in an electrolyte solution, the oppositely charged ions are attracted to the vicinity of this particle, effectively reducing its charge. This phenomenon is known as counterion condensation (CC) [11]. Manning developed a comprehensive theory of counterion condensation [20], which is widely used in modeling the electric field of charged molecules located in an electrolyte solution. In his theory, the entropic energy required to move counterions to the particle has a term that is singular in concentration in the dilute limit [20]. The behavior of the electrostatic energy in the dilute limit determines the amount of CC θ. In our present work, we do not consider CC, since we expect that counterion release (partial if not total) occurs when the PE-cylinder complex approaches the oppositely charged wall. Counterion release is a phenomenon that occurs when two oppositely charged particles embedded in an electrolyte solution approach each other [21–23]. At the distance at which the electric fields of the two oppositely charged particles start penetrating each other, counterions leave the vicinity of the charged particles and counterion release occurs. By considering CC on two lines of discrete charges of opposite sign and using the result reported by Ray and Manning [24], we found that there is no CC when the distance between the two lines is smaller than the Debye length. Quite recently, the first direct ex-

perimental evidence of counterion release was shown by Harries *et al.* [21]. These authors by measuring the conductivity of the solution demonstrated counterion release on the complex of cationic lipid and DNA. Note also that in [10], the binding free energy of CNT-DNA hybrid to a positively charged column does not include the effect of CC.

To incorporate possible CC in our work, we have tried to rigourously apply Manning's theory of CC by obtaining an analytical solution for the electrostatic energy with contributions from both charges σ_S and σ_{PE} in D_0. However, applying the BCs led to a system of equations with infinite dimension for the unknown coefficients in the expression of the electric potential, which cannot be solved without making further approximations. Another option for incorporating CC is to perform numerical simulations to calculate the electrostatic energy at different salt concentrations. The amount of CC θ can be found by studying the behavior of the electrostatic energy in the dilute limit. This is not trivial, because simulations on a dilute solution require a very large system, which is computationally expensive. This is out of the scope of this work. Finally, we mention that we have only considered a neutral dielectric cylinder in this work. The case of a charged dielectric cylinder can be studied by modifying the field equation inside the dielectric and the BC on its surface. We believe it is an interesting problem but leave it to a future work.

Bibliography

[1] Bianco, A., Kostarelos, K., Prato, M., *Curr. Opin. Chem. Biol.* **9(6)**, 674–679 (2005).

[2] Tang, T., Jagota, A., *J. Comput. Theor. Nanosci.* **5**, 1–8 (2008).

[3] Guo, J., Lundstrom, M., and Datta, S., *Appl. Phys. Lett.* **80(17)**, 3192–3194 (2002).

[4] Saito, R., Dresselhaus, G., and Dresselhaus, M.S., Physical Properties of Carbon Nanotubes, Imperial College Press, London (1998).

[5] Chen, Z., Du, X., Du, M.-H., Rancken, C.D., Cheng, H.-P., Rinzler, A.G., *Nano Lett.* **3(9)**, 1245–1249 (2003).

[6] Krupke, R., Hennrich, F., Löhneysen, H.V., Kappes, M., *Science* **301**, 344–347 (2003).

[7] Arnold, M.S, Green, A.A., Hulvat, J.F., Stupp, S.I., Hersam, M.C., *Nat.Nanotechnol.* **1**, 60–65 (2006).

[8] Zheng, M., Jagota, A., Semke, E.D., Diner, B.A., McLean, R.S., Lustig, S.R., Richardson, R.E., Tassi, N.G., *Nat. Mater.* **2**, 338–342 (2003).

[9] Zheng, M., Jagota, A., Strano, M.S., Santos, A.P., Barone, P., Chou, S.G., Diner, B.A., Dresselhaus, M.S., McLean, R.S., Onoa, G.B., Samsonidze, G.G., Semke, E.D., Usrey, M., Walls, D.J., *Science* **302**, 1545–1548 (2003).

[10] Lustig, S.R., Jagota, A., Khripin, C., *J. Phys. Chem. B* **109(7)**, 2559–2566 (2005).

[11] Israelachvili, J. N., Intermolelucar and Surface Forces, 2nd ed., Academic Press: London (1992).

[12] Stigter D., *Biophys. J.* **69**, 380–388 (1995).

[13] Russel, W.B., Saville, D.A., Schowalter, W.R., Colloidal Dispersions, Cambridge Univ. Press, Cambridge, UK (1989).

[14] Jackson, J. D., Classical Electrodynamics, 3rd ed.; Wiley: New York (1999).

[15] Landau, L.D. and Lifshitz, E.M., Electrodynamics of continuous media, Pergamon Press, New York (1984).

[16] Malysheva, O., Tang, T., Schiavone, P., *J. Phys. Chem. C* **114(9)**, 3781–3790 (2010).

[17] Abramovitz, M., Stegun, I.A. Handbook of Mathematical Functions. Dover, New-York (1965).

[18] Moonoosawmy, K. R. and Kruse, P., *J. Am. Chem. Soc.* **132**, 1572–1577 (2010).

[19] Manning, G.S., *J. Phys. Chem. B* **111**, 8554–8559 (2007).

[20] Manning, G.S., *J. Chem. Phys.* **51**, 924–933 (1969).

[21] Wagner, K., Harries, D., May S., Kahl V., Radler J.O., Ben-Shaul A., *Langmuir* **16**, 303–306 (2000).

[22] Sens, P., Joanny, J.-F., *Phys. Rev. Lett.* **84(21)**, 4862–4865 (2000).

[23] Meier-Koll, A.A., Fleck, C.C., von Grunberg, H.H., *J. Phys. Condens. Matter* **16(34)**, 6041–6052 (2004).

[24] Ray, J., Manning, G. S., *Langmuir* **10**, 2450–2461 (1994).

Chapter 6
A model for CNT-DNA Hybrid using One Dimensional Density of States[1]

6.1 Introduction

Carbon nanotubes (CNTs) are a novel nano-material with a number of exceptional electronic, mechanical, and thermal properties [1, 2]. Depending on their chirality CNTs have different structures and electronic properties [1, 2], and can be categorized into metallic or semiconducting tubes. CNTs exhibit interesting structure and behavior when hybridized with single-stranded DNA (ssDNA) molecules [3]. In the experiments conducted by Zheng *et al*. it was found that ssDNA molecules can wrap around CNTs and form CNT-DNA hybrids, allowing the dispersion of poorly soluble CNT bundles in an electrolyte solution [3, 4]. Utilizing the method of ion exchange chromatography (IEC), the dispersed CNT-DNA hybrids can be separated according to the chirality of the CNT core. Specifically, it was first observed in experiments that, as the salt concentration of the solution increased [3], metallic CNT-DNA hybrids eluted earlier from the column than semiconducting CNT-DNA hybrids. In subsequent work by the same authors, specific DNA sequences have been identified that are able to separate twelve semiconducting CNTs according to their chiralities [5].

To understand the experimental observations by studying the interaction between CNT and DNA as well was the properties of the CNT-DNA hybrids, models at different scales have been developed, including quantum mechanics calculations [6–8], molecular dynamics (MD) [4, 9, 10] and continuum modeling [11, 12]. Rotkin et al. studied the electronic structure of the CNT-DNA hybrid in vacuum [6, 7] using semiempirical tight binding modeling. Specifically, they considered Poly(T) helically wrapped around the (7,0) CNT. The polarization component of

[1] A version of this chapter is in preparation for publication.

the cohesion energy of the CNT-DNA hybrid was calculated [7]. Their results confirmed that the CNT-DNA hybrids were highly stable. Enyashin *et al.* studied the stability and electronic structure of CNT-DNA hybrids using density-functional tight-binding method [8]. Also in vacuum, the equilibrium configurations of CNT-Poly(T) hybrids were determined in the molecular simulations of Zheng *et al.* via energy minimization [3]. It was found that Poly(T) ssDNA could take several configurations around CNT, one of which was a helical wrapping, consistent with images from atomic force microscopy (AFM) [4]. The above analysis are all conducted in the absence of an aqueous solution. This can be an important factor because in the experiments of Zheng *et al.*, dispersion of the CNT-DNA hybrids occurred in a dilute electrolyte solution, and their separation was achieved by gradually increasing the salt concentration. Using scaling analysis coupled with molecular dynamics (MD) simulations in an aqueous solution, Manohar *et al.* [9] discussed the important interactions contributing to the hybrid formation. In a dilute solution, two main contributions were identified: 1) electrostatic interaction between DNA charges and CNT; and 2) adhesion between DNA and CNT. Subsequent MD simulations were performed by Johnson *et al.* [10] in an aqueous environment, where possible configurations of the CNT-DNA hybrids, the process of self-assembly of the hybrids, and energetics of the hybrids were studied. The major benefit of MD simulations is that they give valuable insights into the molecular details and dynamics of the hybrids. However, these simulations remain computationally expensive, allowing systems of up to 1.000.000 atoms to be simulated for up to a few microseconds [10, 13]. More importantly, classical MD simulations rely on the molecular mechanics force field, and a force field that can truly reflect the electronic response of the CNTs is not yet available. In the aforementioned MD works, the CNT atoms are modeled as uncharged particles that interact with DNA, water and ions only through the Lennard-Jones potential [14]. In other words, in these simulations, CNTs of different chiralities only differ in structure, but not in their electronic properties. There have also been attempts to model the CNT-DNA hybrids at the continuum level. Lustig *et al.* proposed an analytical model to describe the IEC process for the CNT-DNA hybrids in electrolyte solution [11]. In their work, the

electrolyte solution was modeled as a continuum medium using the Debye-Hückel (DH) equation, the DNA was modeled as a helical line of discrete charges, the CNT was modeled locally as a half-space, and its electronic property was represented as either a metal or a dielectric. The elution model of the CNT-DNA hybrids in IEC was developed by considering the free energy difference between the CNT-DNA hybrid bound to the IEC column and the free hybrid in the bulk solution. Their model predicted that for a given hybrid dimension, with increasing salt concentration of the electrolyte solution, the metallic CNT-DNA hybrids would elute earlier from the column than the semiconducting ones. This is in agreement with the original experiments [3, 4]. It should be noted that in this analytical model, several assumptions were made in order to simplify the analysis. First, the CNT was modeled locally as a half space, that is, its curvature was neglected. Second , the CNT was modeled as a solid metal or dielectric. Finally, the electronic response of the metal or dielectric was incorporated using the method of image charge [15], which is approximate. Malysheva *et al.* [12], in an attempt to evaluate how the attraction of the CNT-DNA hybrid to the IEC column depends on the nature of the CNT core, calculated the binding force between a charged wall and a complex consisting of a polyelectrolyte (PE) and a metallic or dielectric cylinder. The helical wrapping was simplified, whereas the governing equations for the electric potential in the solution and in the interiors of the PE and the cylinder were formulated exactly, in addition to accurate conditions across the domain boundaries. The results were in part consistent with previous predictions in that the binding force associated with the PE near a grounded metallic cylinder was found to be weaker than that associated with the PE near a neutral dielectric cylinder. This trend, however, could be different if the metallic cylinder was not grounded. In this work the CNT's response was again greatly simplified and approximated by a solid metal or dielectric.

The previous works revealed several important elements in modeling the electrostatics of the CNT-DNA hybrids: the charges on the DNA, the electrolyte environment and the electronic response of the CNT. Each of the previous works have captured some of the key elements but none has incorporated all of them. The quantum mechanical calculations properly considered the DNA charges and the

electronic response of the CNT, but neglected the electrolyte solution surrounding the hybrid. The MD simulations included the DNA charges and electrolyte solution, but the CNT's response was absent from the force field. The continuum models often simplified the CNT into solid metal or dielectric. In this work, we attempt to integrate these elements into a single theoretical frame at the continuum level. We propose a model system to represent a CNT-DNA hybrid located in an electrolytic environment. The electronic response of CNT to DNA charges is incorporated using the density of state (DOS) proposed by Mintmire *et al.* [16]. This DOS can be explicitly expressed in terms of the chirality of the CNT, and therefore can be readily integrated into the continuum electrolyte theory. There are two main purposes of this work. First, as an attempt to include all the elements crucial to the electrostatics of the hybrid, we want to examine whether this model is able to capture the experimentally observed difference between hybrids with different CNT cores. Second, it is known that the DOS model [16] has its limitations; hence it is desirable to see if it is applicable to the CNT-DNA hybrid system considered here.

The paper is organized as follows. In Section 6.2, we describe the model system and chosen mathematical approach. The boundary value problem (BVP) for the electric potential is defined in Section 6.3. The results and discussions are given in Section 6.4. Finally, conclusions are presented in Section 6.5.

6.2 Problem description

The model under consideration consists of a CNT which is wrapped by a DNA molecule and the hybrid is embedded in an electrolyte solution. The CNT is modeled as a cylindrical surface of radius r_{CNT}. In an electrolyte solution, the backbone of a DNA molecule becomes negatively charged due to deprotonation, and the negatively charged DNA wraps around CNT in helical fashion [3]. In this work, the helical wrapping of the DNA is simplified by smearing out the DNA charges onto a cylindrical surface of radius $r_{DNA} > r_{CNT}$, which is adopted from the standard primitive model for a polyelectrolyte [17, 18]. The uniform surface charge density on the cylindrical surface representing DNA is denoted as σ_{DNA}, such that

$\sigma_{DNA} < 0$. σ_{DNA} depends on the wrapping angle of DNA around CNT. The effective range for σ_{DNA} is estimated in Subsection 6.4.2. The two cylinders, representing CNT and DNA, are aligned so that their axes coincide. In addition, both cylinders are assumed to be very long along their axes, so that the problem is essentially two-dimensional, as shown in Figure 6.1. The CNT is assumed to be uncharged before the introduction of DNA. In the presence of charged DNA, its electric field can induce positive charges on the surface of the CNT [19]. The induced charge on the CNT surface is denoted by σ_{CNT}, such that, $\sigma_{DNA}\sigma_{CNT} < 0$. Due to the proposed geometry for the CNT-DNA hybrid, σ_{CNT} is uniform along the circumference of the CNT (there is no dependency on the polar angle), and it has a constant value along the axis of the CNT. This means that the surface charge density on the CNT is one dimensional (1D). Here, r is used to denote the polar radius. This geometry allows one to calculate the induced charge using the 1D DOS proposed by Mintmire *et al.* [16], which has been widely used in calculating charge generation on CNT [20, 21]. The exterior region to the CNT-DNA hybrid, denoted by D_0, is occupied

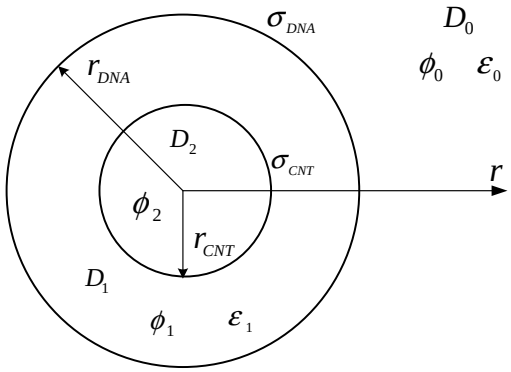

Figure 6.1: Geometry of the model CNT-DNA system. r is the polar radius, r_{CNT} and r_{DNA} are radii of the CNT and the DNA, respectively. D_2 is the interior region of the DNA, where electric potential ϕ_2 is defined. D_1 is the region between the two cylindrical surfaces, with the electric potential ϕ_1 and dielectric constant ε_1. D_0 is the exterior region to the hybrid, with ϕ_0 and ε_0.

by an electrolyte solution with dielectric constant ε_0 and the Debye length $1/k$ [22]. The space between the DNA and the CNT, D_1, is assumed to be free of charges and has the dielectric constant ε_1. The region D_1 will be referred to hereafter as the ring.

From MD simulations [9], it is found that a few water molecules are between the DNA and the CNT. Therefore, it is not known exactly what value for the dielectric constant ε_1 should be taken in the region between the DNA and the CNT. In this work, two limiting cases for ε_1 are considered, that is, $\varepsilon_1 = 1$ corresponding to a region occupied by vacuum (no water molecules in D_1) and $\varepsilon_1 = 80$ corresponding to a region fully occupied by water. The interior of the CNT D_2 is occupied by a vacuum, which is a reasonable assumption for a pristine, unoxidized CNT in an aqueous solution [10]. The electric potential in D_0 is denoted as ϕ_0, in D_1 as ϕ_1, and in D_2 as ϕ_2. In Section 6.3, the BVP for the electric potential in all regions is established. Consequently, we solve for the electric potential in all regions. Specifically, we are interested in ϕ_0 and how it changes with the electronic response of the CNT, because it determines the interaction strength between the hybrid and an object in its exterior region (that is, the IEC column).

6.3 BVP for the electric potential

The governing equation for the electric potential ϕ_0 in an electrolyte solution is given by the Debye-Hückel (DH) equation [22]

$$\nabla^2\phi_0 = k^2\phi_0 \text{ in } D_0, \tag{6.1}$$

where ∇^2 is the Laplacian, and k is the inverse Debye length. The Debye length $1/k$ of an electrolyte solution scales with its salt concentration c as $1/k \propto 1/\sqrt{c}$ [22]. That is, as the salt concentration increases, the Debye length decreases. Since there are no free charges in D_1 and D_2, the electric potential in these regions satisfies the Laplace equation [15]

$$\nabla^2\phi_i = 0 \text{ in } D_i,\ i = 1, 2. \tag{6.2}$$

The boundary conditions (BCs) are the following:

$$\lim_{r\to\infty} \phi_0 = 0, \tag{6.3a}$$

$$\phi_1|_{r=r_{CNT}} = \phi_2|_{r=r_{CNT}}, \tag{6.3b}$$

$$\phi_0|_{r=r_{DNA}} = \phi_1|_{r=r_{DNA}}, \tag{6.3c}$$

$$\varepsilon_0 \frac{\partial \phi_0}{\partial r}|_{r=r_{DNA}} - \varepsilon_1 \frac{\partial \phi_1}{\partial r}|_{r=r_{DNA}} = -\frac{\sigma_{DNA}}{\epsilon}, \tag{6.3d}$$

$$\frac{\partial \phi_2}{\partial r}|_{r=r_{CNT}} - \varepsilon_1 \frac{\partial \phi_1}{\partial r}|_{r=r_{CNT}} = \frac{\sigma_{CNT}}{\epsilon}. \tag{6.3e}$$

Equation (6.3a) is the condition that the electric potential vanishes at infinity. Equations (6.3b) and (6.3c) are the conditions of continuity of the electric potential on the CNT and on the DNA, respectively. Equations (6.3d) and (6.3e) are the conditions of discontinuity of the electric displacement on the surfaces of the DNA and the CNT, respectively. Here, ϵ is the permittivity of free space.

σ_{CNT} in Eq. (6.3e) is the induced surface charge density on the surface of the CNT. To calculate σ_{CNT}, Minmire *et al.* results for a universal 1D DOS for CNTs [16] are utilized. The universal expression for the 1D DOS on the CNT is based on a linear energy dispersion relation for graphene [1, 2, 16]. This result has been shown to be in good agreement with *ab initio* calculations for low energies E, that is, when $|E| << |V_{pp\pi}|$ [16], where $V_{pp\pi}$ is the nearest-neighbor interaction, and $|V_{pp\pi}| = 2.5$ eV. The expression for the universal DOS per carbon atom near the Fermi level is the following [16]

$$\upsilon(E) = \frac{a}{\pi^2 r_{CNT} |V_{pp\pi}|} \sum_{m=-\infty}^{\infty} g\left(E, \gamma_m\right), \tag{6.4}$$

where $a = 2.49$ Å is the lattice constant of the graphene sheet, and it is related to the distance between the carbon atoms $a_{C-C} = 1.44$ Å as $a = \sqrt{3} a_{C-C}$

$$g(E, \gamma_m) = \begin{cases} \frac{|E|}{\sqrt{E^2 - \gamma_m^2}}, & |E| > |\gamma_m|, \\ \\ 0, & |E| < |\gamma_m|. \end{cases} \tag{6.5}$$

and

$$|\gamma_m| = \frac{a|V_{pp\pi}\left(3m - n_1 + n_2\right)|}{2\sqrt{3} r_{CNT}}. \tag{6.6}$$

Here m is an integer, and (n_1, n_2) is a pair of integer indices defining CNT's chirality. The metallic CNTs are distinguished from the semiconducting CNTs through γ_m, which explicitly depends on (n_1, n_2). For metallic CNTs, $n_1 - n_2 = 3q$, where q is an integer, whereas for semiconducting CNTs, $n_1 - n_2 \neq 3q$.

The amount of induced charge $\delta\rho$ per carbon atom can be calculated by integrating the product of the DOS with the Fermi distribution function over all energies

[21]

$$\delta\rho = -e \int_{-\infty}^{\infty} v(E)\ sgn(E)\ F\left[sgn(E)(E - E_F - q\phi_{CNT})\right] dE, \tag{6.7}$$

where E_F is the Fermi level (zero for undoped tubes), $sgn(E)$ is the sign function which is 1 for $E > 0$ and -1 for $E < 0$, and $F(E) = 1/\left[1 + \exp(E/k_BT)\right]$ is the Fermi distribution function, e is the unsigned charge of an electron, ϕ_{CNT} is the electric potential on the CNT, k_B is the Boltzmann constant, and T is the temperature. In this expression for $\delta\rho$, the integration from $-\infty$ to 0 calculates the amount of holes per carbon atom and the integration from 0 to ∞ calculates the amount of electrons per carbon atom.

The surface charge density on the CNT per unit area is defined as $\sigma_{CNT} = \delta\rho/A$, where $A = \sqrt{3}a^2/4$ is the area per carbon atom. Together with mathematical manipulations of $\delta\rho$, the expression for σ_{CNT} can be derived in the following form

$$\begin{aligned} \sigma_{CNT} &= -\frac{4e}{\sqrt{3}a\pi^2 r_{CNT}|V_{pp\pi}|} \\ &\quad \times \int_0^{\infty} \frac{\sinh\left(\frac{E_F + e\phi_{CNT}}{k_BT}\right)}{\cosh\left(\frac{E_F + e\phi_{CNT}}{k_BT}\right) + \cosh\left(\frac{E}{k_BT}\right)} g(E, \gamma_m) dE. \end{aligned} \tag{6.8}$$

By examining Eq. (6.8), it can be seen that the amount of charge on the CNT σ_{CNT} is not fixed, but rather it depends on ϕ_{CNT}. In the trivial case when $\sigma_{DNA} = 0$, the electric potential is zero everywhere, that is, $\phi_{CNT} = 0$. For undoped CNT, Eq. (6.8) predicts that $\sigma_{CNT} = 0$, which is expected. A negatively charged DNA ($\sigma_{DNA} < 0$) causes ϕ_{CNT} to be negative, and hence σ_{CNT} as given in Eq. (6.8) is positive, that is, $\sigma_{CNT} > 0$. Since the CNT is assumed to be uncharged before a DNA molecule is introduced, the total charge on the CNT surface is not maintained when the DNA charges are present. This means that the CNT is essentially connected to a source of charges or grounded. Limitations of this approach will be discussed in Subsection 6.4.4.

To simplify the calculations and analysis, let us introduce the following normalization

$$\bar{\phi}_0 = \frac{ez}{k_BT}\phi_0,\ \bar{\phi}_1 = \frac{ez}{k_BT}\phi_1,\ \bar{\phi}_2 = \frac{ez}{k_BT}\phi_2,\ \ \bar{\phi}_{CNT} = \frac{ez}{k_BT}\phi_{CNT}, \tag{6.9}$$

$$\bar{\sigma}_{DNA}=\frac{aez}{k_BT}\frac{\sigma_{DNA}}{\epsilon},\ \bar{\sigma}_{CNT}=\frac{aez}{k_BT}\frac{\sigma_{CNT}}{\epsilon},\ \bar{r}_{DNA}=\frac{r_{DNA}}{a}, \tag{6.10}$$

$$\bar{r}_{CNT}=\frac{r_{CNT}}{a},\ \bar{k}=ka,\ \bar{r}=\frac{r}{a},\ \beta=\frac{1}{z},\ l_B=\frac{e^2}{4\pi\varepsilon_0\epsilon k_BT},\ \bar{l}_B=\frac{l_B}{a}, \tag{6.11}$$

$$\bar{E}=\frac{r_{CNT}2\sqrt{3}}{a|V_{pp\pi}|}E,\ \alpha=\frac{|V_{pp\pi}|}{2\sqrt{3}k_BT},\ \frac{\alpha\bar{E}}{\bar{r}_{CNT}}=\frac{E}{k_BT}, \tag{6.12}$$

$$\bar{\gamma}_m=\gamma_m\frac{2\sqrt{3}r_{CNT}}{a\left|V_{pp\pi}\right|}=\begin{cases}\left|3m'-1\right|, & \text{semiconducting } (n_1-n_2\neq 3q)\\ \left|3m'\right|, & \text{metallic } (n_1-n_2=3q)\end{cases} \tag{6.13}$$

where z is the valence of the cation in the solution, and l_B is the Bjerrum length [22]. Here, m' has been used to replace $m-q$ in Eq. (6.6), m' is also integer. The normalized BVP has the following form

$$\begin{aligned}&\tfrac{\partial^2\bar{\phi}_0}{\partial\bar{r}^2}+\tfrac{1}{\bar{r}}\tfrac{\partial\bar{\phi}_0}{\partial\bar{r}}=\bar{k}^2\bar{\phi}_0 \text{ in } D_0,\\ &\tfrac{\partial^2\bar{\phi}_1}{\partial\bar{r}^2}+\tfrac{1}{\bar{r}}\tfrac{\partial\bar{\phi}_1}{\partial\bar{r}}=0 \text{ in } D_1,\\ &\tfrac{\partial^2\bar{\phi}_2}{\partial\bar{r}^2}+\tfrac{1}{\bar{r}}\tfrac{\partial\bar{\phi}_2}{\partial\bar{r}}=0 \text{ in } D_2,\end{aligned} \tag{6.14}$$

$$\bar{\phi}_0(\bar{r}\to\infty)=0, \tag{6.15a}$$

$$\bar{\phi}_1|_{\bar{r}=\bar{r}_{CNT}}=\bar{\phi}_2|_{\bar{r}=\bar{r}_{CNT}}, \tag{6.15b}$$

$$\bar{\phi}_0|_{\bar{r}=\bar{r}_{DNA}}=\bar{\phi}_1|_{\bar{r}=\bar{r}_{DNA}}, \tag{6.15c}$$

$$\varepsilon_0\frac{\partial\bar{\phi}_0}{\partial\bar{r}}|_{\bar{r}=\bar{r}_{DNA}}-\varepsilon_1\frac{\partial\bar{\phi}_1}{\partial\bar{r}}|_{\bar{r}=\bar{r}_{DNA}}=-\bar{\sigma}_{DNA}, \tag{6.15d}$$

$$\frac{1}{\varepsilon_0}\frac{\partial\bar{\phi}_2}{\partial\bar{r}}|_{\bar{r}=\bar{r}_{CNT}}-\frac{\varepsilon_1}{\varepsilon_0}\frac{\partial\bar{\phi}_1}{\partial\bar{r}}|_{\bar{r}=\bar{r}_{CNT}}=\bar{\sigma}_{CNT}, \tag{6.15e}$$

where

$$\bar{\sigma}_{CNT}=\begin{cases}\text{metallic:}\quad \bar{\sigma}^m_{CNT}=-\frac{8z\bar{l}_B}{3\pi\bar{r}^2_{CNT}}\tanh\left(\frac{\alpha\bar{E}_F}{\bar{r}_{CNT}}+\beta\bar{\phi}_{CNT}\right)\\ \times\int_0^\infty\frac{1}{1+\frac{\cosh(\alpha\bar{E}/\bar{r}_{CNT})}{\cosh(\alpha\bar{E}_F/\bar{r}_{CNT}+\beta\bar{\phi}_{CNT})}}\sum_{m'=\lceil-\bar{E}/3\rceil}^{\lceil\bar{E}/3\rceil-1}\frac{\bar{E}}{\sqrt{\bar{E}^2-(3m')^2}}d\bar{E},\\ \text{semiconducting:}\quad \bar{\sigma}^s_{CNT}=-\frac{8z\bar{l}_B}{3\pi\bar{r}^2_{CNT}}\tanh\left(\frac{\alpha\bar{E}_F}{\bar{r}_{CNT}}+\beta\bar{\phi}_{CNT}\right)\\ \times\int_0^\infty\frac{1}{1+\frac{\cosh(\alpha\bar{E}/\bar{r}_{CNT})}{\cosh(\alpha\bar{E}_F/\bar{r}_{CNT}+\beta\bar{\phi}_{CNT})}}\sum_{m'=\lceil(-\bar{E}+1)/3\rceil}^{\lceil(\bar{E}+1)/3\rceil-1}\frac{\bar{E}}{\sqrt{\bar{E}^2-(3m'-1)^2}}d\bar{E}.\end{cases} \tag{6.16}$$

Here, the superscript "m" stands for $\bar{\sigma}_{CNT}$ on a metallic CNT, and the superscript "s" stands for that on a semiconducting CNT.

6.4 Results and discussions

In this section we provide the expressions for the electric potentials in each region ($D_0,\ D_1$ and D_2) and examine the tendency of their behavior.

6.4.1 Expressions for electric potential

The general solution to the ordinary differential equations, Eqs. (6.14), is

$$\bar{\phi}_0 = C_1 K_0\left(\bar{k}\bar{r}\right) + C_5 I_0(\bar{k}\bar{r}), \tag{6.17}$$

$$\bar{\phi}_1 = C_2 + C_3 \ln(\bar{r}), \tag{6.18}$$

$$\bar{\phi}_2 = C_4 + C_6 \ln(\bar{r}), \tag{6.19}$$

where $C_i\ (i = 1...5)$ are integration constants to be determined from the BCs, $K_0(x)$ and $I_0(x)$ are the 0th order modified Bessel functions of the first and the second kind, respectively. The asymptotic behavior of $K_0(x)$ and $I_0(x)$ is such that as $x \to \infty,\ K_0(x) \to 0$ and $I_0(x) \to \infty$ [23]. According to Eq. (6.15a), the electric potential $\bar{\phi}_0$, Eq. (6.17), should vanish at large distances from the CNT-DNA hybrid, that is, when $\bar{r} \to \infty$. Therefore, $C_5 = 0$. The electric potential $\bar{\phi}_2$ in the interior of the CNT, Eq. (6.19), should be finite. Because the logarithmic term exhibits singularity at $\bar{r} = 0$, C_6 must be zero.

The unknown coefficients C_1, C_2, C_3 and C_4 can be found by utilizing the four BCs, Eqs. (6.15b)–(6.15e). The final expressions for the electric potential in each region are

$$\bar{\phi}_0 = \frac{\bar{r}_{DNA}\bar{\sigma}_{DNA} + \varepsilon_0 \bar{r}_{CNT}\bar{\sigma}_{CNT}}{\bar{k}\bar{r}_{DNA}\varepsilon_0 K_1\left(\bar{k}\bar{r}_{DNA}\right)} K_0\left(\bar{k}\bar{r}\right) \text{ in } D_0, \tag{6.20}$$

$$\bar{\phi}_1 = \frac{\bar{r}_{DNA}\bar{\sigma}_{DNA} + \varepsilon_0 \bar{r}_{CNT}\bar{\sigma}_{CNT}}{\bar{k}\bar{r}_{DNA}\varepsilon_0 K_1\left(\bar{k}\bar{r}_{DNA}\right)} K_0\left(\bar{k}\bar{r}_{DNA}\right) + \frac{\varepsilon_0}{\varepsilon_1}\bar{r}_{CNT}\bar{\sigma}_{CNT} \ln\left(\frac{\bar{r}_{DNA}}{\bar{r}}\right) \text{ in } D_1, \tag{6.21}$$

$$\bar{\phi}_2 = \frac{\bar{\sigma}_{DNA}\ K_0\left(\bar{k}\bar{r}_{DNA}\right)}{\bar{k}\varepsilon_0 K_1\left(\bar{k}\bar{r}_{DNA}\right)} + \bar{r}_{CNT}\bar{\sigma}_{CNT}\left[\frac{\varepsilon_0}{\varepsilon_1}\ln\left(\frac{\bar{r}_{DNA}}{\bar{r}_{CNT}}\right) + \frac{K_0\left(\bar{k}\bar{r}_{DNA}\right)}{\bar{k}\bar{r}_{DNA}K_1\left(\bar{k}\bar{r}_{DNA}\right)}\right] \text{ in } D_2. \tag{6.22}$$

As was mentioned earlier, $\bar{\sigma}_{CNT}$ is the induced surface charge density on the CNT by $\bar{\sigma}_{DNA}$ and it is coupled with $\bar{\phi}_2$ through Eq. (6.16). It is clear from Eq. (6.22) that the electric potential in the interior of the CNT is a constant independent of position r, that is, $\bar{\phi}_2 = \bar{\phi}_{CNT}$, the potential on the CNT surface. Therefore, in order to determine the actual values of the electric potential, Eqs. (6.20)–(6.22) need to be solved iteratively with Eq. (6.16).

Eqs. (6.20)–(6.22) also show that the electric potential depends on the following parameters: $\bar{r}_{CNT}$ (dimensionless radius of the CNT), $\bar{r}_{DNA}$ (dimensionless radius of the cylindrical surface representing DNA), $\bar{\sigma}_{DNA}$ (normalized DNA charge density), $\bar{k}$ (normalized Debye length of the solution), and ε_1 (dielectric constant of the ring region). Note that ε_0 (dielectric constant of the aqueous solution) is fixed at 80 throughout this work. DNA dispersion of the CNTs was performed in a solution with monovalent salt [3], therefore the region D_0 is considered to be filled with a univalent electrolyte solution ($z = 1$). In the following, we first demonstrate the results for $r_{CNT} = 5$ Å for both metallic and semiconducting CNTs. This value for the radius r_{CNT} is chosen because in the DNA-assisted CNTs separation experiments, HiPco produced CNTs are used [5]. It is assumed that the mean diameter of such CNTs is 1 nm [24]. The charges of a ssDNA molecule, when wrapped around a CNT, are found to be located at a distance of 5 Å away from the circumference of the CNT [9]. This means that the diameter of the cylindrical surface representing DNA is 2 nm. Using this geometry, we present the electric potential for different values of $\bar{\sigma}_{DNA}$ and $1/\bar{k}$, which allows us to study how the electric potential depends on the electronic nature of the CNT (metallic or semiconducting) at different DNA's helical angle and concentration of the solution. Because water molecules have been reported [9] to locate between the CNT surface and DNA charges, there is some uncertainty about what is an appropriate value for ε_1. In the following, we take the two limiting values: 1 for vacuum fully occupying the ring and 80 for water fully occupying the ring, and demonstrate how the results can be different for the two extreme situations. Finally, we will address the results for different CNT sizes.

6.4.2 Estimation of the range of $\bar{\sigma}_{DNA}$

For the above mentioned geometry ($r_{CNT} = 5$ Å, $r_{CNT} = 10$ Å), let us estimate an effective surface charge density σ_{DNA} on the cylinder representing the wrapped ssDNA molecule. To do that let us look at Figure 6.2. The helical angle of the wrapped ssDNA is defined as the angle between the DNA and the circumference of the CNT (See Figure 6.2b). The neighboring charges on the backbone of the

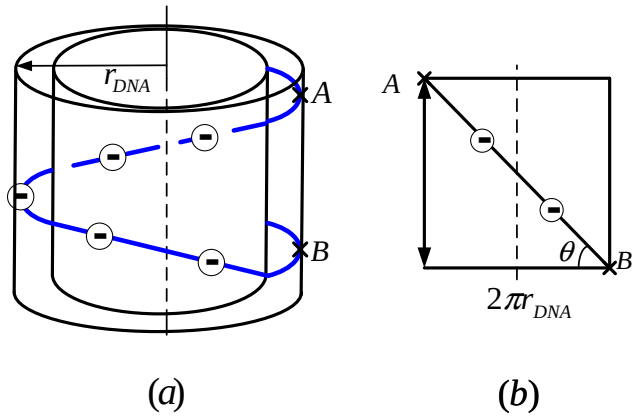

Figure 6.2: Geometry of the model CNT-DNA hybrid: a) three-dimensional model of the CNT-DNA hybrid for a complete helix turn. DNA helix lays on the surface of the outside cylinder with radius r_{DNA} ; b) expanded view of the cylindrical surface representing the DNA molecule for a complete helix turn.

DNA are considered to be 7 Å apart [25]. Thus, the charges corresponding to a complete helix turn are $e \times (2\pi r_{DNA}/\cos\theta) \times 7$Å (See Figure 6.2b). The area of the cylindrical surface corresponding to a complete helix turn is $(2\pi r_{DNA})^2 \tan\theta$. Therefore the areal density of the smeared charges is

$$\sigma_{DNA} = -\frac{e}{7\text{Å}\ 2\pi r_{DNA} \sin\theta}. \tag{6.23}$$

In literature, different values of the wrapping angles for CNT-DNA hybrids are reported. Lustig *et al.* have reported $\theta = 40^o$. Their result is supported by atomic force microscopy (AFM) measurements [11]. Kilina *et al.* observed through scanning tunneling microscopy (STM) measurements that very stable CNT-DNA hybrids are formed for $\theta = 26.4^o$ [26]. Note that in these works [11, 26], the reported helical angle was complementary to θ shown in Figure 6.2, and we have converted

it to our definition. If we consider a wider range of θ that covers the previously reported data, $\theta = (10^o; 60^o)$, the corresponding surface charge density of the cylinder representing DNA is in the range of $(-0.21; -0.04)$ C/m^2. With the normalization introduced in Eq. (6.10), the relation between $\bar{\sigma}_{DNA}$ and σ_{DNA} is the following $\bar{\sigma}_{DNA} = \sigma_{DNA}\,[aez]\,/\,[\epsilon k_B T]$, where $e = 1.6 \times 10^{-19}$ C, $k_B = 1.38 \times 10^{-23}$ J/K, $\epsilon = 8.85 \times 10^{-12}$ F/m, and $z = 1$. At room temperature $T = 300$ K, the range for $\bar{\sigma}_{DNA}$ is $(-227.8; -45.68)$.

6.4.3 Numerical results

In this subsection, the numerical results are provided for the normalized electric potential in all regions due to the CNT-DNA hybrid. Because the fundamental difference between metallic and semiconducting CNTs is reflected through the induced $\bar{\sigma}_{CNT}$, it will also be discussed in detail. Using the symbol $\bar{\phi}$, without any subscripts, we define the combined electric potential in all regions ($D_2,\ D_1$ and D_0), that is, $\bar{\phi}_2 \cup \bar{\phi}_1 \cup \bar{\phi}_0$. When it is needed to emphasize the type of the CNT a certain subscript, "m" or "s", will be added to $\bar{\sigma}_{CNT}$ and $\bar{\phi}$. In Figures 6.3–6.8, calculations are conducted for metallic and semiconducting CNT-DNA hybrids of the same geometry as specified earlier. The Bjerrum length l_B is taken to be 7 Å [22]. Intrinsic CNT is considered, therefore the Fermi level is taken to be zero, $E_F = 0$. The normalized parameters which correspond to the mentioned fixed parameters are the following: $\alpha = 27.89,\ \beta = 1,\ \bar{r}_{CNT} = 2.01,\ \bar{r}_{DNA} = 4.02,$ and $\bar{l}_B = 2.81$,which are fixed during the following discussion. We study a range of the Debye length of the electrolyte solution, from 1 to 100 nm, and the normalized values are $1/\bar{k}$ in the range $(4.02; 402)$. $\bar{\sigma}_{DNA}$ will be specified from the defined range in Subsection 6.4.2, and ε_1 will be taken as 1 or 80 to capture the limiting situations.

As the first example, we use Figure 6.3 to describe the electric potential in each region, and to compare $\bar{\phi}$ for the metallic CNT-DNA and for the semiconducting CNT-DNA hybrids. Calculations are performed for the Debye length $1/\bar{k}$ being equal to 402 (corresponding to $1/k = 100$ nm), and the dielectric constant of the ring $\varepsilon_1 = 80$. The normalized surface charge density is taken to be $\bar{\sigma}_{DNA} = -80$

corresponding to the wrapping angle of 29.7^o. Figure 6.3(a) plots the normalized electric potential $\bar{\phi}$ versus the normalized distance $\bar{r}$. Each region has a certain range for $\bar{r}$, which is displayed on Figure 6.3(a), $\bar{r}$ from the range $[0; 2.01]$ belongs to D_2; $\bar{r}$ from the range $[2.01; 4.02]$ belongs to D_1; and $\bar{r}$ from the range $[4.02; 80.32]$ belongs to D_0. The black dashed line represents $\bar{\phi}^m$ due to the metallic CNT-DNA hybrid, and the black solid line represents $\bar{\phi}^s$ for the semiconducting CNT-DNA hybrid. The general trend of $\bar{\phi}(r)$ is the same for metallic and semiconducting CNTs. Specifically, a negative source charge, $\bar{\sigma}_{DNA} < 0$, causes the normalized electric potential in all regions to be negative, $\bar{\phi} < 0$, with the largest magnitude at the location of the DNA, that is $\bar{r} = 4.02$. In D_0, as $\bar{r}$ increases going away from the DNA, the magnitude of the electric potential decreases. This is because the influence of the DNA charge diminishes due to the screening from the electrolyte solution. In D_1, as $\bar{r}$ decreases going away from the DNA to the CNT, the magnitude of the electric potential also decreases, but the decrease is much more gradual due to the absence of the ions. Finally, in D_2, the electric potential is a constant independent of position.

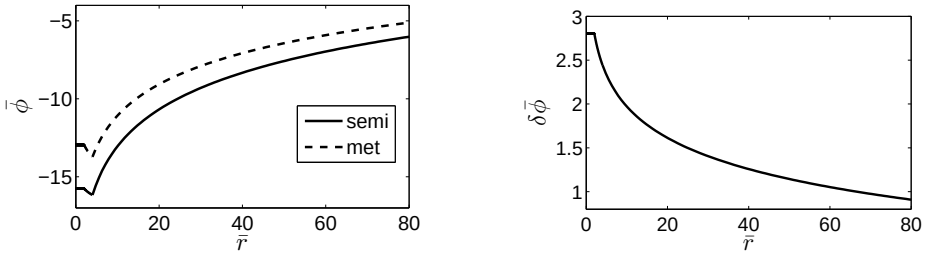

(a) (b)

Figure 6.3: a) the normalized potential $\bar{\phi}$ in all domains versus the normalized distance $\bar{r}$ for the metallic and semiconducting CNT-DNA hybrids; b) the difference $\delta\bar{\phi}$ versus $\bar{r}$. Here, $\alpha = 27.89, \beta = 1, E_F = 0, \bar{l}_B = 2.81, \bar{r}_t = 2.01, \varepsilon_0 = 80, \bar{r}_{DNA} = 2\bar{r}_{CNT}, \bar{\sigma}_{DNA} = -80$, $\varepsilon_1 = 80$ and $1/\bar{k} = 402$.

As can be seen in Figure 6.3(a), the qualitative behavior is the same for both curves. But there is a visible quantitative difference between them. For the same normalized distance $\bar{r}$, the magnitude of $\bar{\phi}^m$ is smaller than $\bar{\phi}^s$ in all three regions. We are motivated by experiments done by Zheng *et al.* [3], therefore the main at-

tention is given to the electric potential $\bar{\phi}_0$ in D_0. For any fixed $\bar{r}$ from D_0, the magnitude of $\bar{\phi}_0^m$ is smaller than that of $\bar{\phi}_0^s$, that is, $\left|\bar{\phi}_0^m\right| < \left|\bar{\phi}_0^s\right|$. This means that the binding energy of the metallic CNT-DNA hybrid to the charged column will be smaller. Therefore, as the salt concentration increases, the metallic CNT-DNA hybrids will be eluting earlier. This fact is consistent with the experiments. The quantitative difference between the two curves is plotted in Figure 6.3(b), where $\delta\bar{\phi}$ is defined as $\delta\bar{\phi} = \bar{\phi}^m - \bar{\phi}^s$. The largest difference appears to be in region D_2. Whereas in regions D_1 and D_0, as r increases, $\delta\bar{\phi}$ decreases. As was mentioned before $\delta\bar{\phi}$ in D_0 governs the difference in the electrostatic interaction with charged objects in a solution, therefore we define the relative percentage difference in D_0 as $\eta_0 = \left|\bar{\phi}_0^m - \bar{\phi}_0^s\right| / \left|\bar{\phi}_0^m\right| \times 100\%$. Our calculations show that $\eta_0 \simeq 17.8\%$ everywhere in D_0 for the set of parameters $1/\bar{k}$, ε_1 and $\bar{\sigma}_{DNA}$ used here. Thus, the electrostatic interaction of a charged object in solution with a metallic CNT-DNA hybrid is approximately 20% weaker than that with a semiconducting CNT-DNA hybrid, irrespective of it separation from the hybrids. This is a considerable difference, and it is consistent with the earlier observed elution of metallic CNT-DNA hybrids in experiments [3].

In the above calculations, ε_1 has been fixed at 80 corresponding to water fully filling the gap between the CNT and the DNA. This may not be a case, as was shown in previous MD simulations [9], where the space between them was observed to be occupied only partially by water. In such a case, it is expected that this ε_1 can be much smaller than 80. To see how a smaller value for ε_1 can affect the results, let us to consider the other limiting situation where $\varepsilon_1 = 1$ corresponding to D_1 free of water molecules. Figure 6.4 plots $\bar{\phi}$ versus $\bar{r}$ for the same $1/\bar{k} = 402$ and $\bar{\sigma}_{DNA} = -80$, but $\varepsilon_1 = 1$. As in the previous figure, the dashed black curve corresponds to the metallic CNT-DNA hybrid, and the solid black curve corresponds to the semiconducting CNT-DNA hybrid. The same variation of $\bar{\phi}$ versus $\bar{r}$ is observed in all domains (See Figures 6.3(a) and 6.4(a)). In addition, the magnitude for the electric potential $\bar{\phi}^m$ is still smaller than that of $\bar{\phi}^s$ in all regions. However, their difference, $\delta\bar{\phi}$ as shown in Figure 6.4(b), is very different from the case of $\varepsilon_1 = 80$. While $\delta\bar{\phi}$ in region D_2 is much larger in the case of $\varepsilon_1 = 1$, being 9.62 compared

with 2.8 in Figure 6.3(b), it undergoes a drastic drop in region D_1, and becomes significantly smaller than the case of $\varepsilon_1 = 80$ in region D_0, as shown in the insert of Figure 6.4(b). The relative percentage difference is approximately $\eta_0 = 4.26\%$ for $\varepsilon_1 = 1$ everywhere in D_0. This means that with $\varepsilon_1 = 1$, the interaction energy between a charged object in a solution and the CNT-DNA hybrid is only less than 5% weaker in the case of a metallic-CNT core.

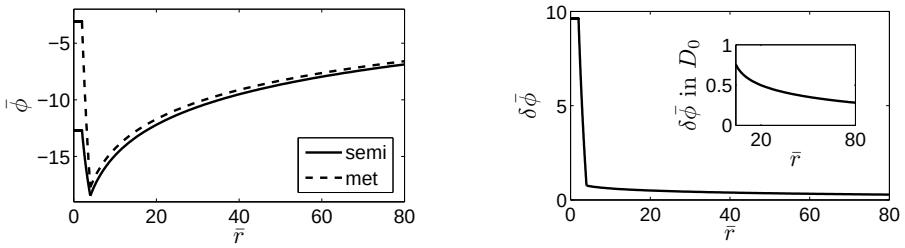

(a) (b)

Figure 6.4: a) the normalized potential $\bar{\phi}$ in all domains versus the normalized distance $\bar{r}$ for metallic and semiconducting CNT-DNA hybrids; b) the difference $\delta\bar{\phi}$ versus $\bar{r}$. Here, $\alpha = 27.89, \beta = 1, E_F = 0, \bar{l}_B = 2.81, \bar{r}_{CNT} = 2.01, \varepsilon_0 = 80, \bar{r}_{DNA} = 2\bar{r}_{CNT}, \bar{\sigma}_{DNA} = -80$, $\varepsilon_1 = 1$ and $1/\bar{k} = 402$.

At first, the fact, that as ε_1 decreases the difference $\delta\bar{\phi}$ decreases in D_0, appears to be counterintuitive. The dielectric constant is a factor that characterizes the polarization of media. Hence intuitively, a smaller ε_1 introduces a smaller electrostatic screening from the dielectric media in D_1, and may enlarge the difference between $\bar{\phi}^m$ and $\bar{\phi}^s$. To explain this observation, let us look at the expression for $\bar{\phi}_0$, Eq. (6.20), and identify the factors influencing its behavior as ε_1 changes. It can be seen that the terms due to the DNA, $\bar{r}_{DNA}, \bar{\sigma}_{DNA}$ do not change as ε_1 changes. After careful consideration, it could be noticed that $\bar{\sigma}_{CNT}$ in the second term depends on $\bar{\phi}_2$, which in turn depends on ε_1. Therefore, in order to explain why $\delta\bar{\phi}$ in D_0 decreases as ε_1 decreases, we will examine how $\bar{\phi}_2$ and $\bar{\sigma}_{CNT}$ vary with ε_1.

Figures 6.5(a) and 6.5(b) depict $\bar{\phi}_2$ versus ε_1 and $\bar{\sigma}_{CNT}$ versus ε_1 for both types of the CNT-DNA hybrids. On both figures, the dashed black curve represents $\bar{\phi}_2^m$ or $\bar{\sigma}_{CNT}^m$, and the solid black curve represents $\bar{\phi}_2^s$ or $\bar{\sigma}_{CNT}^s$. From these two figures, it can be seen that at a given ε_1, $\left|\bar{\phi}_2^m\right| < \left|\bar{\phi}_2^s\right|$ and $|\bar{\sigma}_{CNT}^m| > |\bar{\sigma}_{CNT}^s|$, respectively. These two results are consistent and can be explained by Eq. (6.22). The first term

in Eq. (6.22) is the electric potential on the CNT surface in D_2 due to the DNA charges only, and is negative because $\bar{\sigma}_{DNA} < 0$. The second term in Eq. (6.22) represents the effect of the CNT induced charges, and being positive, competes with the first term in determining $\bar{\phi}_2$. The larger $\bar{\sigma}_{CNT}$, the less negative $\bar{\phi}_2$ becomes. Since at a given ε_1, more charges are generated on the metallic CNT than on the semiconducting CNT, the magnitude for the electric potential on the metallic CNT is smaller than on the semiconducting CNT.

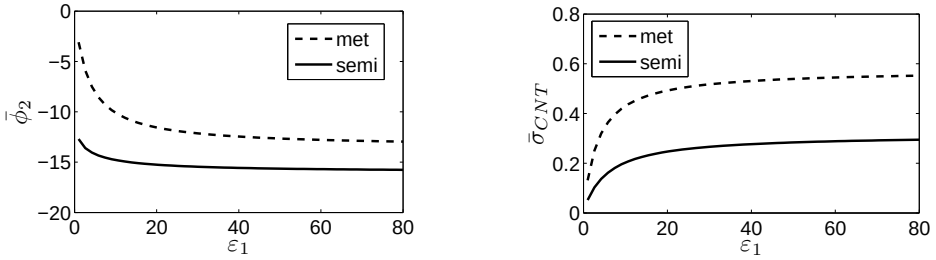

(a) (b)

Figure 6.5: a) the normalized electric potential $\bar{\phi}_2$ on the tube versus ε_1; b) the normalized surface charge density $\bar{\sigma}_{CNT}$ on the tube versus ε_1. Here, $\alpha = 27.89, \beta = 1, E_F = 0, 1/\bar{k} = 402, \varepsilon_0 = 80, \varepsilon_1 = (1, 80), \bar{r}_{CNT} = 2.01, \bar{r}_{DNA} = 2\bar{r}_{CNT}, \bar{l}_B = 2.81$, and $\bar{\sigma}_{DNA} = -80$.

Eq. (6.22) also shows that the dependence of $\bar{\phi}_2$ on ε_1 is present only in the second term. As ε_1 increases, the second term decreases, causing $\bar{\phi}_2$ to be more negative, as seen in Figure 6.5(a). Physically, the larger screening associated with a larger value of ε_1 results in a smaller electric field in the ring, and hence less increase in electric potential from the DNA surface to the CNT surface. The net result of this is the more negative potential on the CNT and more induced positive charges. This trend is true for both metallic and semiconducting CNT-DNA hybrids. However, the increase in $\bar{\sigma}_{CNT}$ with ε_1 is more pronounced for metallic CNT. Consequently, the difference $\delta\bar{\sigma}_{CNT} = \bar{\sigma}^m_{CNT} - \bar{\sigma}^s_{CNT}$ is significantly smaller at a small value of ε_1. Since from Eq. (6.20), the electric potential $\bar{\phi}_0$ crucially depends on $\bar{\sigma}_{CNT}$, the smaller $\delta\bar{\sigma}_{CNT}$ that occurs at smaller ε_1 leads to the fact that $\delta\bar{\phi}$ in D_0 decreases as ε_1 is changed from 80 to 1.

In Figure 6.5(b), $\bar{\sigma}_{DNA} = -80$, whereas the induced charges $\bar{\sigma}_{CNT}$ for the two

types of tubes is less than 0.6 for the entire range of ε_1. This represents a very small fraction of the $\bar{\sigma}_{DNA}$. For example, at $\varepsilon_1 = 80$, the generated charge on the metallic CNT $\bar{\sigma}^m_{CNT}$ is only 0.7% of $\bar{\sigma}_{DNA}$ and the generated charge on the semiconducting CNT $\bar{\sigma}^s_{CNT}$ is only 0.37% of $\bar{\sigma}_{DNA}$. Nevertheless, such small amount of induced charges cause nearly a 20% difference between $\bar{\phi}^m_0$ and $\bar{\phi}^s_0$. This can be explained by examining Eq. (6.20). The second term in the numerator captures the effect of $\bar{\sigma}_{CNT}$, and it is amplified by $\varepsilon_0 = 80$, the dielectric constant of the solution.

The above results are obtained for fixed values of $1/\bar{k} = 402$ and $\bar{\sigma}_{DNA} = -80$. Now, it is of interest to study how varying the Debye length changes the results for $\bar{\phi}_0$. It is important because in the experiments [3], different CNT-DNA hybrids were separated according to the electronic properties of CNT's core by increasing the salt concentration of the electrolyte solution (decreasing Debye length). Figure 6.6 plots $\bar{\phi}_0$ versus $1/\bar{k}$ evaluated at an arbitrary point $\bar{r} = 3\bar{r}_{DNA}$. The black dashed curve represents $\bar{\phi}^m_0$, and the solid black curve represents $\bar{\phi}^s_0$. For the same value of the Debye length $1/\bar{k}$, the magnitude of $\bar{\phi}^m_0$ is smaller than $\bar{\phi}^s_0$. For example, for the metallic CNT-DNA hybrid, as $1/\bar{k}$ changes from 400 (corresponding to the Debye length of 100 nm) to 4 (corresponding to the Debye length of 1 nm), $\bar{\phi}^m_0$ at the point $\bar{r} = 3\bar{r}_{DNA}$ changes from -10.54 (corresponding to $\phi^m_0 = -0.27$ V) to -0.22 (corresponding to $\phi^m_0 = -5.7$ mV). For the semiconducting CNT-DNA hybrid, if the normalized Debye length is reduced from 400 to 4, $\bar{\phi}^s_0$ at the point $\bar{r} = 3\bar{r}_{DNA}$ changes from -12.41 (corresponding to $\phi^s_0 = -0.32$ V) to -0.23 (corresponding to $\phi^s_0 = -5.9$ mV). Therefore, as $1/\bar{k}$ decreases, the difference between $\bar{\phi}^m_0$ and $\bar{\phi}^s_0$ greatly decreases. This happens because the electric potential due to the source, $\bar{\sigma}_{DNA}$, becomes screened.

Before this moment we have studied cases with varying ε_1 and $1/\bar{k}$. Now, it is time to fix $1/\bar{k}$ and ε_1 and vary $\bar{\sigma}_{DNA}$. This is important because different helical angles have been reported [11, 26], and the magnitude for $\bar{\sigma}_{DNA}$ is influenced by the helical angle (See subsection 6.4.2). Here, we examine the curves of the electric potential in all domains for two different values of $\bar{\sigma}_{DNA}$ corresponding to two different wrapping angles. Figure 6.7 plots $\bar{\phi}$ versus $\bar{r}$ for $1/\bar{k} = 402$, $\varepsilon_1 = 80$: a) $\bar{\sigma}_{DNA} = -45.68$ corresponding to $\theta = 60^o$; and b) $\bar{\sigma}_{DNA} = -227.8$ correspond-

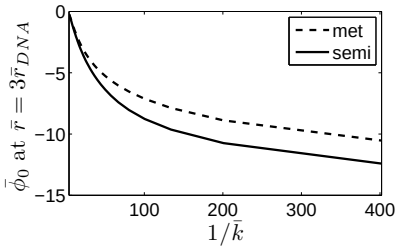

Figure 6.6: The normalized electric potential $\bar{\phi}_0$ evaluated at the point $\bar{r} = 3\bar{r}_{DNA}$ versus the normalized Debye length $1/\bar{k}$ of the solution. For the following parameters $\alpha = 27.89, \beta = 1, E_F = 0, \varepsilon_0 = 80, \varepsilon_1 = 80, \bar{l}_B = 2.81, \bar{r}_{CNT} = 2.01, \bar{r}_{DNA} = 2\bar{r}_{CNT}, \bar{\sigma}_{DNA} = -80$ and $1/\bar{k} = (4.02, 402)$.

ing to the wrapping angle $\theta = 10^o$. The black dashed line represents $\bar{\phi}^m$ due to the metallic CNT-DNA hybrid, and the black solid line represents $\bar{\phi}^s$ for the semiconducting CNT-DNA hybrid. The general trend of the curves in each domain is the same as in Figures Figure 6.3(a) and 6.4(a). For $\bar{\sigma}_{DNA} = -45.68$, as it can be seen from Figure 6.7(a), for any $\bar{r}$, $\left|\bar{\phi}^s\right| > \left|\bar{\phi}^m\right|$, and the relative difference is $\eta_0 = 37.11\%$. Whereas, for $\bar{\sigma}_{DNA} = -227.8$, the reverse behavior is observed. That is, for any $\bar{r}$, $\left|\bar{\phi}^s\right| < \left|\bar{\phi}^m\right|$, and especially for $\left|\bar{\phi}^s_0\right| < \left|\bar{\phi}^m_0\right|$. The relative difference is $\eta_0 = 9.53\%$. The first result implies that $\bar{\phi}^m_0$ is approximately 37% weaker than $\bar{\phi}^s_0$. Whereas, the latter result implies that $\bar{\phi}^m_0$ is approximately 10% stronger than $\bar{\phi}^s_0$. To explain why this is the case, let us look at the expression for $\bar{\phi}_0$, that is, Eq. (6.20). This expression depends in $\bar{\sigma}_{CNT}$, which in turns depends on $\bar{\phi}_2$. Therefore, in the next figure, let us look how $\bar{\sigma}_{CNT}$ and $\bar{\phi}_2$ vary with $\bar{\sigma}_{DNA}$.

Figure 6.8(a) plots $\bar{\sigma}_{CNT}$ versus $\bar{\sigma}_{DNA}$ and Figure 6.8(b) plots $\bar{\phi}_2$ versus $\bar{\sigma}_{DNA}$ for the Debye length of 100 nm, and $\varepsilon_0 = \varepsilon_1 = 80$. As can be seen from Figure 6.8, when $\bar{\sigma}_{DNA}$ is in the range from ~ -171 (corresponding to 13.4^o) to -42 (corresponding to 70^o), then $\bar{\sigma}^m_{CNT} > \bar{\sigma}^s_{CNT}$ and $\left|\bar{\phi}^m_2\right| < \left|\bar{\phi}^s_2\right|$. $\bar{\sigma}_{DNA}$ is not considered to be larger than -42 because it corresponds to a very loose wrapping of a DNA around CNT. To our knowledge, wrapping angles larger than 70^0 (consistent with our formulation) were not observed experimentally. As the magnitude of $\bar{\sigma}_{DNA}$ increases further, the behavior of $\bar{\sigma}^s_{CNT}$ with respect to $\bar{\sigma}^m_{CNT}$ becomes "wave-like", as well as, the behavior of $\bar{\phi}^m_2$ with respect to $\bar{\phi}^s_2$. As shown on Figure

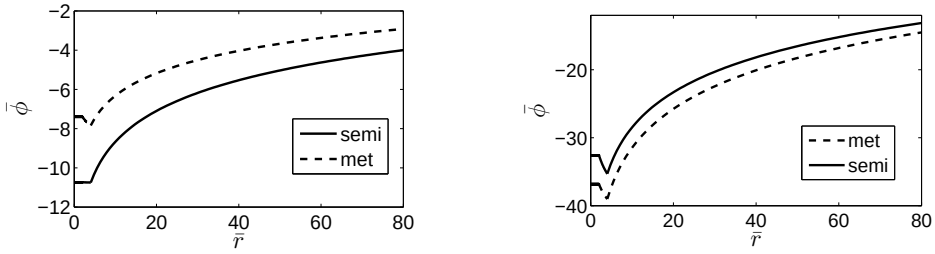

(a) (b)

Figure 6.7: The normalized potential $\bar{\phi}$ in all domains versus the normalized distance $\bar{r}$ for the metallic and semiconducting CNT-DNA hybrids: a) $\bar{\sigma}_{DNA} = -45.68$ and b) $\bar{\sigma}_{DNA} = -227.8$. Here, $\alpha = 27.89, \beta = 1, E_F = 0, \bar{l}_B = 2.81, \bar{r}_{CNT} = 2.01, \varepsilon_0 = 80, \bar{r}_{DNA} = 2\bar{r}_{CNT}$, $\varepsilon_1 = 80$ and $1/\bar{k} = 402$.

6.7, this behavior influences the curves of the electric potential in all domains. It is known from the experimental results that the metallic CNT-DNA hybrids elute earlier from the charged wall than the semiconducting ones. Therefore, it is expected that $\left|\bar{\phi}_2^m\right| < \left|\bar{\phi}_2^s\right|$. One of the reason for the "wave-like" behavior observed in Figure 6.8 could be that the universal DOS is only valid for low energies $|E| << \Lambda = 2r_{CNT}/a_{C-C}$ [16], that is, low electric potential as well. For higher values for the electric potential, the results might not be accurate.

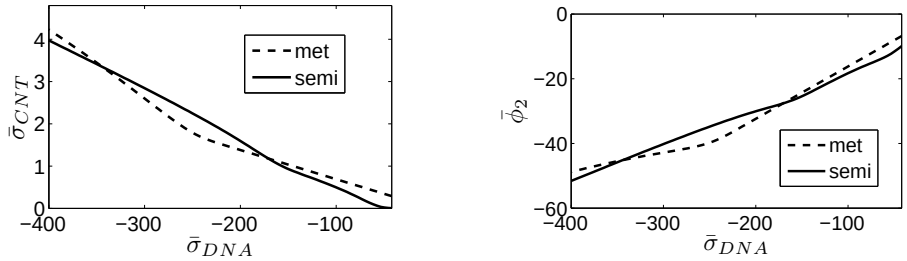

(a) (b)

Figure 6.8: a) the normalized surface charge density on the CNT $\bar{\sigma}_{CNT}$ versus $\bar{\sigma}_{DNA}$; b) the normalized electric potential on the CNT $\bar{\phi}_2$ versus $\bar{\sigma}_{DNA}$. For the following parameters $\alpha = 27.89, \beta = 1, E_F = 0, \varepsilon_0 = 80, \varepsilon_1 = 80, \bar{l}_B = 2.81, \bar{r}_{CNT} = 2.01, \bar{r}_{DNA} = 2\bar{r}_{CNT}$, and $1/\bar{k} = 402$.

Finally, let us study how the difference between the electric potential in D_0 is influenced by the size of the CNTs. In the above calculations we have considered $r_{CNT} = 5$ Å and $r_{DNA} = 10$ Å (See Figure 6.3). Keeping the distance between the

CNT and the DNA fixed and equal to 5 Å, let us look at the two cases: a) $r_{CNT} = 4$ Å ($\bar{r}_{CNT} = 1.61$) [9] and b) $r_{CNT} = 1$ nm ($\bar{r}_{CNT} = 4.02$) [1]. The latter value for r_{CNT} is chosen because the observed ssCNTs have diameters smaller than 2 nm [1]. As can be seen from Eq. (6.23), $\bar{\sigma}_{DNA}$ depends on r_{DNA}. Previously $\bar{\sigma}_{DNA}$ equal to -80 was considered, it corresponds to the wrapping angle equal to $\theta = 29.7^0$ (See Figure 6.3). By keeping the same wrapping angle ($\theta = 29.7^0$): $r_{DNA} = 9$ Å ($\bar{r}_{DNA} = 3.61$) corresponds to $\bar{\sigma}_{DNA} = -88.71$, and $r_{DNA} = 15$ Å ($\bar{r}_{DNA} = 6.02$) corresponds to $\bar{\sigma}_{DNA} = -53.23$. In this calculations, other parameters are kept fixed (as in the first example) $\alpha = 27.89,\ \beta = 1,\ \bar{l}_B = 2.81, 1/\bar{k} = 402$, and $\varepsilon_1 = 80$. Figure 6.9 plots $\bar{\phi}$ versus $\bar{r}$ for the parameters mentioned above and for the following geometries of the CNT-DNA hybrids: a) $\bar{r}_{CNT} = 1.61, \bar{r}_{DNA} = 3.61$ and $\bar{\sigma}_{DNA} = -88.71$; and b) $\bar{r}_{CNT} = 4.02, \bar{r}_{DNA} = 6.02$ and $\bar{\sigma}_{DNA} = -53.23$. As before, the black dashed line represents $\bar{\phi}^m$, and the black solid line represents $\bar{\phi}^s$. The general trend of the curves in each domain is the same as in Figures 6.3(a), 6.4(a) and 6.7. Our numerical results show that for a) $\eta_0 \simeq 27.72\%$, and b) $\eta_0 \simeq 2.13\%$. This shows that as r_{CNT} increases the difference η_0 decreases. It is expected because for a semiconducting CNT, the band gap is inversely proportional to its diameter [1]. This means that a larger diameter semiconducting CNT have a smaller gap, which implies such semiconducting CNT behaves more like a metallic one.

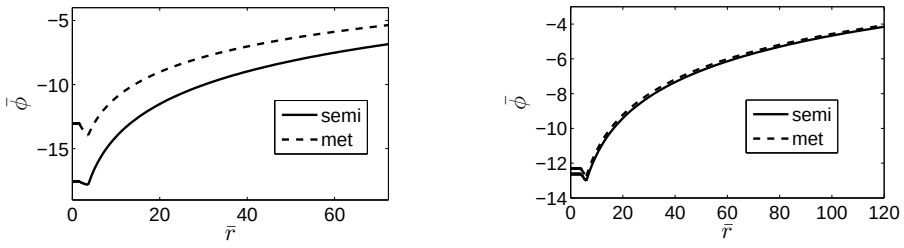

(a) (b)

Figure 6.9: The normalized potential $\bar{\phi}$ in all domains versus the normalized distance $\bar{r}$ for the metallic and semiconducting CNT-DNA hybrids a) $\bar{r}_{CNT} = 1.61, \bar{r}_{DNA} = 3.61$ and $\bar{\sigma}_{DNA} = -88.71$; and b) $\bar{r}_{CNT} = 4.02, \bar{r}_{DNA} = 6.02$ and $\bar{\sigma}_{DNA} = -53.23$. Here, $\alpha = 27.89, \beta = 1, E_F = 0, \bar{l}_B = 2.81$, $\varepsilon_0 = 80, \varepsilon_1 = 80$ and $1/\bar{k} = 402$.

6.4.4 Limitations

This work has several limitations. First, in this work the helical structure of DNA molecule is simplified by smearing the charges uniformly onto a cylindrical surface. This is a standard treatment in continuum theories of polyelectrolyte, and allows us to obtain the solution in a semi-analytical form. More accurate geometry for the CNT-DNA hybrid can be incorporated by considering the DNA backbone charges explicitly via three dimensional modeling.

The main limitation of this model resides in the calculation of σ_{CNT}. First of all, the universal 1D DOS used in σ_{CNT} is approximate. It is valid for small values of energy $|E| << |V_{pp\pi}|$. We identified the range of σ_{DNA}; such that the behavior of the electric potential in D_0 is consistent with experimental observations by Zheng *et al.* Second, the net charge on the CNT is not zero, and it depends on ϕ_2. This implies that the CNT is connected to a source of charges, which is the case when the CNT is grounded. This may not be a good assumption for a CNT suspended in an electrolyte solution. In the situation where the total induced charges on the CNT is zero, the CNT surface is most likely composed of positive and negative "patches", which is only possible when the helical wrapping geometry of the DNA is accurately represented. Next, the universal DOS uses rigid band approximation, where under influence of σ_{DNA}; subbands of the CNT can be moved rigidly up and down without changing $\upsilon(E)$ [21]. This assumption is valid for the coaxial geometry [21]. This is because the cylindrical symmetry generates the same potential across the circumference of the CNT. Our proposed model for the CNT-DNA hybrid ensures that the electric potential is uniform across the circumference of the CNT.

6.5 Conclusions

To summarize, in this paper, we developed a continuum model for the CNT-DNA hybrids in an electrolyte solution. Different cores of the CNTs were distinguished using Mintmire *et al.* expression for the 1D DOS. This model allowed us to obtain an analytical expression for the electric potential in an electrolyte solution for

the CNT-DNA hybrids. The induced charges on the CNT are found to be $1-2$ orders of magnitude smaller than the DNA charges, whether the CNT is metallic or semiconducting. Despite the fact that the induced charges are small, for $\varepsilon_1 = 80$ and for $r_{CNT} = 5$ Å and $r_{DNA} = 10$ Å, the electric potential $\bar{\phi}_0^m$ for the metallic CNT-DNA hybrid in D_0 is weaker than that $\bar{\phi}_0^s$ of the semiconducting CNT-DNA hybrid by 20%. Whereas, for $\varepsilon_1 = 1$, $\bar{\phi}_0^m$ is weaker than $\bar{\phi}_0^s$ by 5%. As the Debye length of the electrolyte solution decreases, the difference between $\bar{\phi}_0^m$ and $\bar{\phi}_0^s$ decreases due to the screening from ions. For the values of $\bar{\sigma}_{DNA}$ from the range of $(-88.96; -61.54)$, which corresponds to the range of helical angles θ measured from the experiments $(26.4^o; 40^0)$, $\bar{\phi}_2^m$ is weaker than $\bar{\phi}_2^s$. This explains why in Zheng's experiments, the metallic CNT-DNA hybrids elute earlier from the charged column than the semiconducting CNT-DNA hybrids. However, for high values of $\bar{\sigma}_{DNA}$, that is $\bar{\sigma}_{DNA} > -171$, the reverse behavior is seen $\left|\bar{\phi}_2^m\right| > \left|\bar{\phi}_2^s\right|$. The results may not be correct, because the expression used to calculate $\bar{\sigma}_{CNT}$ is approximate. It should be noted that high values of $\bar{\sigma}_{DNA}$ correspond to unrealistic wrapping angles for CNT-DNA hybrids. For example, $\bar{\sigma}_{DNA} \simeq -171$ corresponds to 13.4^o. Finally, as r_{CNT} increases the relative percentage error between ϕ_0^m and ϕ_0^s decreases. This is expected because as the radius of the semiconducting CNT increases, its band gap decreases, and semiconducting CNT behaves more like a metallic CNT.

Bibliography

[1] Saito, R., Dresselhaus, G., and Dresselhaus, M.S., *Physical Properties of Carbon Nanotubes*, Imperial College Press, London (1998).

[2] M.S. Dresselhaus, G. Dresselhaus, and P.C. Eklund, *Science of Fullerenes and Carbon Nanotubes*, Academic Press, San Diego (1996).

[3] Zheng M., Jagota A., Semke E.D., Diner B.A., McLean R.S., Lustig S.R., Richardson R.E., Tassi N.G., *Nat. Mater.*, **2**, 338–342 (2003).

[4] Zheng, M., Jagota, A., Strano, M.S., Santos, A.P., Barone, P., Chou, S.G., Diner, B.A., Dresselhaus, M.S., McLean, R.S., Onoa, G.B., Samsonidze, G.G., Semke, E.D., Usrey, M., Walls, D.J., *Science*, **302**, 1545–1548 (2003).

[5] X. Tu, S. Manohar, A. Jagota, M. Zheng, *Nature,* **460**, 250–253 (2009).

[6] S. V. Rotkin, *Annu. Rev. Phys. Chem.*, **61** , 241–61 (2010).

[7] S. E. Snyder and S. V. Rotkin, *JETP Letters*, **84 (6)**, 348–351 (2006).

[8] A.N. Enyashin, S. Gemming, G. Seifert, "DNA-wrapped carbon nanotubes", *Nanotechnology*, **18**, 245702 (2007).

[9] S.Manohar, T. Tang, and A. Jagota, Structure of Homopolymer DNA-CNT Hybrids, *J. Phys. Chem. C*, **111**, 17835–17845 (2007).

[10] R. Johnson, A. T. C. Johnson, and M. L. Klein, *Nano Lett.*, **8(1)**, 69–75 (2008).

[11] Lustig, S.R., Jagota, A., Khripin, C., *J. Phys. Chem. B*, **109(7)**, 2559–2566 (2005).

[12] O. Malysheva, T. Tang, P. Schiavone, *J. of Adhesion*, **87**, 251–271 (2011).

[13] I. Buch, M. J. Harvey, T. Giorgino, D. P. Anderson, and G. De Fabritiis, *J. Chem. Inf. Model.* , **50**, 397–403 (2010).

[14] R.R. Johnson, A. T. C. Johnson, M. L. Klein, *Small*, **6(1)**, 31–34 (2010).

[15] J.D.Jackson, *Classical Electrodynamics*, third ed., Wiley, New York, 1999.

[16] J.W. Mintmire, *Physical Review Letters*, **81(12)**, 2506–2509 (1998).

[17] Mills, P., Anderson, C.F. Record, M.T. Jr., *Journal of Physical Chemistry*, **90(24)**, 6542–6548 (1986)

[18] G.S. Manning, *Physica A: Statistical and Theoretical Physics*, **231**, 236–253 (1996).

[19] A. Nussbaum, *Semiconductor Device Physics*, Prentice-Hall, NJ, 1962.

[20] T. Tang, A. Jagota, *J. of Comput. and Theoretical Nanoscience*, **5**, 1–8 (2008).

[21] J. Guo, S. Goasguen, M. Lundstorm, S. Datta, *Applied Physics Letters,* **81(8)**, 1486–1488 (2002).

[22] Russel, W.B., Saville, D.A., Schowalter, W.R., *Colloidal Dispersions*, Cambridge Univ. Press, Cambridge, UK, 1989.

[23] Abramovitz, M., Stegun, I.A., *Handbook of Mathematical Functions*, Dover, New-York (1965).

[24] J. G. Duque, A. N. G. Parra-Vasquez, N. Behabtu, M. J. Green, A. L. Higginbotham, B. K. Price, A. D. Leonard, H. K. Schmidt, B. Lounis, J. M. Tour, S. K. Doorn, L. Cognet, and M. Pasquali, *ACS NANO*, **4(6)**, 3063–3072 (2010).

[25] T. Schlick, *Molecular modeling and simulation: an interdisciplinary guide. Interdisciplinary applied mathematics*, Springer, 2002.

[26] S. Kilina, D. A. Yarotski, A. A. Talin, S. Tretiak, A. J. Taylor, and A. V. Balatsky, *Journal of Drug Delivery*, Article ID 415621, 9 pages, 2011.

Chapter 7
Conclusions and Future work

7.1 Conclusions

At the current moment numerous different systems consisting of charged objects interacting with electronically responsive structures exist at the micro/nano scale level. In practical applications, the mentioned systems are embedded in an electrolytic environment. For example, cells adhering to an implant's surface, biosensors detecting specific DNA molecules, and DNA molecules which are used to separate bundled CNTs.

By keeping the focus on the latter example, it was shown that in order to gain control of the separation technique for the CNT-DNA hybrids, it is necessary to understand their behavior and identify important integrations for hybrids in an electrolyte solution. Experimentally, it has been observed that the separation of the CNTs based on their electronic properties depends on many factors such as the DNA sequence, and the type of ions in the electrolyte solution. However, the reasons for this are not well understood. Ultimately, one would like to know what are the optimal factors for the separation of the CNTs. A theoretical understanding of the separation mechanism for CNT-DNA hybrids could help find the optimal factors without testing all the possibilities. At the current moment, most of the works, which are available in this field, are performed via experiments or molecular dynamics simulations.

In this work, the systematic study at the continuum level is performed and an analytical solution is obtained for the electrostatic interaction between the CNT-DNA hybrid embedded in an electrolyte solution. It was shown throughout this work that the electrostatic interaction has to be considered not only because a DNA molecule becomes charged in an electrolyte solution, but also because the CNT responds electronically to the electric field created by the DNA charges. In addition,

a CNT-DNA hybrid exhibits an influence from the electrolyte solution, therefore, it also has to be considered.

To the author's knowledge, this is the only work, where at the continuum level, the boundary value problems for the electrostatic interaction for the simplified models of CNT-DNA hybrid were rigorously solved. In the presented models, the response of the electrolyte solution to the CNT-DNA hybrid is incorporated using the linear Poisson-Boltzmann equation. Simplified models for DNA molecules are used. These models allowed us to obtain an analytical solution for the electric potential for the CNT-DNA hybrid. This provides an opportunity to test systems with different conditions at a real time scale. In the first three models, the response of the CNT to a DNA was incorporated by considering electronically responsive structures. In the last model, a more realistic response of the CNT to the DNA charge was used. That is, the expression for the DOS derived by Mintmire *et al.* was incorporated in order to distinguish semiconducting and metallic CNTs. The obtained analytical solution allows one to test different conditions (such as salt concentration, DNA charge) at a real time scale. In addition to that the obtained results shed light on the experimental observations by Zheng *et al.* Also, the author believes that these results should encourage the development of physically realistic models for the CNT-DNA hybrids.

The obtained understanding from this dissertation can be applied to modeling other systems involving charged particles interacting with electronically responsive structures. As was shown in this work, the response of the electronically responsive structure has to be considered when the charged particle is located nearby.

7.2 Future Work

In this work, the primary goal was to obtain analytical or semi-analytical solutions from the continuum point of view for the CNT-DNA hybrids embedded in an electrolyte solution and to use these results for understanding DNA-assisted separation of the CNTs.

As an extension of this work, it could be interesting to look at the phenomenon

of counterion condensation on the DNA molecule and how it would be influenced by metallic and semiconducting CNTs. To do that the model developed in Chapter 6 could be considered. This model includes key elements in the modeling of electrostatics of the CNT-DNA hybrid: the effect of an electrolyte solution, the charges of a DNA, and the response of the CNT to the DNA charges. To the author's knowledge, at the current moment, this is the only work where these key elements in the modeling of electrostatics are considered in a rigorous way. Therefore, it would be of a great interest to apply Manning's theory of counterion condensation to this model in order to obtain the semi-analytical expression for the amount of condensed counterions. Also, it would be interesting to study how this amount depends on the distance between a CNT and a DNA molecule.

As a further extension of the present work, a three-dimensional model for the CNT-DNA hybrid embedded in an electrolyte solution can be developed by combining all the obtained knowledge from the current work, as well as incorporating new results. The electrolyte solution can be modeled via the Debye-Hückel or the Poisson-Boltzmann equation. A more realistic three-dimensional model for a ssDNA could be utilized, that is, by modeling ssDNA as a helix of discrete charges. A new approach for calculating the generated charge on the CNT caused by the DNA charges has to be used in the three-dimensional model of the CNT-DNA hybrid. The method used in Chapter 6 is valid only for the cylindrical symmetry, and it becomes unapplicable for the three-dimensional model of the CNT-DNA hybrid. Rotkin *et al.* developed a model for calculating the induced surface charge density on the CNT in the framework of the tight binding method in the nearest neighbor approximation [2]. However, this model has to be tackled using numerical calculations.

In the CNT-DNA hybrid, other contributions, such as van der Waals forces should be incorporated. Van der Waals force is a leading factor of adhesion between DNA and CNT [1]. This contribution can be incorporated by utilizing the Lennard-Jones potential for the interaction of the CNT atoms with other atoms. There are many other aspects of the CNT and DNA molecule interactions, such as the entropic effect, enthalpy change due to deformation of the ssDNA and the CNT,

hydrogen bonding, and the hydrophobic interaction. In the case of single stranded DNA—CNT hybrids, through MD simulations [1], it was demonstrated that, at low ionic strength, electrostatic and van der Waals interactions are two important contributions to the free energy of the hybrid.

Bibliography

[1] S. Manohar, T. Tang, A. Jagota, J. Phys. Chem. C 111 (2007) 17835.

[2] S. E. Snyder and S. V. Rotkin, *JETP Letters*, **84 (6)**, 348–351 (2006).

Appendix A: Supportive information for Chapter 4

A.1 Asymptotic analysis for CC

In the following we give the detailed asymptotic analysis from which we obtained the equations to determine CC. In all cases, the geometry of the cylinder and the PE are fixed, that is, r_0/a is constant. We consider $ka \to 0$ at a different normalized separation d/a. Systems of the PE–metallic cylinder and the PE–dielectric cylinder are considered separately.

A.1.1 PE–metallic cylinder

First we consider the case where the PE is infinitely far from the metallic cylinder. This is achieved by first holding ka fixed and letting $d/a \to \infty$. In this limit

$$K_n\left[ka\left(\frac{d}{a}-1\right)\right] \to 0, \tag{A.1.1.1}$$

and Eq. (4.19) reduces to

$$-2zN\xi(1-z\theta)\frac{K_0(ka)}{kaK_1(ka)} - 2N\ln(ka) + N\ln\frac{4\pi e\theta l_B N_A a^2 \sum_i \nu_i z_i^2}{\gamma\nu Q} = 0, \tag{A.1.1.2}$$

that is, Eq. (4.21).

In the limit of finite separation between the PE and the cylinder irrespective of the dilution, we fix d/a and set $ka \to 0$, then the asymptotic behaviors of the terms in Eq. (4.19) are

$$K_0(ka) \sim -\ln(ka), \tag{A.1.1.3}$$

$$kaK_1(ka) \sim 1, \tag{A.1.1.4}$$

$$f_0^{met} K_0 \left[ka(\frac{d}{a} - 1) \right] \sim -\frac{\ln(ka) \ln\left[ka(\frac{d}{a} - 1)\right]}{\ln(ka \cdot r_0/a)} - \frac{\ln\left[ka(\frac{d}{a} - 1)\right]}{2\pi \ln(ka \cdot r_0/a)} \int_0^{2\pi} \ln\left[\Lambda(\psi)\right] d\psi, \quad \text{(A.1.1.5)}$$

$$f_n^{met} K_n \left[ka \left(\frac{d}{a} - 1 \right) \right] \sim -\frac{1}{\pi} \left(\frac{r_0/a}{d/a - 1} \right)^n \times \int_0^{2\pi} \ln\left[\Lambda(\psi)\right] \cos(n\psi) d\psi, n > 0, \quad \text{(A.1.1.6)}$$

$$ka f_0^{met} K_1 \left[ka(\frac{d}{a} - 1) \right] \sim \frac{1}{(d/a - 1)} \frac{\ln(ka)}{\ln(ka \cdot r_0/a)} + \frac{1}{2\pi(d/a - 1)\ln(ka \cdot r_0/a)} \int_0^{2\pi} \ln\left[\Lambda(\psi)\right] d\psi, \quad \text{(A.1.1.7)}$$

$$ka f_n^{met} K_{n+1} \left[ka(\frac{d}{a} - 1) \right] \sim -\frac{2}{\pi} \frac{n}{(d/a - 1)} \left(\frac{r_0/a}{d/a - 1} \right)^n \times \int_0^{2\pi} \ln\left[\Lambda(\psi)\right] \cos(n\psi) d\psi, n > 0. \quad \text{(A.1.1.8)}$$

Substituting these equations into Eq. (4.19), it is clear that the dominating terms in the numerator are $-\ln(ka)$ from $K_0(ka)$ and $[\ln(ka)]^2 / \ln(ka \cdot r_0/a)$ from $f_0^{met} K_0 \left[ka(d/a - 1)\right]$. The second term in (A.1.1.5) is finite in the limit of $ka \to 0$. All terms in the denominator are finite in the dilute limit, except the second term in (A.1.1.7), which vanishes as $ka \to 0$. Keeping the leading terms in Eq. (4.19), we get

$$\frac{-2zN\xi(1 - z\theta)\left[\frac{\ln(ka)}{\ln(ka \cdot r_0/a)} - 1\right] \ln(ka)}{1 + \frac{1}{d/a - 1} \frac{\ln(ka)}{\ln(ka \cdot r_0/a)} - \frac{1}{\pi(d/a - 1)} \sum_{n=1}^{\infty} \left[n \left(\frac{r_0/a}{d/a - 1} \right)^n \int_0^{2\pi} \ln\left[\Lambda(\psi)\right] \cos(n\psi) d\psi \right]} - 2N \ln(ka) = 0. \quad \text{(A.1.1.9)}$$

To see the transition between the two above limiting cases, we proposed the scaling relation $d/a = A(ka)^{-\alpha}$. This ensures that in the dilution of $ka \to 0$,

$r_0/a \ll d/a \ll 1/ka$. Under this condition, the asymptotic expressions of the terms in Eq. (4.19) are

$$f_0^{met} K_0 \left[ka \left(\frac{d}{a} - 1 \right) \right] \sim -\frac{\left[\ln(ka) + \ln\left(\frac{d}{a}\right) \right]^2}{\ln(ka)}, \tag{A.1.1.10}$$

$$ka f_0^{met} K_1 \left[ka(\frac{d}{a} - 1) \right] \sim \frac{1}{d/a} \frac{\ln(ka)}{\ln(ka)} + \frac{1}{d/a} \frac{\ln\left(\frac{d}{a}\right)}{\ln(ka)}, \tag{A.1.1.11}$$

$$f_n^{met} K_n \left[ka \left(\frac{d}{a} - 1 \right) \right] \sim 0, n > 0, \tag{A.1.1.12}$$

$$ka f_n^{met} K_{n+1} \left[ka(\frac{d}{a} - 1) \right] \sim 0, n > 0. \tag{A.1.1.13}$$

Substituting the above expressions into Eq. (4.19) and using $d/a = A(ka)^{-\alpha}$, we obtain

$$-2zN\xi(1 - z\theta) \left[-1 + (1 - \alpha)^2 \right] \ln(ka) - 2N \ln(ka) = 0. \tag{A.1.1.14}$$

A.1.2 PE–dielectric cylinder

The equation to determine CC for the case of a PE near a dielectric cylinder is the same as Eq. (4.19) with the coefficients f_n^{met} replaced by f_n^{diel}. With fixed d/a and $ka \to 0$, the asymptotic expressions of the terms in Eq. (4.19) are given by

$$f_0^{diel} K_0 \left[ka \left(\frac{d}{a} - 1 \right) \right] \sim -\frac{r_0}{2\pi a} \ln \left[ka \left(\frac{d}{a} - 1 \right) \right] \int_0^{2\pi} \frac{r_0 - d\cos(\psi)}{a\Lambda^2(\psi)} d\psi, \tag{A.1.2.1}$$

$$ka f_0^{diel} K_1 \left[ka \left(\frac{d}{a} - 1 \right) \right] \sim \frac{r_0}{2\pi a \left(d/a - 1 \right)} \int_0^{2\pi} \frac{r_0 - d\cos(\psi)}{a\Lambda^2(\psi)} d\psi, \tag{A.1.2.2}$$

$$f_n^{diel} K_n \left[ka \left(\frac{d}{a} - 1 \right) \right] \sim -\frac{\varepsilon_2}{\pi(\varepsilon_1 + \varepsilon_2)} \left(\frac{r_0/a}{d/a - 1} \right)^n \int_0^{2\pi} \ln\left[\Lambda(\psi)\right] \cos(n\psi) d\psi$$

$$+ \frac{\varepsilon_1}{\pi n(\varepsilon_1 + \varepsilon_2)} \left(\frac{r_0/a}{d/a - 1} \right)^n \int_0^{2\pi} \frac{r_0 \left[r_0 - d\cos(\psi) \right]}{a^2\Lambda^2(\psi)} \cos(n\psi) d\psi, n > 0, \tag{A.1.2.3}$$

$$ka f_n^{diel} K_{n+1} \left[ka \left(\frac{d}{a} - 1 \right) \right] \sim \frac{2}{\pi(\varepsilon_1 + \varepsilon_2)} \left(\frac{r_0/a}{d/a - 1} \right)^{n+1}$$

$$\times \int_0^{2\pi} \frac{\varepsilon_1 r_0 \cos(n\psi) + d\left(\varepsilon_2 \sin(\psi)\sin(n\psi) - \varepsilon_1 \cos(\psi)\cos(n\psi)\right)}{a\Lambda^2(\psi)} d\psi, n > 0. \tag{A.1.2.4}$$

Under condition $d > r_0$, the integral $\int_0^{2\pi} \left[r_0 - d\cos(\psi)\right] / \left[\Lambda^2(\psi)\right] d\psi$ is exactly zero. Therefore,

$$f_0^{diel} K_0\left[ka\left(\frac{d}{a} - 1\right)\right] \sim 0, \tag{A.1.2.5}$$

$$ka f_0^{diel} K_1\left[ka\left(\frac{d}{a} - 1\right)\right] \sim 0. \tag{A.1.2.6}$$

Keeping only the leading terms in Eq. (4.19), which are logarithmic in ka, we have the following equation

$$\frac{-2N\xi z(1 - z\theta)[-\ln(ka)]}{1 + \frac{1}{\pi(\varepsilon_1+\varepsilon_2)} \sum_{n=1}^{\infty} \left(\frac{r_0/a}{d/a-1}\right)^{n+1} \int_0^{2\pi} \frac{\varepsilon_1 r_0 \cos(n\psi) + d(\varepsilon_2 \sin(\psi)\sin(n\psi) - \varepsilon_1 \cos(\psi)\cos(n\psi))}{a\Lambda^2(\psi)} d\psi} - 2N\ln(ka) = 0. \tag{A.1.2.7}$$

A.2 Expressions for the normalized potential, the electric displacement for the PE–metallic and the PE–dielectric cylinders

With the proposed normalization in Section 4.5, the expressions for the normalized electric potential in D_0 and D_2 and for the normalized electric displacement for the PE–metallic and the PE–dielectric cylinder systems are given, respectively, by

$$\bar{\phi}_{out} = \frac{K_0(\bar{r}') - \sum_{n=0}^{\infty} \bar{f}_n \cos(n\psi) K_n(\bar{r})}{K_1(\bar{a}) + \bar{f}_0 K_1(\bar{d} - \bar{a}) + \frac{1}{2}\sum_{n=1}^{\infty} \bar{f}_n K_{n+1}(\bar{d} - \bar{a})} \text{ in } D_0, \tag{A.2.1}$$

$$\bar{\phi}_{in(s)} = \frac{K_0(\bar{a}) - \sum_{n=0}^{\infty} \bar{f}_n K_n(\bar{d} - \bar{a})}{K_1(\bar{a}) + \bar{f}_0 K_1(\bar{d} - \bar{a}) + \frac{1}{2}\sum_{n=1}^{\infty} \bar{f}_n K_{n+1}(\bar{d} - \bar{a})} \text{ in } D_2, \tag{A.2.2}$$

$$\frac{\partial \bar{\phi}_{out}}{\partial \bar{r}'} = -\frac{K_1(\bar{r}') + \left(\sum_{n=0}^{\infty} \bar{f}_n \cos(n\psi) \frac{\partial K_n(\bar{r})}{\partial \bar{r}}\right) \frac{\partial \bar{r}}{\partial \bar{r}'} + \left(\sum_{n=0}^{\infty} \bar{f}_n \frac{\partial \cos(n\psi)}{\partial \psi} K_n(\bar{r})\right) \frac{\partial \psi}{\partial \bar{r}'}}{K_1(\bar{a}) + \bar{f}_0 K_1(\bar{d} - \bar{a}) + \frac{1}{2}\sum_{n=1}^{\infty} \bar{f}_n K_{n+1}(\bar{d} - \bar{a})}.$$

The superscripts met and $diel$ have been removed from the above expressions with the understanding that the corresponding coefficients $\bar{f}_n$ will be used for each case. The normalized coefficients $\bar{f}_n$ corresponding to the PE–metallic and the PE–dielectric cylinders are given, respectively, by

$$\bar{f}_n^{met} = \begin{cases} \dfrac{\int_0^{2\pi} K_0\big[\bar{a}\bar{\Lambda}(\psi)\big]d\psi}{2\pi K_0(\bar{r}_0)}, & n = 0 \\ \dfrac{\int_0^{2\pi} K_0\big[\bar{a}\bar{\Lambda}(\psi)\big]\cos(n\psi)d\psi}{\pi K_n(\bar{r}_0)}, & n > 0 \end{cases} \tag{A.2.3}$$

and

$$\bar{f}_n^{diel} = \begin{cases} \dfrac{1}{2\pi K_1(\bar{r}_0)} \int_0^{2\pi} \dfrac{\big[\bar{r}_0 - \bar{d}\cos(\psi)\big]K_1\big[\bar{a}\bar{\Lambda}(\psi)\big]}{\bar{a}\bar{\Lambda}(\psi)} d\psi, & n = 0 \\ \dfrac{n\varepsilon_2 \int_0^{2\pi} K_0\big[\bar{a}\bar{\Lambda}(\psi)\big]\cos(n\psi)d\psi}{\pi n(\varepsilon_1+\varepsilon_2)K_n(\bar{r}_0)} + \dfrac{\varepsilon_1\bar{r}_0 \int_0^{2\pi} \frac{[\bar{r}_0 - \bar{d}\cos(\psi)]K_1[\bar{a}\bar{\Lambda}(\psi)]}{\bar{a}\bar{\Lambda}(\psi)}\cos(n\psi)d\psi}{\pi n(\varepsilon_1+\varepsilon_2)K_n(\bar{r}_0)}, & n > 0, \end{cases} \tag{A.2.4}$$

where $\bar{\Lambda}(\psi) = \bar{a}^{-1}\sqrt{\bar{r}_0^2 - 2\bar{r}_0\bar{d}\cos\psi + \bar{d}^2}$. 4

Appendix B: Review of calculations for the energy dispersion relation

In this appendix, the results for the energy dispersion relation for graphene are repeated from Saito [1] and Reich et al [2]. After that it is outlined how these results can be used to derive the 1D DOS derived by Mintmire *et al.* [3].

B.1 Review of calculations of energy dispersion relations

CNT can be represented as a graphene sheet rolled into a cylinder. As was mentioned in Chapter 1, "graphene can be imagined as atomic-scale "chicken wire", made of carbon atoms and covalent bonds (special chemical bonds) between them". A graphene sheet can be represented by joined hexagons. The distance between two atoms is denoted as a_{C-C} and it is equal to 1.44 Å. It is possible to construct a graphene surface by translating the unit cell, consisting of two atoms A and B (See Figure B.1). There is one basis function per atom. Therefore, there are two basis

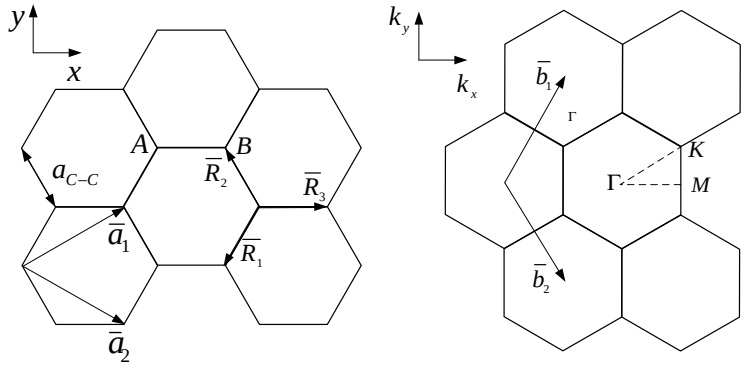

Figure B.1: a) the unit cell of the graphene and b) Brillouin zone of graphene.

functions per unit cell. $\vec{a}_1$ and $\vec{a}_2$ are the unit vectors of the hexagonal lattice in the real space. They could be expressed in terms of a

$$\vec{a}_1 = \left(\frac{\sqrt{3}}{2}a, \frac{a}{2}\right), \ \vec{a}_2 = \left(\frac{\sqrt{3}}{2}a, -\frac{a}{2}\right). \tag{B.1.1}$$

Another useful length can be derived knowing the above information: $a = \sqrt{3}a_{C-C}$.

The unit vectors from the reciprocal hexagonal lattice are the following

$$\vec{b}_1 = \left(\frac{3\pi}{\sqrt{3}a}, \frac{2\pi}{a}\right), \ \vec{b}_2 = \left(\frac{3\pi}{\sqrt{3}a}, -\frac{2\pi}{a}\right). \tag{B.1.2}$$

In order to obtain an expression describing the electronic properties of the CNTs, the Schrodinger equation has to be solved. The matrix form of Schrodinger equation is the following

$$H\Psi(\vec{k}) = E(\vec{k})\Psi(\vec{k}), \tag{B.1.3}$$

where H is Hamiltonian, $E(\vec{k})$ are the eigenvalues at wave vector $\vec{k}$, and $\Psi(\vec{k})$ are the eigenfunctions. The eigenfunctions can be expressed by a linear combination of Bloch functions

$$\Psi(\vec{k}) = \sum_l C_l \Phi_l(\vec{k}). \tag{B.1.4a}$$

The tight binding (TB) method is one of two basic approaches to calculate the electronic energy bands of a material [2]. It is performed by considering only the nearest-neighbor interactions. In the TB method, the Bloch functions can be expressed as linear combination of the atomic wave functions. For the unit cell of graphene, which contains two atoms A and B, the Bloch function for A and B sublattices has the following form

$$\Phi_i = \frac{1}{\sqrt{N}} \sum_{\vec{R}}^{N} e^{i\vec{k}\cdot\vec{R}_i} \varphi(\vec{r} - \vec{R}_i), \ i = A, B. \tag{B.1.5}$$

Here, N is the number of unit cells in the solid, and $\vec{R}_i$ is a lattice vector, and $\varphi(\vec{r})$ is the atomic wave function.

Now, the Schrodinger equation can be written in terms of the Bloch functions, that is, substitute Eqs. (B.1.4a) and (B.1.5) in Eq. (B.1.3). From here, to obtain for

eigenvalues $E(\vec{k})$, the so-called secular equation has to be solved

$$\det(H - ES) = 0. \tag{B.1.6}$$

For graphene, H is Hamiltonian (2x2) matrix. The elements of H (transfer matrix) and S (overlap between Bloch functions matrix) have the following form:

$$H_{IJ}(\vec{k}) = \langle \Phi_I | H | \Phi_J \rangle,\ S_{IJ}(\vec{k}) = \langle \Phi_I | \Phi_J \rangle. \tag{B.1.7}$$

By considering only the nearest-neighbor interactions, the diagonal terms for H and S are the following

$$H_{AA}(\vec{k}) = \left\langle \varphi_A(\vec{r} - \vec{R}_A) | H | \varphi_A(\vec{r} - \vec{R}_A) \right\rangle = \epsilon_{2p} = H_{BB}(\vec{k}), \tag{B.1.8}$$

$$S_{AA}(\vec{k}) = \langle \varphi_A(\vec{r} - \vec{R}_A) | \varphi_A(\vec{r} - \vec{R}_A) \rangle = 1 = S_{BB}(\vec{k}). \tag{B.1.9}$$

For the off-diagonals terms, the interaction of atom A needs to be considered with three nearest-neighbor interactions B atoms. The distance between them is denoted as $\vec{R}_1, \vec{R}_2$ and $\vec{R}_3$ (See Figure B.1)

$$H_{AB}(\vec{k}) = \frac{1}{N} \sum_{\vec{R}_A}^{N} \sum_{\vec{R}_B}^{N} \langle e^{i\vec{k}\cdot\vec{R}_A} \varphi_A(\vec{r} - \vec{R}_A) | H | e^{i\vec{k}\cdot\vec{R}_B} \varphi_B(\vec{r} - \vec{R}_B) \rangle. \tag{B.1.10}$$

The second sum runs over all three nearest neighbors of a given atom A

$$\vec{R}_1 = \frac{1}{3}\left(\vec{a}_2 - 2\vec{a}_1\right),\ \ \vec{R}_2 = \frac{1}{3}\left(\vec{a}_1 - 2\vec{a}_2\right),\ \ \vec{R}_3 = \frac{1}{3}\left(\vec{a}_2 + \vec{a}_1\right). \tag{B.1.11}$$

For the case in hand, substituting Eq. (B.1.11) in Eq. (B.1.10), the expression for H_{AB} becomes

$$H_{AB}(\vec{k}) = t(e^{i\vec{k}\cdot\vec{R}_1} + e^{i\vec{k}\cdot\vec{R}_2} + e^{i\vec{k}\cdot\vec{R}_3}) = tf(k), \tag{B.1.12}$$

where t is given by $t = \langle \varphi_A(\vec{r} - \vec{R}_A) | H | \varphi_B(\vec{r} - \vec{R}_B) \rangle$, and $f(k)$ has the following form

$$f(k) = \exp\left(\frac{ik_x a}{\sqrt{3}}\right) + 2\exp\left(-\frac{ik_x a}{2\sqrt{3}}\right)\cos\left(\frac{k_y a}{2}\right), \tag{B.1.13}$$

$f(k)$ is a complex function, and the Hamiltonian forms a Hermitian matrix, therefore $H_{BA} = H^*_{AB}$, where $*$ denotes the complex conjugate. The overlap integral matrix is given by $S_{AA} = S_{BB} = 1$, and $S_{BA} = S^*_{AB} = sf(k)$, where $s = \langle \varphi_A(\vec{r} - \vec{R}_A) | \varphi_B(\vec{r} - \vec{R}_B) \rangle$.

Therefore, the explicit form for H and S can be written as

$$H = \begin{pmatrix} \epsilon_{2p} & tf(k) \\ tf(k)^* & \epsilon_{2p} \end{pmatrix}, \quad S = \begin{pmatrix} 1 & sf(k) \\ sf(k)^* & 1 \end{pmatrix}, \tag{B.1.14}$$

The eigenvalues $E(\vec{k})$ can be obtained by solving the secular equation

$$\begin{vmatrix} \epsilon_{2p} - E & tf(k) - Esf(k) \\ tf(k)^* - Esf(k)^* & \epsilon_{2p} - E \end{vmatrix} = 0. \tag{B.1.15}$$

The general form for the eigenvalues $E(\vec{k})$ is

$$E_{g2D}(\vec{k}) = \frac{\epsilon_{2p} \pm tw(\vec{k})}{1 \pm sw(\vec{k})}, \tag{B.1.16}$$

where $w(\vec{k}) = \sqrt{f(\vec{k})f(\vec{k})^*}$ such that

$$w(\vec{k}) = \sqrt{1 + 4\cos\left(\sqrt{3}k_x a/2\right)\cos\left(k_y a/2\right) + 4\cos^2\left(k_y a/2\right)}. \tag{B.1.17}$$

E^+ refer to π^*, and E^- refer to π bands, respectively.

When the overlap integral $s = 0$ and $\epsilon_{2p} = 0$, the expression becomes

$$E_{g2D}(k_x, k_y) = \pm t\sqrt{1 + 4\cos\left(\frac{\sqrt{3}k_x a}{2}\right)\cos\left(\frac{k_y a}{2}\right) + 4\cos^2\left(\frac{k_y a}{2}\right)}. \tag{B.1.18}$$

Figure B.2 is used to depict the energy dispersion relation for graphene. The upper half space of the energy dispersion curves describes the π^*-energy anti-bonding band, and the lower half is the π-energy bonding band. The points, where π^* and π bands intersect, are called K points. In each hexagon, there is six points at the locations of the carbon atoms. For the discussed case, K points are the following $\left(0, \pm\frac{4\pi}{3a}\right)$, $\left(\frac{2\pi}{a\sqrt{3}}, \pm\frac{2\pi}{3a}\right)$, $\left(-\frac{2\pi}{a\sqrt{3}}, \pm\frac{2\pi}{3a}\right)$. Taylor expansion around K point for $tf(k)$ is

$$\begin{aligned} tf(k) \simeq tf(k_x^p, k_y^p) + \left[\frac{\partial f}{\partial k_x}\right]_{k_x^p, k_y^p}(k_x - k_x^p) + \left[\frac{\partial f}{\partial k_y}\right]_{k_x^p, k_y^p}(k_y - k_y^p) \\ = \frac{\sqrt{3}}{2}ita\left(k_x - i\beta_y\right), \end{aligned} \tag{B.1.19}$$

where $\beta_y = k_y - 4\pi/3a$.

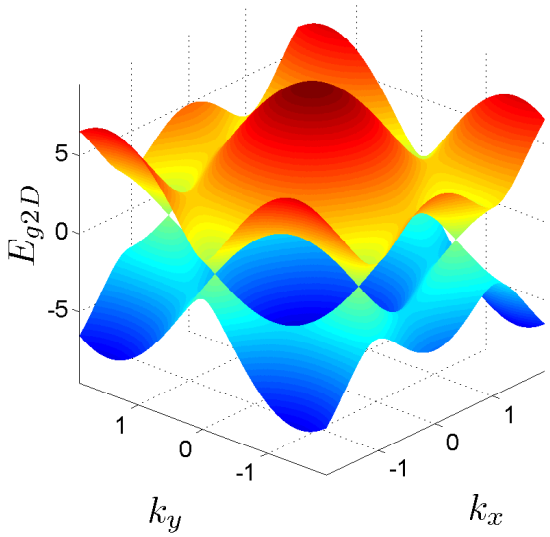

Figure B.2: The energy dispersion relation using Eq. (B.1.16), where $\epsilon_{2p} = 0, t = -3.033$ eV, $s = 0$.

Eq. (B.1.16) near K points has the following form

$$E_{g2D}(k) = \pm\frac{\sqrt{3}}{2}ta\sqrt{k_x^2 + \beta_y^2}, \tag{B.1.20}$$

which is the so-called linear dispersion relation for graphene.

Consequently, Mintmire *et al.* have utilized the expression for the linear dispersion relation in order to obtain the universal expression for the one-dimensional (1D) density of states (DOS) for the CNTs. To do that the energy dispersion relation for graphene was quantized along the circumference of the CNT with radius r_t, and number of states below energy E was calculated.

The following is the expression derived by Mintmire *et al.* for the universal DOS for CNT per carbon atom near Fermi level

$$\rho(E) = \frac{a}{\pi^2 r_t \left|V_{pp\pi}\right|} \sum_{m=-\infty}^{\infty} g\left(E, \gamma_m\right), \tag{B.1.21}$$

where $V_{pp\pi}$ is the nearest-neighbor interaction, $|V_{pp\pi}| = 2.5$ eV, a is the lattice constant of the graphene sheet and

$$g(E, \varepsilon_m) = \begin{cases} \frac{|E|}{\sqrt{E^2 - \gamma_m^2}}, & |E| > |\gamma_m|, \\ 0, & |E| < |\gamma_m|, \end{cases} \tag{B.1.22}$$

$$|\gamma_m| = \frac{a|V_{pp\pi}\,(3m - n_1 + n_2)\,|}{2\sqrt{3}r_t}, \tag{B.1.23}$$

where (n_1, n_2) are the pair of integer indices defining CNTs chirality.

Because the expression for $\rho(E)$ is approximate, it is valid for small values of the energy, that is, $|E| << |V_{pp\pi}|$. Figure B.3 represents the DOS using the above equation.

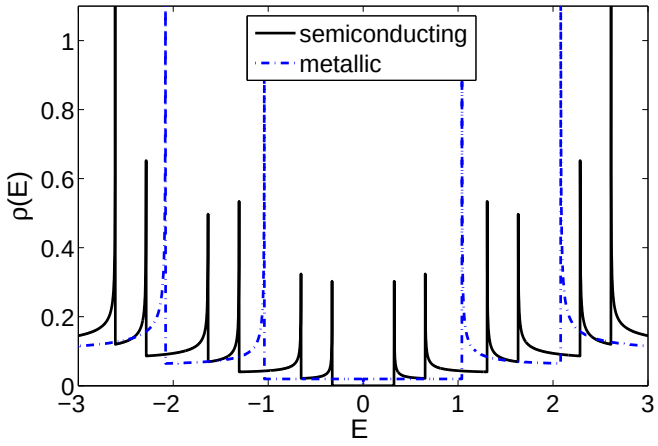

Figure B.3: Density of states for semiconducting and metallic CNTs.

The expression for summation in $g\,(E, \gamma_m)$ can be expressed in a different way.

$$|E| > |\gamma_m|,$$

$$|E| > \left|\frac{a|V_{pp\pi}\,(3m - n_1 + n_2)\,|}{2\sqrt{3}r_t}\right|.$$

For a CNT with a pair of indices (n_1, n_2), metallic CNTs correspond to the case $|n_1 - n_2| = 3q$ and semiconducting CNTs correspond to the case $|n_1 - n_2| = 3q + 1$, where q is an integer.

Therefore, for metallic CNTs when $E/V_{pp\pi} > 0$

$$\frac{2\sqrt{3}r_t E}{aV_{pp\pi}} > |3m - 3q| = |3m'|\,,$$

where m' is an integer. This leads to

$$\left\lceil -\frac{2\sqrt{3}r_t E}{3aV_{pp\pi}} \right\rceil \leq m' \leq \left\lceil \frac{2\sqrt{3}r_t E}{3aV_{pp\pi}} \right\rceil - 1,$$

where $\lceil x \rceil$ is a ceiling function.

For semiconducting CNTs when $E/V_{pp\pi} > 0$

$$\frac{2\sqrt{3}r_t E}{aV_{pp\pi}} > |3m - 3q - 1| = |3m' - 1|\,.$$

Therefore, the condition for m' is the following

$$\left\lceil -\frac{2\sqrt{3}r_t E}{3aV_{pp\pi}} + \frac{1}{3} \right\rceil \leq m' \leq \left\lceil \frac{2\sqrt{3}r_t E}{3aV_{pp\pi}} + \frac{1}{3} \right\rceil - 1.$$

Therefore, $\upsilon(E)$ can be rewritten as

for metallic CNT:

$$\rho(E) = \frac{a}{\pi^2 r_t \left|V_{pp\pi}\right|} \sum_{m'=\left\lceil -\frac{2\sqrt{3}r_t E}{3aV_{pp\pi}} \right\rceil}^{\left\lceil \frac{2\sqrt{3}r_t E}{3aV_{pp\pi}} \right\rceil - 1} \frac{|E|}{\sqrt{E^2 - (3m')^2}},$$

for semiconducting CNT:

$$\rho(E) = \frac{a}{\pi^2 r_t \left|V_{pp\pi}\right|} \sum_{m'=\left\lceil -\frac{2\sqrt{3}r_t E}{3aV_{pp\pi}} + \frac{1}{3} \right\rceil}^{\left\lceil \frac{2\sqrt{3}r_t E}{3aV_{pp\pi}} + \frac{1}{3} \right\rceil - 1} \frac{|E|}{\sqrt{E^2 - (3m' - 1)^2}}.$$

Bibliography

[1] Saito, R., Dresselhaus, G., and Dresselhaus, M.S., Physical Properties of Carbon Nanotubes, Imperial College Press, London (1998).

[2] Reich, S. and Thomsen, C. and Maultzsch, J., Carbon nanotubes: basic concepts and physical properties, Wiley-VCH, 2004.

[3] J.W. Mintmire, Universal Density of States for Carbon Nanotubes, Physical Review Letters, 1999.